POROUS OPTICAL COATINGS BY OBLIQUE ANGLE DEPOSITION

By

RAJ BAHADUR TOKAS

(PHYS01201004013)

Bhabha Atomic Research Centre, Mumbai

A thesis submitted to the

Board of Studies in Physical Sciences

In partial fulfillment of requirements

for the Degree of

DOCTOR OF PHILOSOPHY

of

HOMI BHABHA NATIONAL INSTITUTE

March, 2017

Homi Bhabha National Institute

Recommendations of the Viva Voce Board

As members of the Viva Voce Board, we certify that we have read the dissertation prepared by **R. B. Tokas** entitled **"*Porous optical coatings by oblique angle deposition*"** and recommend that it may be accepted as fulfilling the dissertation requirement for the Degree of Doctor of Philosophy.

D S Patil 23-08-2017
Date:

Chairman- **Dr. D. S. Patil**

Date: 23/8/2017

Guide / Convener- **Dr. N. K. Sahoo**

Date: 23/08/2017

Member 1- **Dr. S. C. Gadkari**

Date: 23/08/17

Member 2- **Dr. Saibal Basu**

Date: 23.8.2017

External Examiner- **Dr. R. Ganesan**

Final approval and acceptance of this dissertation is contingent upon the candidate's submission of the final copies of the dissertation to HBNI.

I hereby certify that I have read this dissertation prepared under my direction and recommend that it may be accepted as fulfilling the dissertation requirement.

Date: 23/8/2017

Place: Mumbai

Dr. N. K. Sahoo

(Guide)

STATEMENT BY AUTHOR

This dissertation has been submitted in partial fulfillment of requirements for an advanced degree at Homi Bhabha National Institute (HBNI) and is deposited in the Library to be made available to borrowers under rules of the HBNI.

Brief quotations from this dissertation are allowable without special permission, provided that accurate acknowledgement of source is made. Requests for permission for extended quotation from or reproduction of this manuscript in whole or in part may be granted by the Competent Authority of HBNI when in his or her judgment the proposed use of the material is in the interests of scholarship. In all other instances, however, permission must be obtained from the author.

R. B. Tokas

DECLARATION

I, hereby declare that the investigation presented in the thesis has been carried out by me. The work is original and has not been submitted earlier as a whole or in part for a degree / diploma at this or any other Institution / University.

R. B. Tokas

LIST OF PUBLICATIONS ARISING FROM THE THESIS

Journal

1. “Oblique angle deposition of HfO_2 thin films: quantitative assessment of indentation modulus and microstructural properties”, R. B. Tokas, S. Jena, P. Sarkar, S. R. Polaki, S. Thakur, S. Basu and N. K. Sahoo, *Mater. Res. Express*, **2015**, *2*, 035010.
2. “Effect of angle of deposition on micro-roughness parameters and optical properties of HfO_2 thin films deposited by reactive electron beam evaporation”, R. B. Tokas, S. Jena, S. Thakur, N. K. Sahoo, Thin Solid Films, **2016**, 609, Pages 42–48.
3. “Study of Hafnium Oxide thin films deposited by RF magnetron sputtering under glancing angle deposition at varying target to substrate distance”, S. Maidul Haque, K. Divakar Rao, J. S. Misal, R. B. Tokas, D. D. Shinde, J. V. Ramana, Sanjay Raiand N. K. Sahoo, Applied Surface Science, **2015**, 353, Pages 459–468.
4. “Study of ZrO_2 thin films deposited at glancing angle by magnetron sputtering under varying substrate rotation”, R. B. Tokas, S. Jena, J. S. Mishal, K. Divakar Rao, S. R. Polaki, C. Pratap, D. V. Udupa, S. Thakur, Sanjiv Kumar and N. K. Sahoo, (In Press).
5. “X-ray absorption fine structure studies of obliquely deposited HfO_2 thin films”, R. B. Tokas, A. K. Yadav, S. N. Jha and D. Bhattacharyya, S. Thakur, and N. K. Sahoo (communicated).

Conferences

1. "Glancing angle deposition of SiO_2 thin film microstructures: Investigations of optical and morphological properties", R. B. Tokas, S. Jena, P. Sarkar, S. Thakur, N. K. Sahoo, AIP Conf. Proc., **2014**, 1591, 1045-1047.
2. "Comparative studies of optical & elastic properties of ZrO_2 thin films prepared under normal and oblique incidence deposition geometries", P. Sarkar, R. B. Tokas, S. Jena, S. Thakur, and N. K. Sahoo, AIP Conf. Proc., **2014**, 1591, 1051-1053.
3. “Oblique Angle Deposition of HfO_2 Thin Films: Investigation of Optical and Microstructural Properties”, R. B. Tokas, S. Jena, S. Thakur and N. K. Sahoo, 3rd Int. Conf. on Phy. at Sur. and Interfaces, **2014**.
4. "Spectroscopic ellipsometry investigations of optical anisotropy in obliquely deposited hafnia thin films", R. B. Tokas, Shuvendu Jena, S. Maidul Haque, K.

Divakar Rao, S. Thakur, and N. K. Sahoo, AIP Conf. Proc., **2016**, 1731, 060007.

5. "Development of broadband antireflection coating for laser and spectroscopic applications by exploiting oblique angle deposition of SiO_2 thin films", DAE-BRNS National Laser Symposium (NLS-25), KIIT University, Bhubaneshwar, Odisha, India (December 20-23, **2016**).

PUBLICATIONS OTHER THAN THESIS

1. "Omnidirectional photonic band gap in magnetron sputtered TiO2/SiO2 one dimensional photonic crystal", S. Jena, R. B. Tokas, P. Sarkar, J. S. Misal, S. Maidul Haque, K. D. Rao, S. Thakur, N. K. Sahoo, Thin Solid Films **2016**, 599, Pages 138–144.
2. "Effect of O 2/Ar gas flow ratio on the optical properties and mechanical stress of sputtered HfO2 thin films", S. Jena, R. B. Tokas, J. S. Misal, K. Divakar Rao, D.V.Udupa, S. Thakur, N.K.Sahoo, Thin Solid Films, **2015,** 592, Pages 135-142.
3. "A probe into compositional and structural dependence of optical properties of lanthanum fluoride films prepared by resistive heating", P. Rao, S. Kumar, R. B. Tokas, N. K. Sahoo, Nuclear Instruments and Methods in Physics Research, Section B: Beam Interactions with Materials and Atoms , **2015**, 342, Pages108-115.
4. "Stoichiometry dependent inter diffusion and structural evolution in Al-Ni multilayer", M. Swain, S. Singh,, S. Basu,, D. Bhattacharya,, R. B. Tokas, M. Gupta, Journal of Alloys and Compounds, **2015**, 631, 46-51.
5. "Optical properties and laser damage threshold of HfO2-SiO2 mixed composite thin films", S. Jena, R. B. Tokas, N. M. Kamble, S. Thakur and N. K. Sahoo Applied Optics, **2014**, **53**, Pages 850-860.
6. "Investigation on the adsorption characteristics of sodium benzoate and taurine on gold nanoparticle film by ATR-FTIR spectroscopy", Naveen Kumar, S. Thomas, R. B. Tokas, R. J. Kshirsagar, Spec. Acta Part A: Molecular and Biomolecular Spectroscopy, **2014**, 118, Pages 614–618.
7. "Surface roughness and interface width scaling of magnetron sputter deposited Ni/Ti multilayers", M. Haque, S., Biswas, A., Bhattacharya, D., Tokas, R. B., Bhattacharyya, D. Sahoo, N. K., J. of App. Phy., **2013**, **114**(10), 103508.

8. “Investigation of elastic and optical properties of electron beam evaporated ZrO2-MgO composite thin films”, S. Jena, R. B. Tokas, N. M. Kamble, S. Thakur, D. Bhattacharyya and N. K. Sahoo, Thin Solid Films, **2013**, 537**,** Pages 163-170.
9. “Post analyses of multilayer interference filter using numerical reverse synthesis and Rutherford backscattering spectrometry”, N. K. Sahoo, Sanjiv Kumar, R. B. Tokas, S. Jena, N. M. Kamble, S.Thakur and G. L. N. Reddy, Applied Optics, **2013**, 52, Pages 2102-2115.
10. “Investigation of dispersive optical constants and morphological parameters of composite (HfO2)(1-x):(SiO2)(x) thin films using Tauc-Lorentz-Urbach model”, R. B. Tokas, S. Jena, P. Sarkar, S. Thakur and N.K. Sahoo, 59th DAE-BRNS Solid state physics symposium, **2015**.
11. “Achieving omnidirectional photonic band gap in sputter deposited TiO2/SiO2 one dimensional photonic crystal”, S. Jena, R. B. Tokas, P. Sarkar, S. MaidulHaque, J. S. Misal, K. D. Rao, S. Thakur and N. K. Sahoo, AIP Conf. Proc. **2015**, 1665, 060018.
12. “Phase Modulated Spectroscopic Ellipsometry and Grazing Angle X-ray Reflectivity Studies of ZrO2MgO Thin films Prepared by Reactive EB Evaporation”, R. B. Tokas, S. Jena, A. Biswas, S. Thakur and N. K. Sahoo, NLS-22, **2014**.
13. “Effect of substrate temperature on optical and morphological properties ZrO2-MgO thin films”, R. B. Tokas, S. Jena, N. M. Kamble, S. Thakur and N.K. Sahoo, , AIP Conf. Proc., **2013** ,1512 784-785.
14. “Investigation of pulse laser induced damage threshold & morphological evolution in ZrO2-MgO composite optical interference coatings”, R. B. Tokas, S. Jena, S. Thakur and N. K. Sahoo, , XXXVII National Symposium of Optical Society of India, **2013**.
15. “Magnesia-alumina-zirconia ternary composite: an emerging candidate for high power laser interference multilayer coatings”, R. B. Tokas, S. Jena, S. Thakur and N. K. Sahoo, 21st National Laser Symposium, **2013**.

DEDICATIONS

This thesis is dedicated to my family

ACKNOWLEDGEMENTS

First and foremost, I would like to express my deep and sincere gratitude to my thesis supervisor Dr. N. K Sahoo for his guidance, constant support, and encouragement. His wide knowledge in the field of multilayer thin film and logical way of dealing with scientific problems has benefited me a lot in the completion of this dissertation. I am also grateful to him for reviewing my thesis critically.

I would like to extend my sincerest thanks to Dr. S. Thakur for his guidance, valuable suggestions, critical analysis, support and encouragement. I also gratefully acknowledge the help rendered by Shri Shuvendu Jena during the growth of my thesis. I am also thankful to all the colleagues of Atomic and Molecular Physics Division, BARC for their help and support. I would like to acknowledge my collaborators for their support in several experiments/measurements and discussions.

It gives me immense pleasure to thank the members of the doctoral committee Prof. D. S. Patil (Chairman), Prof. S. C. Gadkari (Member) and Prof. Saibal Basu (Member) for their critical review and suggestions during the progress review and pre-synopsis presentation.

Finally, I owe my unfeigned gratitude and indebtness to my parents for all they have done. Above all I would like to thank my wife and kids who have always rendered their unconditional love and support. I express my sincere thanks to all my friends for their kind help and pleasurable company for making the life enjoyable.

CONTENTS

SYNOPSIS

Oblique angle deposition (OAD) has been attracting researchers in recent years due to their demanding applications in photonic crystals, energy harvesting and storage devices, fuel cell and hydrogen storage, wetting and micro fluidics, optical rugate devices, humidity sensors, micro-electronics, and thermal barriers coatings etc. From optical application point of view, porous micro-structured thin films achieved through OAD route are being explored and experimented for fabricating interference filters using single optical materials by varying refractive index across the film thickness. The refractive index variation is achieved by changing the angle of deposition which results in varying porous microstructure due to change in atomic shadowing and limited ad-atom diffusion during growth with or without substrate rotation. When this angle of deposition reaches $\geq 80^{o}$, it is termed glancing angle deposition (GLAD) which depicts unique properties different from normally deposited films. By employing substrate rotation and varying deposition angle, different microstructure patterns like pillar, helix, zigzag, erect columns etc., have been achieved successfully. For optical applications, researchers have developed several interference thin film devices, viz., (i) multi-stop band interference rugate filter, (ii) optical rugate filters for light trapping in solar cells, (iii) single layer antireflection coating, (iv) selective polarization transmission filter etc. For such devices, researchers have used oblique angle depositions of several oxides viz., TiO_2, SiO_2, HfO_2, ZrO_2, and Ta_2O_5. OAD of such optical thin films have been investigated for their optical, structural and morphological properties and their dependency on angle of deposition, substrate temperature, rate of deposition and other process parameters have been reported. However, it is difficult to generalize such studies for all optical materials deposited by different methodologies in OAD configuration.

It is well known that HfO_2, ZrO_2 and SiO_2 are the mostly used oxides for fabricating optical multilayer devices for high power laser and various spectroscopic applications due to their excellent optical properties and high laser induced damage resistance. Some researchers have reported OAD of such films but extensive study of their mechanical stability, residual stresses, complete morphological and optical characterization and correlation among different properties has not yet been reported. In the present thesis, an extensive study of elastic, optical, morphological, structural and micro-structural properties of oblique angle deposited HfO_2, ZrO_2 and SiO_2 thin films by EB evaporation and sputtering is reported. The thesis is organized in seven chapters to discuss different aspects of the present work. The contents of the chapters are summarized as follows.

Chapter:-1. Introduction

The chapter begins with an introduction to OAD and the importance of OAD in the field of thin film interference devices has been discussed. A literature survey based on the works published by researchers on OAD has been presented and further scopes for new investigations have been discussed. Finally an introduction to the optical materials investigated in the present thesis has been presented. The organization of the rest of the thesis has also been discussed in this chapter.

Chapter:-2. Experimental techniques

This chapter begins with an introduction to the different deposition techniques used for the OAD of various oxide thin films. Actual deposition systems used for the growth of the films discussed in this thesis have also been discussed. Subsequently, various characterization techniques used in the present work have been described and the important information intended from these measurements have also been discussed. The techniques include atomic force microscopy (AFM), atomic force acoustic microscopy (AFAM), UV-VIS-NIR

spectrophotometer, spectroscopic ellipsometry, grazing angle X-ray reflectrometry (GIXR), grazing angle X-ray diffraction (GIXRD), Extended X-ray absorption fine structure spectroscopy (EXAFS), and field emission electron microscopy (FESEM).

Chapter:-3. Oblique angle deposition of HfO_2 thin films by EB evaporation

This chapter describes the importance of characterization of elastic, optical, and morphological properties of obliquely deposited HfO_2 thin films deposited by EB evaporation. Effect of angle of deposition on local structure of HfO_2 thin films has also been assessed by performing EXAFS experiments. HfO_2 thin films have been deposited on Si (100) and fused silica substrate at several oblique angles of depositions. Such OAD films possess porous micro-structures and their mechanical and environmental stabilities are important issues. In order to assess mechanical stability of such thin films, indentation modulus and microstructural properties have been studies by using various characterization tools. FESEM cross-sectional morphology shows highly porous tilted columnar microstructure in the film deposited at glancing angle of 80º. Porosity decreases as the angle of deposition decreases. Variation of film density with tilt angle has been obtained through GIXR measurements. It is observed that indentation modulus obtained from AFAM measurement is least with a value of 42 GPa for a GLAD film (80º) and highest for normally deposited film with value 221 GPa. It is concluded that the trend of decreasing indentation modulus of HfO_2 thin films is an attribute of increase in porosity with angle of deposition and porosity variation is the consequence of change in microstructure of films due to change in growth conditions.

Optical and morphological properties of such films are strongly dependent of angle of deposition due to varying micro-structure with the angle of deposition. For optical applications, surface of thin films/coatings plays an important role in terms of light scattering. Hence it is indispensible to explore morphological and optical properties of such films. For the same HfO_2 films as discussed above, effect of angle of deposition on micro-roughness

parameters and optical properties has been investigated extensively through extended power spectral density measured from AFM and optical transmission measurements. Among all the films, GLAD film (80° deposition angle) exhibits highest grain size and intrinsic RMS surface roughness. Intrinsic roughness and fractal spectral strength obtained from the analysis of extended power spectral density follow the similar trend with deposition angle. Behavior of surface morphological statistical parameters and refractive index with deposition angles have been explained by the combined effect of atomic shadowing, re-emission of ad-atoms and diffusion of ad-atoms.

Chapter:-4. Glancing angle deposition of HfO_2 thin films by magnetron sputtering

In this chapter, GLAD HfO_2 thin films have been explored with respect to two vital deposition parameters visualizing deposition angle and target to substrate distance, D_{TS} in the range 70-125 mm. From morphological, optical and structural studies of such films through AFM, ellipsometric and GIXRD measurements following observations could be made.

(1). At optimum distance D_{TS} = 110 mm and at 82° angle of deposition the film exhibits prominent nanostructures as observed from AFM image.

(2). At lower D_{TS} (70-90 mm), the grains obtained from AFM imaging, are elliptical in shape and as D_{TS} increases the surface grains become circular in shape. The fact has been explained in light of the variation in ad-atom kinetic energy.

(3). The grain area has initially decreased with increase in D_{TS} in the range 70 to 110 mm and then increased with the increase in D_{TS} from 110 mm to 125 mm which is in accordance with the trend of deposition rate. The competition between deposition flux density and the sticking coefficient has led to minimum deposition rate and hence minimum grain area at D_{TS}=110 mm.

(4). The effective refractive index follows almost similar trend as that of deposition rate except for the fact that at 110 mm of D_{TS}, the film deposited at 82° exhibits lower refractive

index compared to that deposited at 86°. At 86° angle and 110 mm of D_{TS}, the formation of amorphous crystallographic structure is responsible for relatively higher index compared to that at 82°.

(5). Crystallographic structural study of the films shows that all the films have formed in polycrystalline monoclinic phase. At lower $D_{TS,}$ the crystallinity has improved with an increase in deposition angle due to the reduction in deposition rate which helps in organizing the atoms in a more crystalline form.

Chapter:-5. Glancing angle deposition of ZrO_2 thin films

This chapter has been divided in two parts:

I. Glancing angle deposition of ZrO_2 thin films by magnetron sputtering:

In this work, a set of ZrO_2 thin films have been deposited in GLAD (82º) configuration at varying substrate rotation. For comparison, ZrO_2 film was also deposited at 0º angle. Refractive index estimated from ellipsometric measurement shows an interesting decreasing behavior with substrate rotation and has been explained in the light of varying columnar structure with substrate rotation. Refractive index of GLAD ZrO_2 films varies between and 1.901 to 2.011. Normally deposited (ND) film exhibits refractive index value of 2.178 which is substantially greater than that of GLAD films. Lowering in refractive index of GLAD films is the attribute of dominant atomic shadowing at glancing angles. Further, correlation length which is the representative of surface grain size obtained from AFM measurement displays a decreasing trend with substrate rotation. The trend has also been attributed to the varying columnar microstructure. All the GLAD ZrO_2 films possess 4 to 5 order greater surface RMS roughness than ND films. Dominant atomic shadowing is responsible for high roughness of GLAD films. Both GLAD and ND ZrO_2 thin films exhibit preferential growth of monoclinic phase oriented in different directions. GLAD films also depict a tetragonal peak which has been attributed to the fine nano-crystallite size (~13 nm). Residual stress in such films depicts

a switching from large compressive to small tensile stress as the deposition angle changes from normal to glancing angle. The GLAD films show an increasing trend of stress with substrate rotation which has been explained in terms of varying inter-molecular forces with inter-columnar distance.

II. Glancing angle deposition of ZrO_2 thin films by EB evaporation:

In this part of the chapter, ZrO_2 thin films have been deposited on fused silica substrate by EB evaporation in normal as well as OAD configurations (82º). Refractive index of the films has been estimated by fitting the measured transmission spectra with suitable theoretical dispersion models. The OAD film shows high porosity with refractive index of 1.40. Porous structure of the film again has been confirmed by AFM image which depicts a highly porous surface morphology with bigger grains and high surface RMS roughness compared to ND film. Elastic modulii of indentation are 74 GPa and 160 GPa for OAD and ND films respectively. Such a high decrease in indentation modulus for GLAD film is the consequence of increased porosity due to tilted columnar growth.

Chapter:-6. Oblique angle deposition of SiO_2 thin films by EB evaporation

In this chapter, optical and morphological properties of OAD SiO_2 thin films deposited at angle 75°, 70 and 0° have been investigated. The refractive index data obtained from suitable modeling of transmission spectra has been found to be 1.14, 1.25 and 1.45@600nm for SiO_2 films deposited at angle 75°, 70 and 0° respectively. The reduction in refractive index for obliquely deposited SiO_2 thin films is the consequence of dominant atomic shadowing. Using the refractive index value obtained for OAD SiO_2 films, a 2-layer design of SiO_2 thin films deposited at an oblique angle of 70° and 75° on both sides of glass substrate (BK7) have been chosen to fabricate a broad band antireflection coating having an average transmission more than 99.2% in a band of 450 nm. Contact angle measurements confirm highly wetting

character of the developed antireflection coating having contact angle 4.8°. Low contact angle of such coating is due to high roughness and irregular variations of height over the surface. Such coatings can be applied to solar panel encapsulation to give antireflection as well as self-cleaning effects which can lead to the enhancement of efficiency.

Chapter:-7. Summary and Future Prospects

The highlights of the work done under this thesis may be summarized as follows:

(1) OAD facilities using EB evaporation and sputtering deposition technique has been set up.

(2) Quantitative assessment of indentation modulus and micro-structural properties of obliquely deposited HfO_2 thin films have been carried out.

(3) Local structure of GLAD HfO_2 thin has been studied by EXAFS measurements.

(4). Effect of angle of deposition on micro-roughness parameters and optical properties of HfO_2 thin films deposited by EB evaporation have been carried out.

(5). Study of Hafnium Oxide thin films deposited by RF magnetron sputtering under glancing angle deposition at varying target to substrate distance has been done.

(6). Optical, morphological, structural, micro-structural properties and residual stresses of ZrO_2 thin films deposited at glancing angle by magnetron sputtering under varying substrate rotation have been explored. Results obtained have been compared with ND ZrO_2 films.

(7). Development of broadband antireflection coating using OAD of SiO_2 thin films.

In future, effect of substrate temperature and deposition pressure could be explored for oblique angle deposition of various optical thin films. Influence of co-deposition in OAD configuration could also be investigated. Finally OAD could be used to fabricate various stable rugate structure based interference devices for optical applications.

LIST OF FIGURES

LIST OF TABLES

CHAPTER 1: INTRODUCTION

1.1. Introduction

Porous coatings have potential applications in optical devices, sensors, energy harvesting devices, solar cells, thermal barrier coatings, micro fluidics etc. To fabricate such coatings, oblique angle deposition (OAD) is the most reliable, precise and established method [1]. OAD thin films have been a field of interest for researchers and technologist for years due to their novel and fascinating physical and chemical properties. This technique [2-4] generally utilizes physical vapour deposition in which incoming flux of ad-atoms is allowed to strike a substrate at an angle with or without substrate rotation**.** By employing the variation in deposition parameters such as substrate rotation (ω), angle of deposition (α), rate of deposition, and substrate temperature (Ts), different microstructures depicting unique physical and chemical properties could be achieved. OAD of thin films generally work at angle ≥ 60° and when this angle of deposition reaches ≥ 80º, it is termed glancing angle deposition (GLAD). By employing substrate rotation and varying deposition angle, different microstructure patterns like pillar, helix, zigzag, erect columns etc., have been achieved [5-7]. OAD thin film deposition may be treated as a combination of top-down and bottom-up nanofabrication process [1, 3]. During conventional film deposition, a flux of atoms in vapour phase strikes upon a substrate normally and condense there to produce a dense solid thin film. In OAD/GLAD, the substrate is inclined to vapour atoms, thus creating oblique deposition geometry. Atoms condense on the substrate spontaneously to form microscopic nuclei. Ballistic shadowing [1, 3] prevents incoming vapour from condensing into regions behind the nuclei, causing the nuclei to develop into columns that tilt towards the vapour source and hence leads to increased voids or porous micro structure. This porosity can be controlled and even be varied along film thickness in a designed manner by changing substrate tilt and

rotation in a design fashion. For example, rugate structures can be fabricated using single material by varying deposition angle so that refractive index varies continuously in a predefined manner along thickness [8-10].

1.2. Theory of OAD/GLAD

1.2.1. Ballistic shadowing

Ballistic shadowing for ad-atoms is the main mechanism which accounts for the porous columnar microstructure of thin film fabricated by OAD. Ballistic shadowing works in case of well collimated incoming vapor of ad-atoms. Shadowing effect becomes poor for a large angular spread of flux of ad-atoms. Either large distance between substrate and vapor source or physical masking which allow a small part of un-collimated flux coming to the substrate, can offer favorable conditions for prominent shadowing effects. With the increase of distance between substrate and vapor source, incident flux collimation becomes better resulting in prominent shadowing effects for a substrate having fixed size. Although for longer distances between substrate and source, good vacuum conditions ($\leq 10^{-4}$ mbar) inside the chamber are required to eliminate the scattering of incoming atoms with the molecules of residuals inside the vacuum chamber. To produce high-quality structures, mean free path of atoms should be larger than the source–substrate distance. Mean free path (simple formulation) of air molecule at room temperature is given as follows [11]

$$l = \frac{5x10^{-3}}{P} \text{ cm} \qquad (1.1)$$

Since in electron beam (EB) or thermal evaporation, deposition can be carried out relatively at lower pressures, longer mean free paths could easily be achieved [12]. Therefore, EB evaporation is widely used for OAD/GLAD techniques. However, there are some types of coating materials such as alloys, which cannot be deposited properly by such techniques. For such cases, sputtering and pulsed laser deposition technique could be used, but at the cost of a

wider angular distribution due to large target size and scattering from the sputtering gas. For wider angular processes, a physical screen which allows a subset of incident vapor flux can restore collimation [3, 13]. GLAD conditions were even achieved by researcher at higher pressures of 0.1 Torr to deposit ZnO thin films by pulsed laser deposition [14].

1.2.2. Film nucleation and column growth

Thin film growth occurs in several phases: (1) Vapor condensation and nucleation (2) Island formation and growth (3) Island coalescence (4) Agglomeration and continuous structure formation and (5) Thickness growth.

The evolution of film structure through these growth phases is described by Chopra [15], Heavens [16] and Milton Ohring [17] in detail. Here nucleation and growth process of only OAD/GLAD thin films is discussed. In the initial phase of vapor condensation and nucleation, incoming vapor particles (atoms/molecules) arrive at the substrate and are quickly physiso-absorbed via several mechanisms on the surface. Depending on the substrate temperature and atom-substrate interaction conditions, such adsorbed ad-atom diffuses on the surface. This diffusing ad-atom can bind with other ad-atoms or clusters to form macroscopic nuclei on the substrate surface. Ad-atoms from such randomly placed nuclei over substrate can re-evaporate also depending on substrate temperature. So, there is a competition between growth and condensation and detachment of ad-atoms from nuclei. With the growth of nuclei, re-evaporation rate of ad-atoms decreases and finally nucleus attains a critical size. The nuclei which attain critical size are small having size of order of few atoms, grow fast and become dominant features over the substrate. Further expansion of these nuclei follows one of the three growth modes:

(1) Volmer–Weber growth: In this mode, atoms are strongly bound to each other and weakly bound to the substrate resulting in 3D island formation.

(2) Frank–van der Merwe growth: In this mode, substrate-ad-atom interaction dominates leading to 2D layer formation.

(3) Stranski–Krastanov growth: It is mixed growth mode. First few 2D mono-layers are followed by 2D island formation. Such switching in growth occurs due to strain build-up, change in lattice symmetry and molecular orientation.

Since Volmer-Weber growth model roughens the substrate having no initial feature, is most important for OAD. Any defect on substrate accelerates roughening. Initial stage of film growth in OAD configuration with α as incident angle of vapor flux with respect to substrate is shown schematically in Fig. 1.1 (a). This randomly organized nucleus further grows in columns and generates shadows. Formation of columnar structure is essentially governed by structure zone model-I [7-10] in which substrate temperature (T_s) is related to melting point (T_m) of deposited material by following relation:

$$\frac{T_S}{T_M} < 0.3 \qquad (1.2)$$

Thus in OAD, nuclei grow in to column and cause the shadows (voids) formation as shown in Fig. 1.1 (b). Such formed columns and voids have size distribution. It results in the screening of some of the nuclei by neighboring nuclei from incoming ad-atoms. In this way, growth of screened nuclei is suppressed as shown in Fig. 1.1 (c). After some time, smaller and suppressed nuclei become completely shadowed and stop growing as presented in Fig. 1.1 (d). Such columns are called extinct columns and this process continues throughout the GLAD thin film growth. Finally top of the nuclei grow in to columns, tilted towards incoming vapors of ad-atoms. Tilt angle β is defined in Fig. 1.1 (d) and it is always less than or equal to incoming vapor angle α. There can be multiple value of β depending angular distribution of incoming vapors.

1.2.3. Column tilt Angle in OAD

Growth of tilted columnar micro-structure in OAD of thin films is governed by several process parameters such as substrate temperature, angle of deposition, rate of deposition,

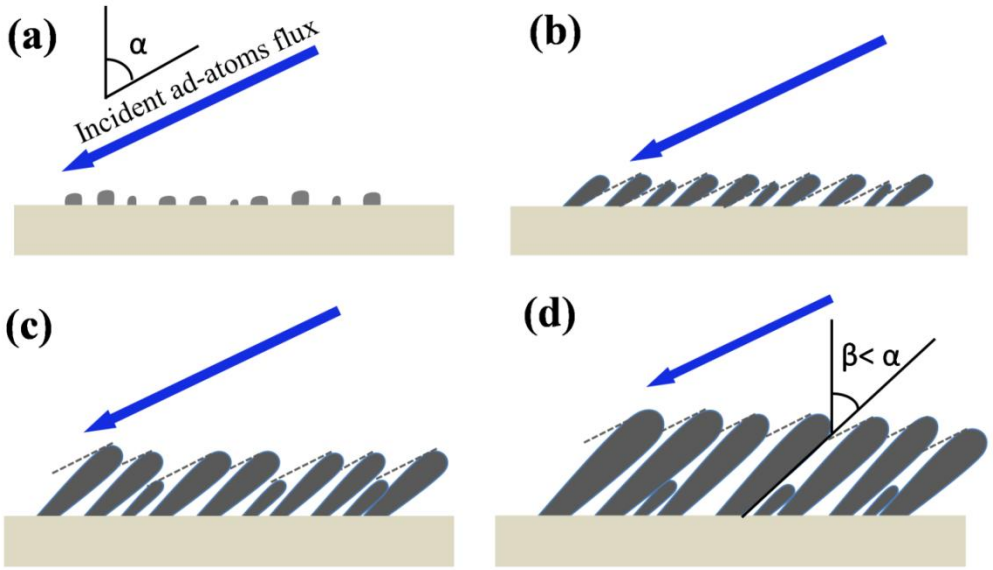

Fig. 1.1: *Different state of nucleation in oblique angle deposition*

chamber pressure, substrate and vacuum composition. Dependency of column tilt angle β on angle α is not governed by any single rule. A relationship between α and β determined experimentally for evaporated Al thin films, only offers a general guideline. This relation was given by Nieuwenhuizen *et al*. [18] and popularly known as tangent rule is as follows:

$$\beta = \tan^{-1}\left(\frac{1}{2}\tan\alpha\right) \tag{1.3}$$

Tangent rule was further modified by Hodgkinson *et al*. [19] by adding an addition fitting parameter. However, tangent rule gives satisfactory results up to α=60º and deviates from experimental data for high oblique angles. Tait *et al.* [20] used ballistic deposition model which describes thin film column angle behavior closely matching with that of real film. They considered sequential deposition of hard discs (ad-atoms) and such hard discs diffuse over some distance after initial contact with the film; but diffusion is limited to a single

column. The most general formulation developed by considering shadowing from one neighbor is given by [20]:

$$\beta = \alpha - sin^{-1}\left[(1-\cos\alpha)/2\right] \quad (1.4)$$

The discussed model can only provide first order approximation of expected behavior of tilt angle β. Actual tilt angle in GLAD films may be perturbed by several factors such as substrate temperature, deposition rate, chamber pressure, different material, interaction between substrate and deposited material [19, 21-25]. Fig. 1.2 (a) shows the comparison of measured and calculated values of angle β for EB evaporated HfO_2 thin films. Values of angle β were measured from FESEM cross-sectional morphology and calculated from tangent and Tait's [20] rule. For higher incident flux angle, measured value of β is close to that predicted from Tait's cosine rule.

1.2.4. Film Density

Since OAD films depict porous columnar structure, film density depicts a radical decrease in film density especially on higher incident angle of incoming flux. Tait *et al.* [20] derived an expression for film density using geometric model of columnar growth in OAD thin films. The film density (ρ) for OAD film in terms of deposition angle is given as follows:

$$\rho = \rho_0 \frac{2\cos\alpha}{1+\cos\alpha} \quad (1.5)$$

Here ρ_0 is the density of normally deposited thin film ($\alpha = 0^o$). Once again, this expression gives first order approximation of expected dependency of density of OAD film on angle of deposition. Exceptions of this equation for real OAD films are reported in literature [26, 27] especially near glancing angle deposition. The variation of film density on incident flux angle for EB evaporated HfO_2 thin film is shown experimentally in Fig. 1.2 (b) and then the calculated density from above equation is compared with the experimental data.

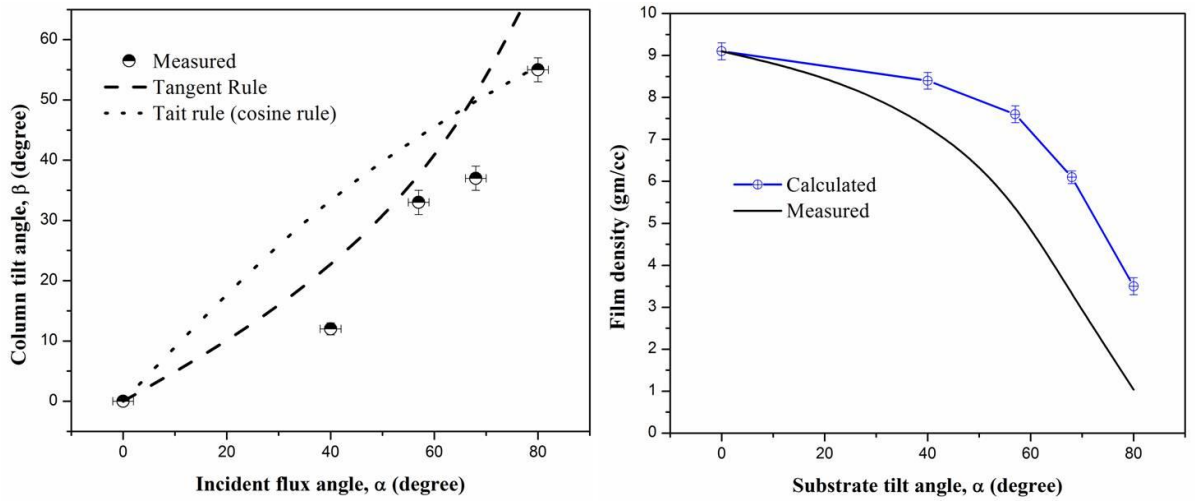

Fig. 1.2 (a): *Measured and calculated column tilt angle and (b) Measured and calculated film density as a function of vapour incident flux angle (α).*

1.2.5. Substrate motion

In OAD, two motion of substrate: substrate tilt and azimuthal rotation are exploited to fabricate various porous micros-structures. For any deposition in OAD configuration, substrate motion is defined by two motions collectively (α, ϕ). For stationary substrate (ϕ=0), slanted columnar growth occurs. Such slanted columnar growth shows biaxial anisotropy in various properties of thin films. In OAD, shadowing effects work in the direction parallel to vapour flux but there is no mechanism for limiting columnar growth in transverse direction, leading to broad columns. The columns broadening keep continue with the film growth until the columns merge with adjacent. By employing the precise and controlled change in (α, ϕ), beautiful GLAD micro and nano structure such as, helical, zigzag, straight pillars etc. [6, 7, 28, 29] can be achieved. Fig. 1.3 (a) and (b) show schematic of OAD and slanted columnar growth of HfO_2 thin films.

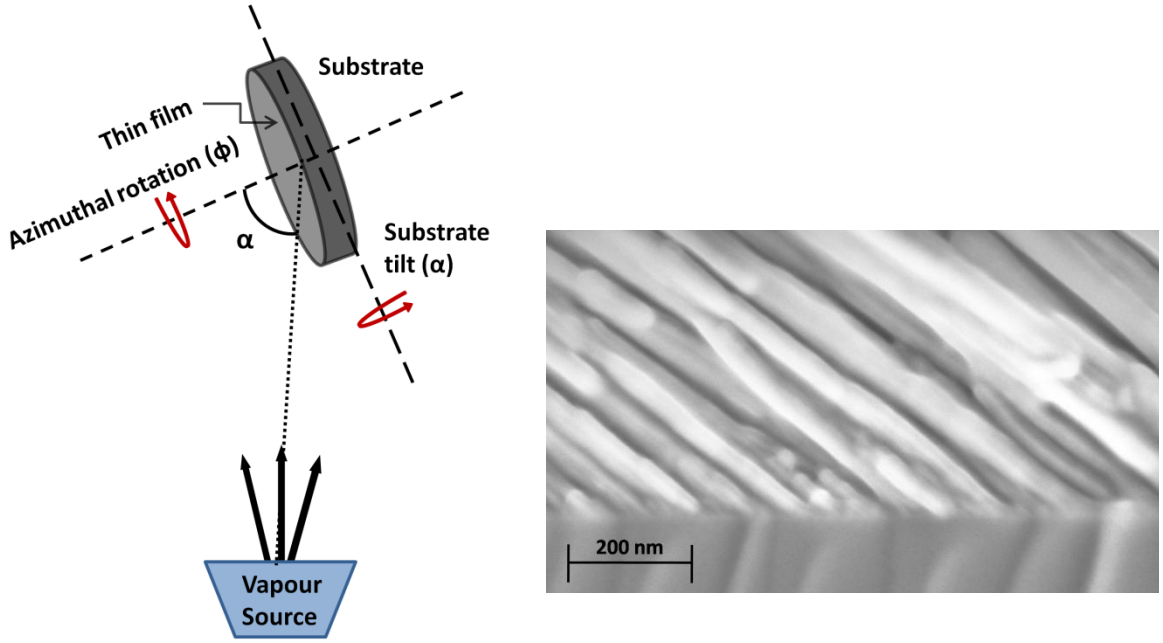

Fig. 1.3 (a): *Schematic of oblique angle deposition and* ***(b)*** *Tilted columnar structure of EB evaporated GLAD HfO_2 film as measured from field emission scanning electron microscopy.*

Rugate structure can be achieved by continuously varying tilt angle α with fixed value of substrate rotation [8-10, 30]. Continuously varying α between two extreme values leads to continuous variation in film porosity and hence refractive index in turn behaves like a high-low index stack. The advantage of substrate rotation in such coatings is to eliminate biaxial optical anisotropy [1].

1.3. Literature survey and Motivation

As discussed in section 1.1, OAD of thin films has several applications in various fields. Dominant applications of OAD films are in the field of optics and photonics. For optical applications, there are well developed theoretical models and control of microstructure on a relevant scale of optical applications. From optical application point of view, researchers have exploited the inherently developed birefringence of slanted columnar growth of several optical materials to develop wave plates and optical retarders. Oliver *et al*. [31] fabricated a quarter wave retarder using MgO GLAD thin films to be used at 351nm in vacuum

environment. Harris *et al*. [32] developed various birefrengent layers of indium tin oxide by oblique angle deposition making them transparent in visible wavelength range and electrically conducting (for flat panel applications). Andy C. Van Popta *et al*. [33] performed experiments to enhance the birefringence of OAD TiO_2 thin films. They carried out bi-deposition of TiO_2 thin films at α=60º and 70º with repetitive 180º substrate rotation. They annealed the fabricated structure between 200°C to 900ºC and achieved the doubling in birefringence ($\Delta n=0.22$). A. Lakhtakia *et al*. [34] developed multi-section chiral sculptured thin films that function as spectral reflection holes for fluid sensors applications. Refractive index profile can be tuned in OAD thin film by varying deposition angle α in a controlled manner along thickness of thin film. Many researchers have explored this to develop GLAD optical filters. As various materials can be deposited and many refractive index profiles can be realized, the GLAD process provides significant flexibility in designing optical thin film devices. K. Robbie *et al*. [35] fabricated a 50 nm band width reflection filter by using single material MgF_2. They varied refractive index of MgF_2 sinusoidaly along thickness by varying angle α between 51º and 81º. Yumei Zhu *et al*. [36] proposed theoretical formulations for depositing multi stop band filter using GLAD technique. They realized such filters by exploiting mix index profile (sinusoidal+ step) of GLAD TiO_2 thin films deposited by EB evaporation. Similar refractive index variation of GLAD TiO_2 film were used by Andy C. van Popta [30] to fabricate 15 nm band width narrow band pass rugate filter at 532 nm. Kennedy *et al*. [37] deposited glass substrate with graded index layer of GLAD SiO_2 thin film with Gaussian index profile resulting in 99.9% transmission in 46 nm band width. Apart from optical rugate filters, many researchers have reported work on 2D and 3D photonic crystal [38-43], luminescent devices [44, 45] and liquid crystal devices [46, 47] utilizing OAD/GLAD optical thin films**.** Apart from devices, various studies of OAD optical thin films have been carried out by researchers. Effect of substrate temperature, rate of deposition,

chamber pressure, effect of annealing, substrate to source distance on optical, mechanical, morphological and structural properties have been investigated.

Oxides are an important class of optical coating materials, because they generally form hard, abrasion resistant, chemically and environmentally stable films with a variety of refractive indices and high transmission spectral ranges. HfO_2, SiO_2 and ZrO_2 which are widely used oxide materials for the development of thin film multilayers based interference devices, have been selected for OAD experiments and studies in present thesis. More discussion on important properties and applications of these optical materials will be discussed in subsequent chapters.

Very few reports are available on OAD/GLAD of such oxide films [37, 48-50] and especially research on their elastic/environmental stability and correlation between different properties is scanty. An extensive study of their mechanical properties, complete morphological and optical characterization and correlation among different properties need to be explored further to understand them closely. Especially effect of variation of different process parameter on microstructure and other properties needs to be studied before the realization of devices based on such films. In the present thesis, an extensive study of elastic, optical, morphological, structural and micro-structural properties of obliquely deposited HfO_2, ZrO_2 and SiO_2 thin films by EB evaporation and sputtering is presented. Effect of process parameter such as deposition angle, substrate rotation and substrate to source distance on various film properties has been investigated.

1.4. Outline of the Thesis

In this thesis, oblique angle deposition of optical material such as HfO_2, ZrO_2 and SiO_2 has been carried out by EB evaporation and sputtering techniques. The thesis has been organized in seven chapters to discuss different aspects of the present work. The contents of the chapters are summarized as follows.

In chapter 1 which is present one, background for the work presented in this dissertation has been given. In this chapter, theory of OAD and its importance in the field optical coating and photonics has been discussed. A literature survey, introduction to materials investigated and motivation of the present thesis is presented.

Chapter 2 describes the experimental techniques which have been used to carry out experimental work presented in the thesis. It includes the deposition techniques used for depositing thin films, various characterization techniques such as atomic force microscopy, atomic force acoustic microscopy, UV-VIS-NIR spectrophotometer, spectroscopic ellipsometry, grazing angle X-ray Reflectrometry (GIXR), grazing angle X-ray diffraction (GIXRD), Extended X-ray absorption fine structure spectroscopy (EXAFS), wetting properties measurements (contact angle measurement), and field emission electron microscopy (FESEM).

Chapter 3 is devoted for OAD of HfO_2 thin films by EB evaporation. In this chapter, the influence of angle of deposition on elastic, morphological, optical, structural and microstructural properties has been studied. Effect of angle of deposition on local structure of such thin films has also been assessed by performing EXAFS experiments.

In the chapter 4, GLAD HfO_2 thin films deposited by RF sputtering have been studied. In this chapter, such films have been explored with respect to two vital deposition parameters visualizing such as deposition angle and target to substrate distance. Effect of substrate to target distance, angle of deposition on structural, morphological and optical properties has been investigated.

Chapter 5 has been divided in two parts:

I. Glancing angle deposition of ZrO_2 thin films by magnetron sputtering:

In this part of the chapter, various properties such as structure, optical properties, morphology and residual stress of GLAD ZrO_2 film has been studied with respect to substrate rotation. Such films have also been compared with normally deposited ZrO_2 thin film.

II. Glancing angle deposition of ZrO_2 thin films by EB evaporation:

In this part of the chapter, ZrO_2 thin films have been deposited on fused silica by EB evaporation in normal as well as OAD configurations (82º). A comparative study of grain structure, indentation modulus, refractive index and film porosity has been carried for normally and obliquely deposited films.

In the chapter 6, SiO_2 thin films deposited on glass and fused silica substrate in OAD configuration have been discussed along with their optical and morphological properties, and film density. The results are compared with the normally deposited (ND) SiO_2 films for the gained advantages. Further, a 2-layer design of SiO_2 thin films deposited at two oblique angles on both sides of glass substrate have been chosen to develop a broad band antireflection coating. Wetting characteristics of such films have also been tested.

Chapter 7 comprises the summary of important findings of the work carried out in the present thesis as well as the future prospects.

CHAPTER 2: EXPERIMENTAL TECHNIQUES

This chapter has been presented in two parts. Part-1 describes the deposition techniques used to deposit the thin films and in part-2, the experimental technique used to characterize the films has been presented.

2.1. Deposition Techniques

Electron beam evaporation (EB) and RF magnetron sputtering techniques have been used to fabricate the thin films studied in the present dissertation.

2.1.1. Deposition by EB evaporation

Evaporation of materials by resistive heating has many short coming like reaction of evaporant with its holder, need of very high current to heat boat, inability to evaporate refractory oxides efficiently etc. Such problems are easily overcome by using EB heating. EB evaporation is now the preferred technique for most of the materials, especially the refractory oxides [51]. EB evaporation is a form of physical vapour deposition in which evaporating material is kept in a suitable crucible (generally copper) and an intense beam of electrons bombards the evaporant. Electron beam heat the central portion of the exposed surface of evaporant and there is reasonably long path for thermal conduction in evaporating material to hearth or crucible. In this way, crucible can be kept at much lower temperature than the melting point of evaporant leading to the non-occurrence of reaction between hearth and evaporating material. In this process, crucible is normally water cooled and copper is normally preferred as crucible material due to its high thermal conductivity.

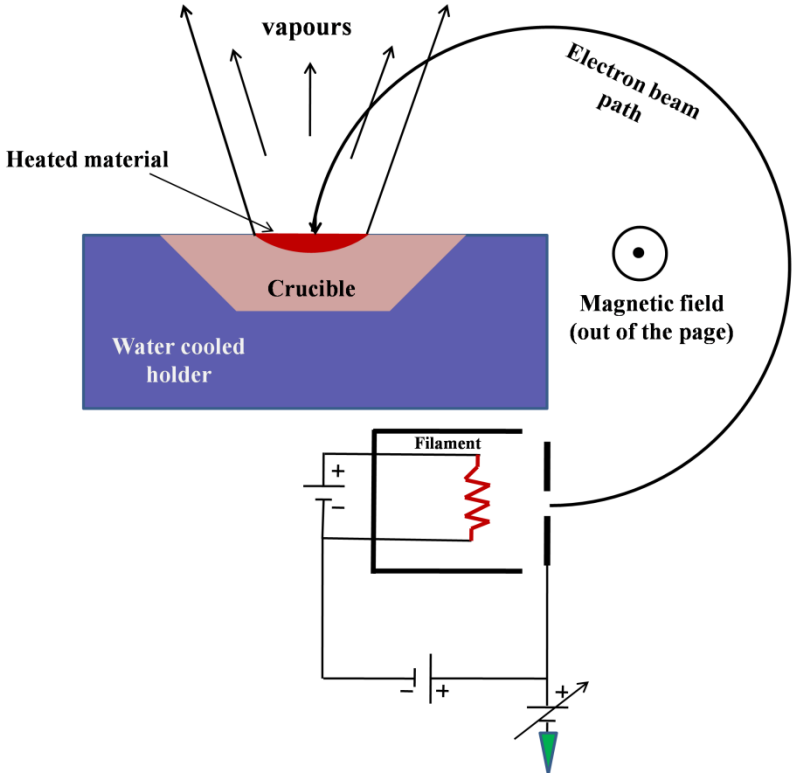

Fig. 2.1: *Schematic diagram of 270º deflection EB gun module.*

The electrons are emitted from a tungsten filament and are guided to hit evaporant by a high potential (6-10 kV). Various types of electrodes and forms of focusing arrangement have been used at different times but bent-beam type of arrangement of gun has been adopted universally. The crucible is kept at the ground potential (grounded) and the filament is kept at high negative voltage with respect to crucible. The filament and electrodes are placed under the crucible to keep it away from the reach of the evaporant vapours. The thermionically emitted electron beam from cathode is bent greater than a semi-circle (270°) by using magnetic field and focused on the material in the crucible. A typical EB source of such type is shown in Fig. 2.1. This eliminates the problems of early EB systems that had filaments in line of sight of the crucible and hence considerably shortened life due to reactions with the evaporant. The position of the spot is controlled and scanned over the crucible by using supplementary magnetic fields derived from coils. Beam scanning increases the area of heated material. Such type of EB evaporation arrangement reduces the temperature necessary

to maintain the same rate of deposition and improves the efficiency of use of the material in the crucible. EB is particularly useful to evaporate materials that possess very high evaporation temperatures and/or the materials that react with boat. The materials like refractory oxides viz., ZrO_2, HfO_2, Al_2O_3, and SiO_2 can easily be evaporated by EB evaporation. Not all electrons are used to heat the material. Some of them are reflected, converted in to secondary electrons and X-rays which may perturb the microstructure of growing film.

For fabricating the film for present thesis, Vacuum Technique Dressen (VTD), Germany make, a fully automatic Vera 902 EB deposition system has been used. Actual photograph and schematic of complete EB deposition system are in shown Fig. 2.2 (a) and (b). Fig. 2.3 (a) and (b) display oblique angle deposition set-up incorporated in EB deposition system and schematic of oblique angle deposition set-up respectively.

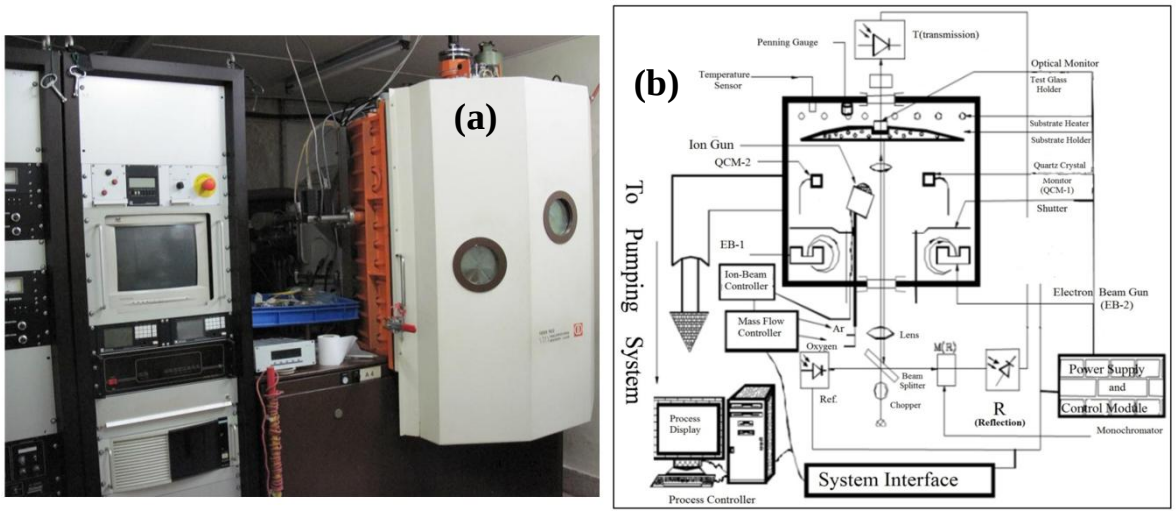

Fig. 2.2 *(a): Actual photograph and (b) Schematic diagram of used EB deposition system.*

This system has two EB guns of 8 kW capacities. There are 4 pockets to contain evaporant installed with each gun. Substrate holder is dome shaped and can be rotated at varying speed to produce thin films of uniform thickness. A radiation heater is kept just above the substrate

holder to heat substrates (up to 450°C). Substrate heating is required to get good adhesion of film with substrate and/or optimum optical properties. Rate of deposition and

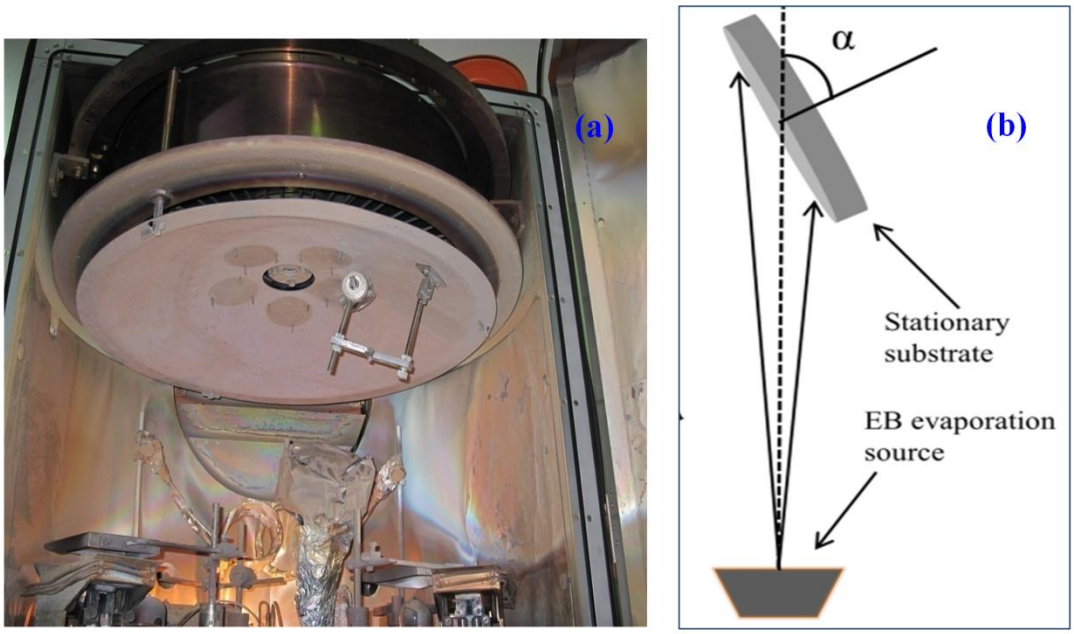

Fig. 2.3: *(a) Dual gun EB deposition system with oblique angle deposition facility, and (b) Schematic of oblique angle deposition set-up.*

thickness of the growing film are controlled by XTC quartz crystal monitors (Inficon make). Leybold make OMS 2000, optical monitor is alternatively used to monitor thickness of optical thin films. Rate of evaporation can be varied by changing filament heating current and automatically be done by the feedback from quartz crystal monitor. For oblique angle deposition, a separate substrate adopters of different sizes were used to bring substrate surface at desired angle to EB beam. Vacuum inside the chamber is achieved by the combination of diffusion, rotary and roots blower vacuum pumps.

2.1.2. Deposition by sputtering

Sputtering process has been used for many years to deposit hard coatings (wear-resistant coatings), low friction coatings, corrosion resistant coatings, decorative coatings and coatings with specific optical or electrical properties [52]. In the basic sputtering process as shown in Fig. 2.4, a target (or cathode) plate is bombarded by energetic ions of an inert gas generated

in glow discharge plasma, situated in front of the target. Bombarded atoms transfer their momentum to target atoms by collision process. It causes the removal of target atoms by cascade phenomena. This process of removal of target atom is called sputtering.

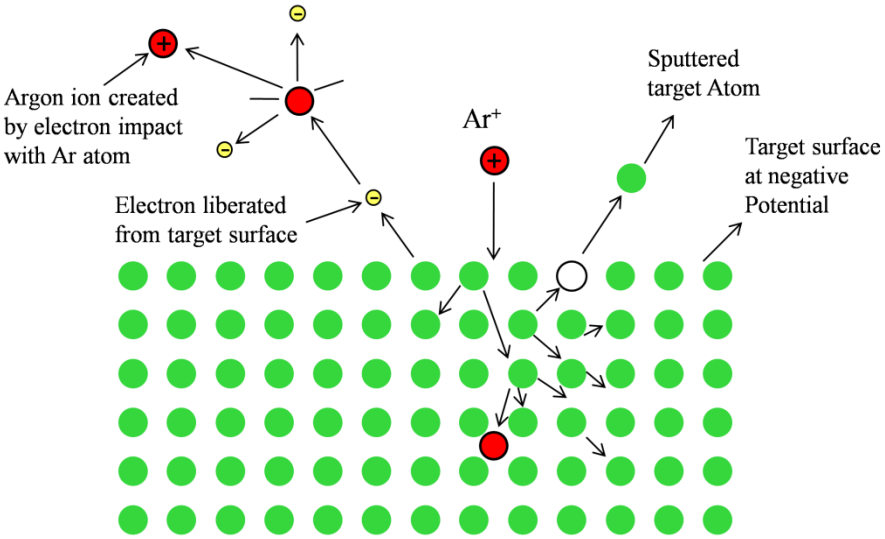

Fig. 2.4: *Basic mechanism of sputtering process.*

Sputtered atom from target may condense on a substrate to form a thin film. Secondary electrons are also emitted from the target surface as a result of the ion bombardment, and these electrons play an important role in maintaining the plasma. The basic sputtering process has been known for many years and many materials have been successfully deposited using this technique [52-54]. However, the process is limited by low deposition rates, low ionization efficiencies in the plasma, and high substrate heating effects. These limitations can be overcome by magnetron sputtering. Magnetrons make use of the fact that a magnetic field configured parallel to the target surface can constrain secondary electron motion to the vicinity of the target. The magnets are arranged in such a way that one pole is positioned at the central axis of the target and the second pole is formed by a ring of magnets around the outer edge of the target. Trapping the electrons in this way substantially increases the probability of an ionizing electron–atom collision occurring. This, in turn, leads to increased ion bombardment of the target, giving higher sputtering rates and, therefore, higher

deposition rates at the substrate. In addition, the increased ionization efficiency achieved in the magnetron mode allows the discharge to be maintained at lower operating pressures (typically, 10^{-3} mbar, compared to 10^{-2} mbar) and lower operating voltages (typically, −500V, compared to −2 to −3 kV) than is possible in the basic sputtering mode.

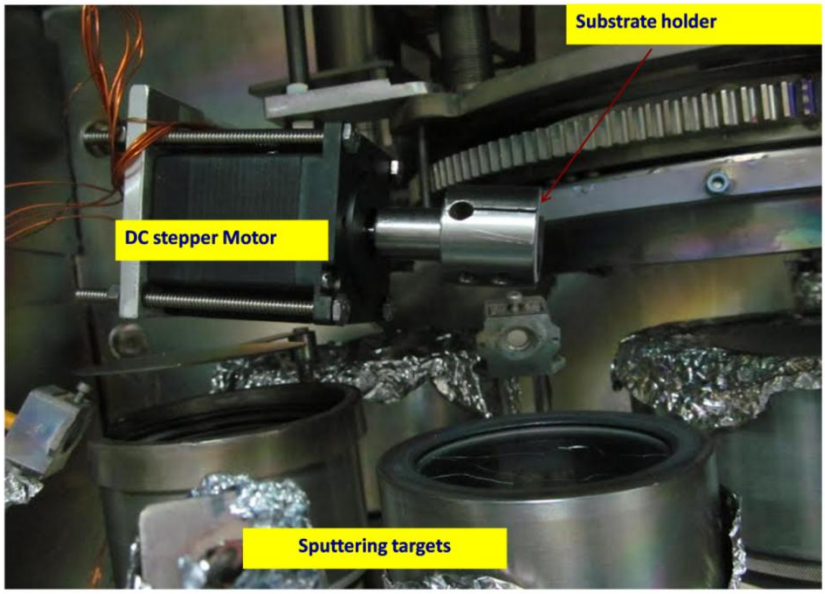

Fig.2.5: *GLAD set up for RF magnetron sputtering.*

In present dissertation, an indigenously developed, multi-magnetron sputtering system equipped with fully automatic process control modules has been used to deposit oxide thin films. It consists of 75 mm magnetrons (Angstrom Science make) compatible with bipolar pulse DC, DC and RF power supply. Substrate to target distance can be tuned between 60 to 125 mm. Capacity of DC, PDC and RF supplies are 10kW, 10kW and 1kW respectively. A turbo molecular pump backed by rotary pump has been used to evacuate the vacuum chamber. For monitoring and controlling thickness and rate of deposition, MDC-360C, multi-channel quartz crystal controller was used. The system is equipped with three mass flow controller to pass different gases (O_2, Ar, N_2) inside the chamber (for reactive sputtering). The system can also work in co-sputtering mode. For glancing angle/oblique angle deposition, a vacuum compatible motor has been installed inside the chamber to rotate and

hold substrate at desired angle with respect to sputtered atoms flux. The minimum and maximum rotation speed of the motor is 0.25 and 100 revolution per minute. For Present dissertation, RF sputtering has been employed to deposit the thin films in glancing angle deposition configuration.

2.2. Characterization Techniques

2.2.1. Atomic Force Microscopy (AFM)

Scanning tunneling microscopy (STM) is a useful tool for surface characterization for metal and semiconductors on an atomic scale [55]. Its major limitation is the need of conducting sample. In 1986, Gerd Binning, Cavin Quate and Christoph Gerber [56] proposed a new type of microscopic technique which could overcome the need of conducting sample. In this technique, forces between probe and samples are measured in atomic scale. The technique is known as AFM. AFM is a synthesis of mechanical profilometer which uses mechanical springs to sense forces and the STM which uses piezoelectric transducers for scanning. It has become one of the most important microscopic techniques used to characterize nano scale structures, surfaces and their properties. It is now an indispensable characterization tool in the field of nano science and nanotechnology and being used routinely in different research areas.

In AFM, a probe tip is attached to a cantilever spring. Under the effect of tip-sample forces, cantilever is deflected following Hook's law and the deflection is recorded by scanning the cantilever over sample surface. Fig. 2.6 shows the schematic of working principle of AFM. The cantilever deflection is detected by an 'optical lever' method and converted into an electrical signal to produce the images. In this method, a laser beam is reflected from the back side (high reflection coating) of cantilever (near free end) end. Reflected beam is incident on a position sensitive detector (generally 4 quadrant spitted photo diode). As the cantilever gets deflected, the angle of reflected beam changes and the spot falls

on a different part of the detector. The signals from the four quadrants are compared to calculate the position of the laser spot. The vertical deflection of the cantilever can be calculated by comparing the signal from the 'top' and 'bottom' halves of the detector. The lateral twisting of the cantilever can also be calculated by comparing the 'left' and 'right' halve signals from the detector. This detection system measures the cantilever defection with sub-Angstrom sensitivity. The precise scanning of tip over sample is performed by using piezo-electric tube scanners ceramics. Such scanner can move in sub-Angstrom steps in X, Y and Z-directions. To carry out accurate and noise free measurement, vibration isolation and acoustic suppression is mandatory in AFM system. The AFM cantilevers are fabricated from Si or Si_3N_4. Typical tip radius of curvature ranges from 1-20 nm. Lower radius of curvatures is required to get higher resolution.

The force F(r) between cantilever tip and sample is the basis of AFM imaging and for short distance between atom /molecules, Van der Waals forces dominates.

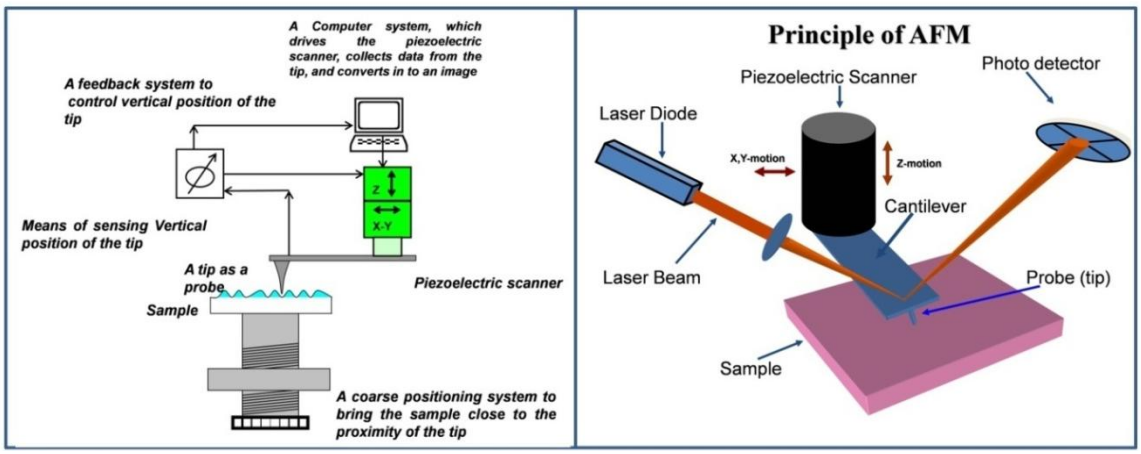

Fig. 2.6: *Schematic of working principle of AFM.*

Vander wall forces are derived from the Lenard Jones potential as follows:

$$F(r) = grad\big(U(r)\big) = \frac{d}{dr}\left(\frac{A_1}{r^{12}} - \frac{B_1}{r^6}\right) = \frac{A}{r^{13}} - \frac{B}{r^7} \qquad (2.1)$$

A and *B* are coefficients and *r* is the inter-atomic/molecular distance. Typical form of Van der Waals forces has been drawn in Fig. 2.7.

2.2.1.1. Mode of operation of AFM

AFM can be used both in static and dynamic mode. There are three modes of operation as described below.

2.2.1.1.1. Contact mode

This is static and widely used mode of AFM operation. In this mode cantilever tip is raster scanned over the surface of sample while being in touch with surface. The force between tip and sample is in the range of 10^{-9} to 10^{-6} Newton. The tip deflected as it moves over the surface irregularities. Contact mode can either be used in constant force or constant height mode but generally it is used in constant force mode. In this mode, the tip is constantly

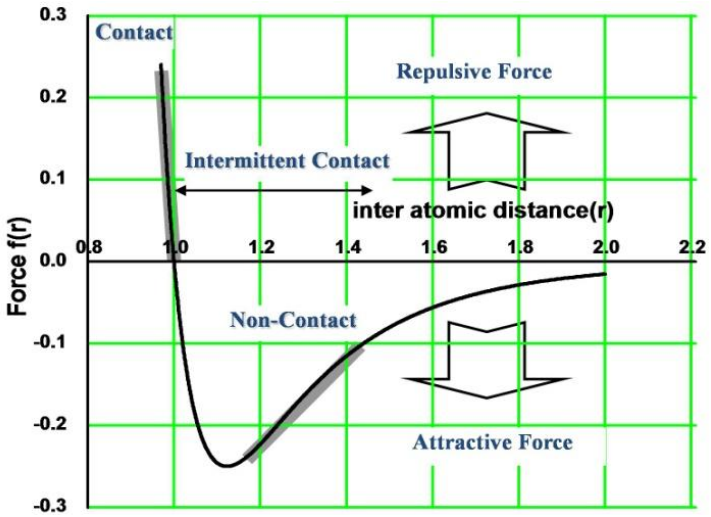

Fig. 2.7: *Dependency of force on distance between tip and sample.*

adjusted to maintain a constant deflection and hence constant distance between tip and sample surface. The movement of Z-scanner to maintain constant height between tip and sample is displayed as topographical image of surface irregularities. To maintain constant height between tip and sample, a feedback arrangement as shown in Fig. 2.6 is utilised. In case where surface is smooth, a constant height mode can be used. The advantage of constant

height mode is high scanning speeds. Resolution in constant height mode is poor. For contact mode, a relatively softer tip having low spring constant is used (~ 0.1 N/m) to avoid any surface or tip damage and to get good deflection contrast.

2.2.1.1.2. Non-contact mode (NCM)

Non-contact mode is performed at tip-sample distance of 10 to 100 nm. The force F(r) is attractive and ranges from 10^{-12} to 10^{-9} N. Obviously forces are poorer compared to contact mode leading to poor sensitivity. To make the measurement sensitive, an oscillating cantilever just above its resonance frequency (ω_r) is used. When the tip is brought closer to the sample, the resonance frequency ω_r will decrease according to $\omega_r = \sqrt{[\omega^2_0 - (1/m)(\partial F/\partial z)]}$. This induces a decrease of the amplitude of the vibration. Here ω_0 is free resonance frequency of cantilever. The amplitude/frequency is then used to control tip-sample distance and is used to generate surface topography. For this mode, a stiff cantilever having spring constant (~10 N or more) is chosen to carry out the measurement.

2.2.1.1.3. Semi-contact or Intermittent mode

This mode relies on the same principles as the NCM imaging, but the cantilever is now driven at a frequency just below the resonance frequency. The amplitude of the vibration will increase when bringing the tip closer to the sample, up to the point when during part of the cycle the tip touches the sample. This induces a decrease of the vibration amplitude, which is used to control the tip-sample distance and to generate topography.

All the mode has advantages and disadvantages over others. Generally for hard and stiff surface, contact mode is preferred whereas for soft samples like biological samples, non-contact or semi-contact mode is chosen. Semi contact mode is rather preferred over other modes due to its ability of giving high resolution without arte effect. Apart from topography, AFM can be used to scan adhesion forces, friction force, phase imaging which gives

compositional contrast, force modulation to scan elastic properties, magnetic force microscopy to scan magnetic domains, force distance spectroscopy, dynamic force microscopy, thermo conductivity, electrostatic force imaging and shear force imaging [57, 58].

For present thesis, NT-MDT make solver P47H SPM system has been used to carry out surface morphological measurements in contact and semi-contact mode of operation.

2.2.2. Atomic Force Acoustic Microscopy (AFAM)

Various developed SPM techniques allow measuring different local physical properties of the surface investigated. One of the key properties of interest is local elasticity or local indentation modulus. Several SPM modes such as phase imaging, force modulation imaging, and some other dynamic force imaging techniques can characterize elastic properties of sample qualitatively. However, force modulation technique can also give quantitative estimation of elastic properties but with poor sensitivity. The research works were still demanding for a scanning based technique that could give quantitative elastic properties [59-62] with high sensitivity and accuracy. AFAM developed by group of Prof. W. Arnold [60] can give qualitative as well as quantitative elastic properties of the test surfaces.

This method is based on measuring of variations of cantilever dynamic properties such as resonance frequency, amplitude and Q-factor caused by variation of the contact stiffness between tip and sample surface. The cantilever is operated in contact mode with constant deflection while the sample is set in to vibration by ultrasonic transducer on the frequency of cantilever flexural resonance. If cantilever properties such as dimension, spring constant and fundamental resonance frequency are known, contact stiffness of tip-sample can be derived from contact resonance spectra using characteristic equations described for clamped-spring-cantilever [60, 63]. Using Hertzian contact theory [64] for tip-sample contact, indentation

modulus of sample can be determined provided contact stiffness measurements have also been performed on a reference sample of known indentation modulus.

Generally, single reference method for determining gives Young's modulus value having error more than 20%. Major source of error are uncertainty in tip dimensions and indentation modulus. Using dual reference method such errors can be eliminated [65]. Apart from quantitative evaluation of elastic properties, AFAM can also be used to scan elastic properties nano metrically in terms of phase difference of cantilever vibrations. Contact resonance frequency can be scanned by AFAM and using suitable references, indentation modulus image can be generated nano metrically. Fig. 2.8 (a) and (b) show the topography and AFAM phase contrast image of Fe_2O_3-SiO_2 composite thin film deposited by co-evaporation. AFAM phase imaging gives a high contrast image depicting grains clearly whereas

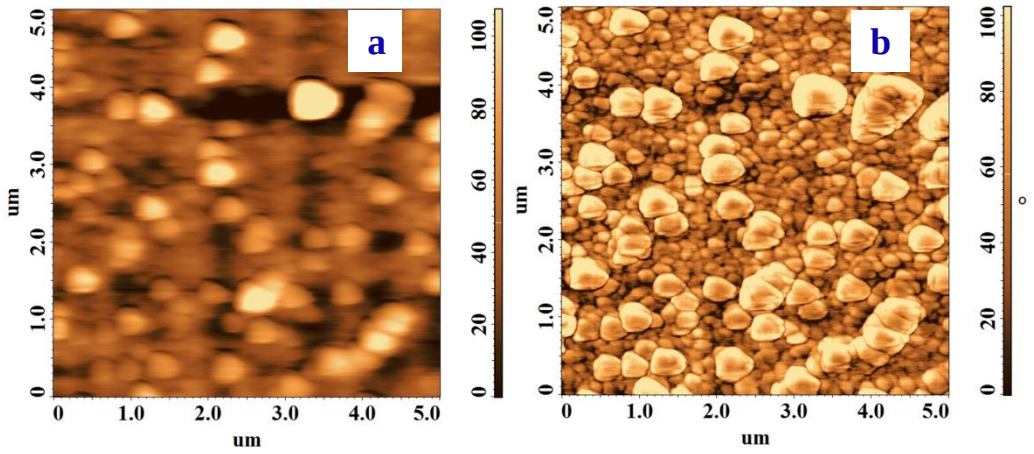

Fig. 2.8: (a). *AFM topography in contact mode (b) AFAM phase contrast image of Fe_2O_3-SiO_2 co-deposited thin film.*

AFM height image does not reveal grain boundary clearly. Therefore, AFAM images are not only used for scanning elastic properties but for high contrast morphological images also. For the characterization of elastic properties, NT-MDT make AFAM system equipped with a piezo-electric transducer has been used. Detailed description of measurement has been given in chapter 3.

2.2.3. Field Emission Scanning Electron Microscopy (FESEM)

Nano science and technology has been driving the development of recent electron microscopy demanding not only improved resolution of features but also for more information from the sample [66]. FESEM images a sample surface by raster scanning over it using high energy beam of electrons as probe. FESEM is a powerful imaging technique with a spatial resolution of 1 nm. It is an ideal tool for imaging morphology and to measure the thickness of thin film.

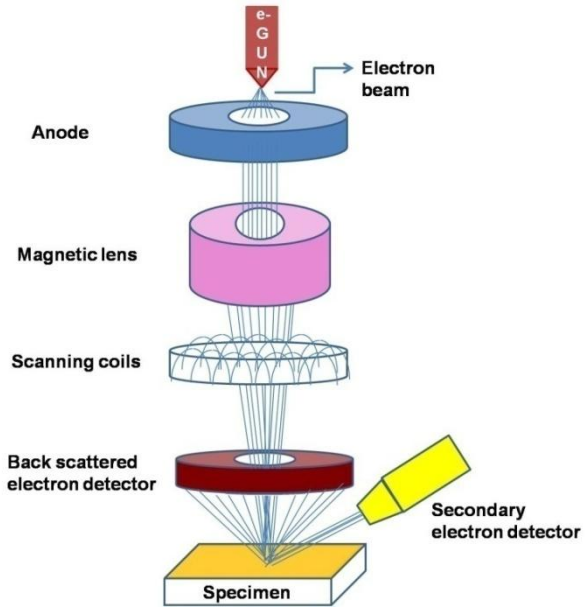

Fig.2.9: *Schematic of Field Emission Scanning Electron Microscopy.*

In FESEM, Field emission electrons are liberated from a sharp tip of the filament by applying very high voltages. These emitted electrons get focused by electromagnetic condenser lens to form a sharp electron beam with a narrow energy spread. A schematic representation of FESEM is illustrated in Fig. 2.9. The focused electron beam is used to raster scan over the material surface to get the morphology. The possible emission characteristics upon interaction of incident electron beam with matter are shown in Fig. 2.10. Generated

secondary and back scattered electrons are analyzed by respective detectors to obtain morphology.

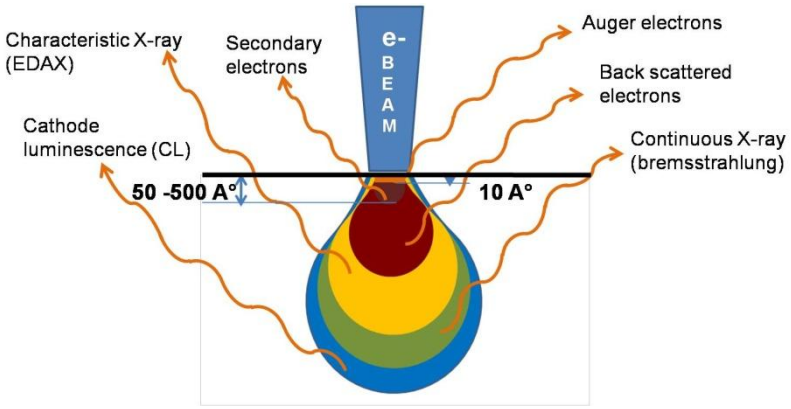

Figure 2.10: *Probable emissions during electron beam interaction with material surface.*

In addition to morphology, the back scattered electrons also gives atomic number (Z) contrast which is useful for mapping of different phases embedded in the surface. Thickness measurement of thin coatings and films, correlation of surface appearance and surface morphology, characterization of size, size distribution, shape and dispersion of additives, particulates and fibres in composites and blends, measurement of height and lateral dimensions of nano-meter sized objects, characterization of cell size and size distribution in foam materials, elemental analysis of micron-sized features, fracture and failure analysis, and defect analysis are main applications of FESEM in nano technology and material science.

In the present dissertation, FESEM (supra 55, Carlzeiss, Germany) has been used to measure cross-sectional morphology and thickness of the films. Energy of the electron beam was maintained at 5 keV while taking cross-sectional FESEM imaging of oxide thin films used in the present thesis.

2.2.4. Extended X-ray Absorption Fine Structure (EXAFS) Spectroscopy

X-ray absorption spectroscopy (XAS), which deals with the measurement of the X-ray absorption spectrum of a sample from 50 eV below to 1000 eV above the absorption edge

(K-, L- or M-edges) of a particular elemental species present in a material, comprises two complementary techniques, viz. X-ray absorption near-edge structure (XANES) and extended X-ray absorption fine structure (EXAFS). The former throughs light on the oxidation state of that particular element whereas the latter provides relevant information regarding the bond lengths and the coordination numbers of the neighboring shells around the elemental species in the material as well as regarding the disorder (both thermal and structural) present in the system. This technique has added advantage of being element-specific and crystallinity of sample is not a prerequisite. With X-rays being fairly penetrating in matter, this technique is not inherently surface-sensitive and average bulk information from a sample can be obtained. With the advent of modern bright synchrotron radiation sources, this technique has emerged to be one of the most powerful techniques for local structure determination, which can be applied to any type of material, viz. amorphous, polycrystalline, polymers, surfaces and solutions under different ambient and extreme environmental conditions [67-69]. XAS beam lines are some of the most significant and extensively used experimental facilities at synchrotron radiation sources all over the world.

In this technique, the energy of the X-ray photon is used to excite a core-electron of the sample atom and the atom is left in an excited state with an empty electron orbital (a core hole). The excited electron is called photo-electron and the kinetic energy of this electron 'E_{kin}' equals the difference of the energy from the incident X-ray photon '$\hbar\omega$' and the binding energy of the electron E_i ($E_{kin} = \hbar\omega - E_i$). The probability that an X-ray photon is absorbed by the radiated material is given by the absorption coefficient μ and it can be observed that μ increases strongly when the x-ray energies equal the binding energies 'E_i' of a core-electron of an element in the investigated material (Fig. 2.11). These step-like features in an absorption spectrum are called absorption edges. X-ray absorption spectra measured show oscillations just above the absorption edge as shown in Fig. 2.12 for copper foil.

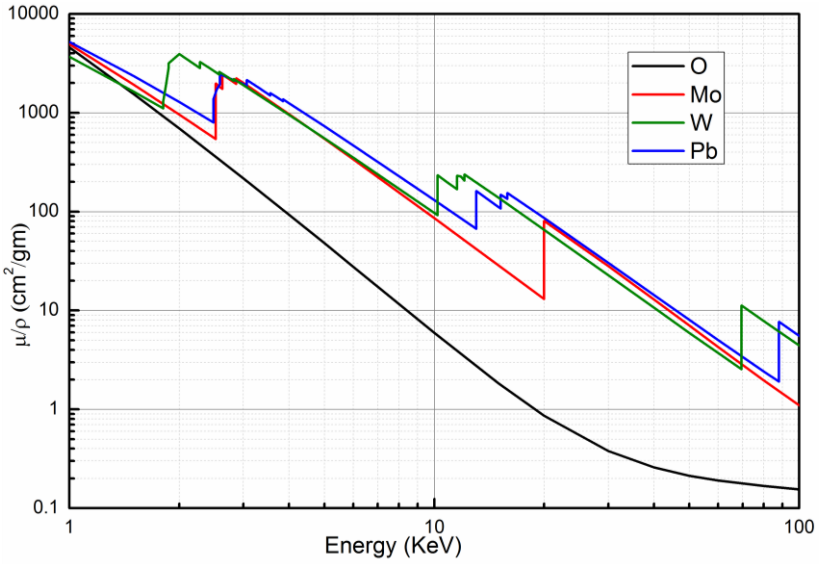

Fig.2.11: *Absorption spectra of several elements. The energies of the absorption edges correspond to the binding energies of the core-electrons of the element that are excited.*

These oscillations are called X-ray absorption fine structure and result from the fact that in condensed matter all atoms are embedded in a defined structure with neighbouring atoms at specified distances. The absorption spectra contain information about the structure of the material under investigation. The information obtained depends on the X-ray energy with

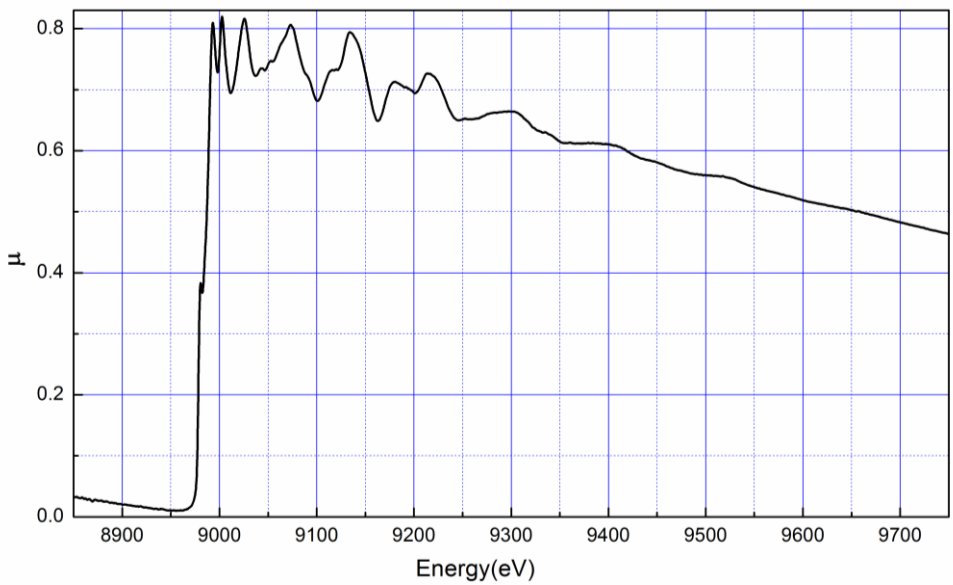

Fig. 2.12: *Absorption spectra of Copper foil measured at the copper K-edge. The EXAFS region begins approximately 50 eV above the absorption edge.*

respect to the binding energy of the electron 'E_i' and thus the spectrum can be divided into two parts: the X-ray absorption near edge structure (XANES) and the extended X-ray absorption fine structure (EXAFS).The near edge structure extends up to 50 eV above the absorption edge. In this energy region the core electron is excited to an unoccupied bound state, so that the shape of the absorption edge depends on the density of states closely above the Fermi level. Therefore, the oxidation state and binding geometry influence the XANES part of the spectrum. The region from 50 eV-1000 eV above an absorption edge is called EXAFS. This part of the spectrum contains information on the types and number of neighbor atoms to the absorbing atom.

EXAFS measurements in present thesis were carried out at the energy scanning EXAFS beamline (BL-09) in the fluorescence mode at the INDUS-2 Synchrotron Source (2.5 GeV, 120 mA) at the Raja Ramanna Centre for Advanced Technology (RRCAT), Indore, India[70]. Detailed procedure of measurement and data analysis is given in chapter 3 of the present thesis.

2.2.5. Optical Characterization

Optical characterization of thin films in the present thesis has been carried out using following two optical interference techniques

2.2.5.1. Spectrophotometry

Optical constants of substrate and thin film and film thickness have been determined from spectrophotometric measurements. A dual beam spectrophotometer was used to measure the transmission spectra of test samples. A working schematic of Shimadzu make dual beam spectrophotometer is shown in Fig. 2.13. Here the collimated light is made monochromatic using two sets of gratings. Then light is modulated using a mechanical chopper followed by splitting in two equal parts using a beam splitter. For transmission measurement, a baseline correction is done keeping both the beams unobstacled and scanning wavelengths by rotating

gratings. Transmitted radiation is recorded by photo multiplier tubes and lead sulphide (PbS) detectors. This is done to measure absolute transmission. Now, test sample is placed in the path of one beam, generally designated as sample beam. Other one is designated as reference beam. Again, wavelengths are scanned in desired wavelength region and transmitted radiation is recorded using the detectors. Transmission *(T)* of a sample of thickness d is given by Beer-Lambert-Bouguer law as following equation.

$$T = \frac{I}{I_0} = e^{-\alpha d} \tag{2.2}$$

Here I and I_0 are transmitted and incident intensity of light. *'α'* is absorption coefficient. For thin film samples, modulations in transmission spectra occur due to interference between the beam coming from different interfaces [71].

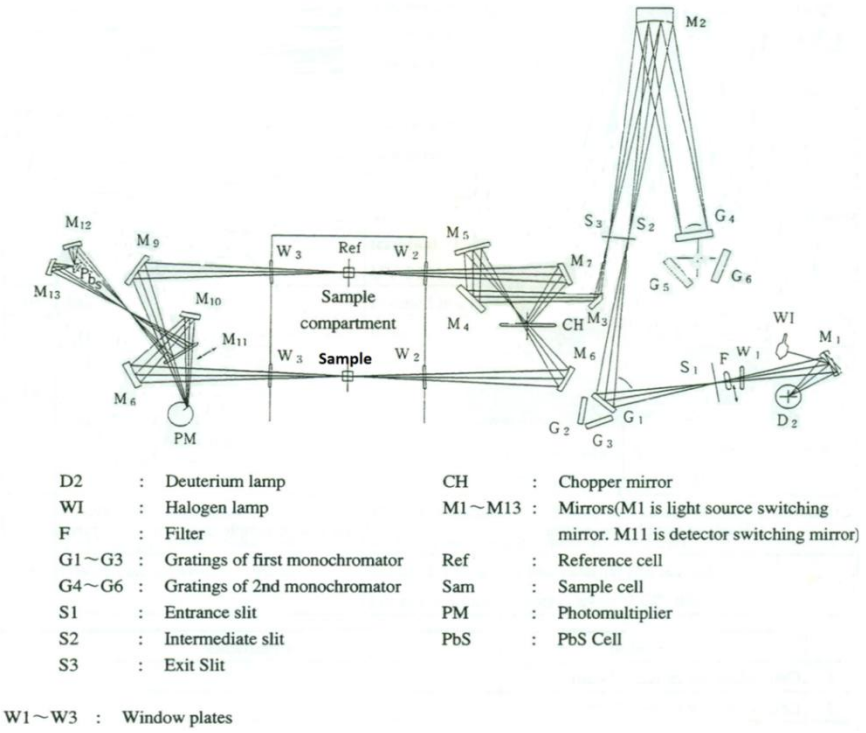

Fig. 2.13: *Schematic diagram of dual beam spectrophotometer (Shimadzu, UV3101PC).*

In present thesis, optical constants of the films have been obtained by fitting the measured transmission data with a theoretically generated spectrum under the following assumptions[72]:

[1] A thin isotropic dielectric layer covers a thick, non-absorbing or weakly substrate, and the optical system is immersed in air.

[2] Light of mean wavelength λ and spectral half width Δλ is incident normally on the sample.

[3] Interference of internally reflected light occurs in the thin films [$\Delta\lambda << \lambda^2/2nt$] and is negligible in the substrate [$\Delta\lambda << \lambda^2/2nt_s$] where n, t, t_s are the refractive index, thickness of the film, thickness of the substrate respectively.

[4] The film and the substrate are weakly absorbing in the studied spectral region i.e. $n^2 >> k^2$ and $n_s^2 >> k_s^2$, where k and k_s are the extinction coefficients of the film and the substrate.

With the above assumption film thickness uniformity is also assumed to get interference spectra. Transmittance of such a system can be expressed as follows [7]:

$$T(\lambda; n, t, n_s, k_s) = A(\lambda; n, k, t, n_s, k_s) / B(\lambda; n, k, t, n_s, k_s) \qquad (2.3)$$

Using above mentioned relation and assuming a suitable dispersion model for the wavelength variation of the optical constants of the substrate and the film, the fitting has been carried out by minimizing the mean square error (MSE) using Levenberg-Marquardt algorithm:

$$\sum_i [T_{\exp(\lambda i)} - T_{Th(\lambda, n_s, k_s, t, n, k)}]^2 \qquad (2.4)$$

Where, T_{exp} and T_{th} are the experimental and theoretical transmittance spectra and λ_i is scanning wavelength in nm. Such optimization technique gives optical constants as well as thickness of the thin films.

After selecting the appropriate dispersion model and optimization method, the experimental transmission spectrum is fitted. From fitting parameters, optical constants and film thickness are derived.

2.2.5.2. Spectroscopic ellipsometry

Ellipsometry is a non destructive optical technique and it uses the fact that light undergoes some change in polarization when it is reflected off the surface of a material. Infect, polarimetry is more suitable name for this. Generally linearly polarised light becomes elliptical polarised after reflection from a surface and hence this technique is called ellipsometry. The polarization change is the characteristic of the surface structure of the sample and hence various information about the material such as refractive index, extinction coefficient, surface roughness and porosity etc., can be obtained by analyzing the reflected light beam. Ellipsometry is a highly useful technique to determine optical constants, thickness, and roughness, fraction of voids and index homogeneity of transparent and semi-transparent thin films.

In Ellipsometry, the variation of the amplitude and the phase difference between the parallel (p) and perpendicular (s) components of the reflected light polarized with respect to the plane of incidence are measured. In general, reflection causes a change in the relative phase of p and s waves and in the ratio of their amplitudes. Change polarization state is measured by the two quantities viz. Ψ (measures amplitude ratio) and Δ (measure relative phase change). These are given by [73]:

$$\rho = \frac{r_p}{r_s} = \tan\psi \exp(i\Delta) \tag{2.5}$$

where r_p and r_s are the reflection coefficients for the p and s component of the waves respectively.

There are three basic designs of ellipsometer in general use but all three do the same work. Sample is illuminated with a narrow, parallel beam of monochromatic light of known polarisation at a known angle of incidence. Using a polarisation-sensitive analyser, change in polarisation state of light in terms of ellipsometric angles, Ψ and Δ are measured after

reflection from the sample surface. From this polarization change, optical parameters for the sample are calculated through the suitable modeling of measured data. The differences between the various instruments are due to the choice of polarizer and analysers, and light source.

Fig. 2.14: *SEMILAB GESS-E spectroscopic ellipsometer used for optical characterization.*

A rotating polarizer type spectroscopic ellipsometer (SEMILAB make) has been used for optical characterization of thin films in present dissertation. Detailed procedure of ellipsometric data analysis for thin films has been given in subsequent chapters.

2.2.6. Grazing Incidence X-ray Reflectivity (GIXR) Characterization

The basic theory of X-ray reflectivity is derived from classical optics and Fresnel theory, modified slightly for X-ray. The complex refractive index (n) of an element in the X-ray region is given by[74] :

$$\eta = 1 - \delta - i\beta \tag{2.6}$$

where, $\delta = \frac{\lambda^2}{2\pi} Z r_e \rho_e$ and $\beta = \frac{\mu\lambda}{4\pi}$ (2.7)

Here δ is a function of wavelength (λ), electron density (ρ_e) and atomic number Z; given by the above expression (8) [r_e is classical electron radius]. Parameter β is the function μ which is the linear absorption coefficient of the material at the particular wavelength λ. Since refractive index of all material in hard X-ray region is less than 1, X-rays suffers total external reflection at extreme grazing angle of incidence from any surface. However, as the grazing angle of incidence value (θ) exceeds the critical angle (θ_c), X-ray starts penetrating inside the layer and reflectivity falls rapidly with angle θ. The critical angle is approximated by:

$$\theta_c = \sqrt{(2\delta)} \qquad (2.8)$$

The reflectivity of X-ray from a thin film i.e., of a plane boundary between two media can be obtained using the well-known Fresnel's boundary conditions of continuity of the tangential components of the electric field vector and its derivative at the sharp interface[74]. However, the Fresnel's reflectivity gets modified for a rough surface by a 'Debye-Waller -like' factor as follows:

$$R_O = R_p \exp(-q^2\sigma^2/2) \qquad (2.9)$$

where, q is the momentum transfer ($4\pi Sin\theta/\lambda$), R_o is the reflectivity of the rough surface and R_p is the Fresnel reflectivity of an otherwise identical smooth surface, σ being the RMS roughness of the surface. Thus by fitting the X-ray reflectivity spectrum of the surface of a sample near its critical angle, estimation of mass density (ρ) and RMS surface roughness (σ), film thickness, can be made quite accurately [75, 76]. The grazing incidence X-ray reflectivity measurements of thin films in present thesis were carried out on automated GIXR reflectometer systems using the Cu Kα radiation (1.54Å).

2.2.7. Grazing Incidence X-ray Diffraction (GIXRD) Measurements

GIXRD is a surface sensitive technique to probe crystalline structure at small angles of incidences of incoming X-ray on test sample. In this technique, collimated X-ray beam is allowed to incident on sample near critical angle. At critical angle, penetration of X-ray beam inside sample is limited to small distances (up to 10 nm) due to total external reflection at surface (refractive index for X-ray is less than 1). At grazing incidence, beam covers a large surface area of the sample leading to large structural contribution from test sample in form of thin film, surface or interface. Simultaneously, substrate structure does not interfere sample diffraction pattern due to negligible penetration of X-ray in substrate (only in thin films having thickness less than 10 nm, small substrate contribution comes due to the generation of evanescent wave at interface). In Fig. 2.15, a schematic of GIXRD set-up is shown.

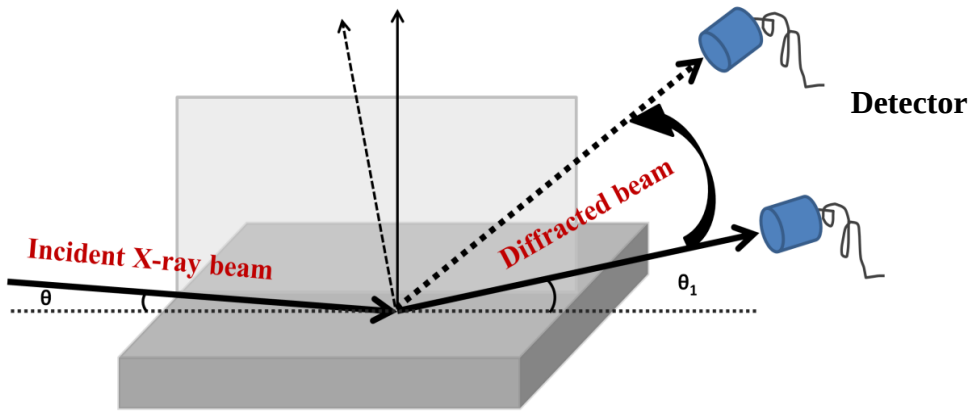

Fig. 2.15: *Schematic diagrams of GIXRD geometry.*

For present thesis, Crystal structure of films was examined by recording GIXRD pattern by Rikaku Ultima-IV XRD machine using Cu Kα X-ray radiation (λ=1.5402 Å). GIXRD spectra were recorded in 2θ geometry.

CHAPTER 3: OBLIQUE ANGLE DEPOSITION OF HfO_2 THIN FILMS BY EB EVAPORATION

In this chapter, HfO_2 thin films have been deposited on fused silica and Si substrate by EB evaporation at several oblique angles of deposition. Various properties of such films such as elastic, optical, micro-structural and morphological properties of such films have been investigated extensively by employing various characterization technique and theoretical models. This chapter has been described in two parts. In the first part of this chapter, effect of deposition angle on elastic, micro structural and local structure properties of obliquely deposited HfO_2 thin films has investigated. In second part, optical and morphological properties have been explored.

3.1. Study of Elastic, Micro structural and Local Structure properties

3.1.1. Introduction

Oblique angle deposition of thin films has been attracting researchers due to its applications in the fabrication of interference devices, micro sensors, microelectronics, photonic crystals, and rugate structures based devices. Presently, it is being used for fabricating precision interference filters [10] in which refractive index is varied by varying the angle of deposition resulting in varying porosity due to atomic shadowing and limited ad-atom diffusion [2, 20, 77] during growth. It generally works at angles greater than 60° with normal to the substrate. When the angle reaches around 80°, it is termed as glancing angle deposition (GLAD).

Oblique angle deposition results in realization of special nano and microstructures of thin films. By employing substrate rotation and varying angle of deposition, different geometries like pillar, helix, zigzag, erect columns etc., have been achieved [5-7]. Zhu *et al.* have fabricated multi-stop band interference rugate filter exploiting GLAD technique [9]. Park *et al*. have fabricated bilayer circular filter by GLAD deposition of TiO_2 thin films [78] and Fahr *et al.* have developed optical rugate filters for light trapping in solar cells[8]. Gasda *et al*. have fabricated nano-rod proton exchange membrane fuel cell cathodes by glancing angle deposition of carbon [79]. Researchers have also developed GLAD magnetic data storage device [80], antireflection coating [37], selective polarization transmission filter [81], narrow band pass rugate filter [30], and relative humidity sensors [82] by employing oblique angle deposition.

Elastic properties are important and indispensable parameters in the assessment of environment & mechanical stability [83] of thin films. They differ significantly from those of the bulk materials due to the interfaces, microstructure, and the underlying substrates. Similar to optical and structural properties, elastic properties such as the stress, co-efficient of thermal expansion, poison's ratio and indentation modulus of the film are also affected by the micro or nano-structure dictated by the deposition process parameters and the deposition technique [84].Thin films deposited at oblique angles are highly porous due to engineered microstructure and hence their mechanical stability is a subject of concern. Therefore it is of great importance to characterize and optimize elastic properties of these porous thin films. Many techniques are being used for the determination of elastic properties of thin films, including micro-and nano-indentation tests [85], laser induced surface acoustic wave (SAW) [86], Surface Brillion light scattering measurements [87] and Atomic Force Acoustic Microscopy (AFAM) [88]. The nano indentation techniques have limitations due to speed, limited lateral resolution and substrate effect [89]. It is also inherently destructive technique.

Laser induced SAW method needs rigorous analysis and also has limitations in terms of low sensitivity and limited spectrum band width [90]. Surface Brillouin light Scattering is time consuming and sensitive to the environmental noise [91]. AFAM technique, on the other hand, can give both quantitative values of Young's modulus of thin films like other technique as well as qualitative picture of Young's modulus in terms of acoustic image, simultaneously with surface topography of the film without being affected by the elastic properties of the substrate [92]. This makes AFAM, a unique and attractive technique for the investigation of elastic properties of thin films.

AFAM technique is based on the evaluation of contact stiffness between tip and sample [93]. Contact resonance frequency for I, II and if possible III overtones are compared to free resonance frequency of the cantilever probe. From the shift of contact resonance frequencies from free vibrations, the contact stiffness (tip-sample) is computed by solving tip-sample vibration characteristic equation [59, 60, 84, 93]. Same measurement is carried out on reference material with known indentation modulus. By employing Hertzian contact formulation and indentation modulus of reference material, indentation modulus of test sample is computed. In AFAM measurement technique, tip geometry plays an important role in determining the indentation modulus. To quantify indentation modulus of the sample**,** quantitative elastic properties and geometry of cantilever tip are required. Direct measurement of elastic properties of probe is a difficult & erroneous process and researchers assume bulk values for the probe. Estimation of indentation modulus with such assumptions (and single reference material) leads to uncertainty more than 20% [94, 95]. Rabe *et al*. [96, 97], proposed dual reference method to determine indentation modulus of unknown sample. This method does not rely on tip geometry & tip elastic properties and can offer results with uncertainty as low as 1%, depending on selection of references.

In the present study, we have employed dual reference method to estimate indentation modulus of obliquely deposited HfO_2 thin films electron beam evaporation.

Hafnium oxide is a widely used optical material which possesses high refractive index and high laser induced damage threshold [98-101]**.** Its wide band gap (~5.5-5.7eV) [98, 102] gives its transparency over a wide spectral range, extending from the ultraviolet to the mid-infrared [103]**.** We have also performed grazing incidence X-ray reflectivity (GIXR) measurements to determine the film density and RMS surface roughness. Cross-sectional morphology of such films has also been measured by field emission scanning electron microscopy (FESEM) to explore the microstructure and thickness of the films. Extended X-ray absorption fine structure (EXAFS) spectroscopy measurements have also been performed on such films to reveal phases, bond length and oxidation states. A correlation among indentation modulus, film density and microstructure of films deposited at different angles has been set.

3.1.2. Experimental Detail

3.1.2.1. Oblique angle deposition of HfO_2 thin film

In present wok, five HfO_2 thin films have been deposited on silicon (100) substrate at 200°C by reactive electron beam evaporation technique in a VTD make 'Vera-902" EB evaporation coating system. Before deposition entire batch of Si substrates were cleaned ultrasonically to achieve good quality films. Such films were deposited at angles (α) = 0, 40, 57, 68 and 80 degrees designated as SAMP-5, SAMP-4, SAMP-3, SAMP-2 and SAMP-1 respectively. The angle of deposition (α) is defined as the angle between normal to the substrate plane and incident vapour flux. Different values of angle were set by tilting the substrate whereas direction of the incoming vapour flux was held fix. Typical distance between substrate and EB evaporated vapour source was kept ~ 45 cm. Schematic diagram and actual photograph of the oblique angle deposition system is shown in Fig. 2.2. The base pressure prior to

deposition was kept $1x10^{-5}$ mbar and during deposition, high purity (99.9%) oxygen was supplied to deposition chamber through mass flow controller to maintain the stoichiometry of HfO_2 thin films. An optimized oxygen partial pressure was kept at $1x10^{-4}$ mbar. Rate of deposition and film thicknesses were monitored and controlled by Inficon make 'XTC2' quartz crystal controller/monitor. Deposition rate was maintained at 5Å/s.

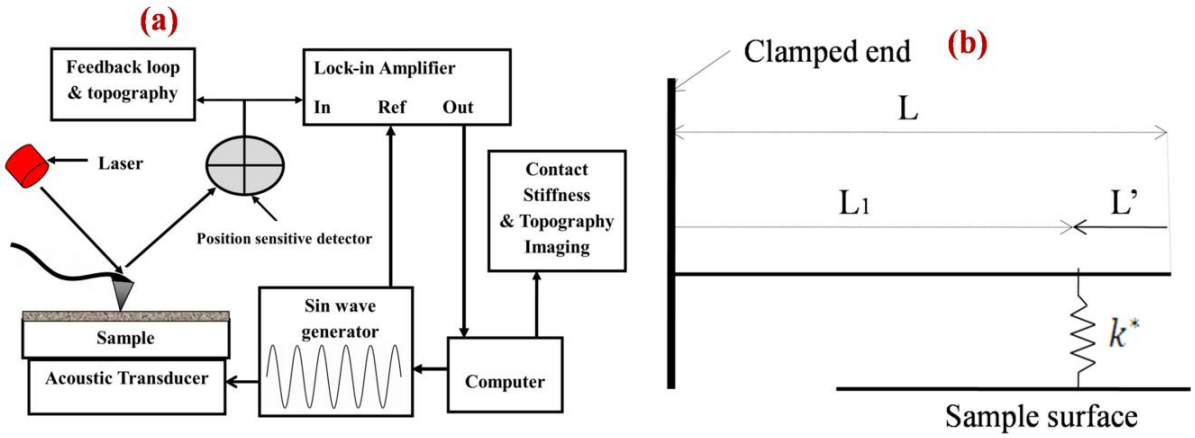

Fig. 3.1 *(a): Schematic of AFAM set-up. (b): Simplified cantilever tip-sample contact interaction.*

3.1.2.2. AFAM Characterization: measurement of contact resonance frequencies

In contact resonance measurements, the sample under investigation was bonded to a piezoelectric transducer placed on the AFM stage just below the sample. Piezo-transducer generates acoustic waves in the range 0.1-5.0 MHz. Honey has a very good acoustic conductance and was used to fix measuring samples on ultrasonic transducer. There are many ultrasonic couplers available but honey is one of the cheapest and easily available. It may be noted that, surface of silicon substrate other than coating side was unpolished and hence rough. High viscosity of honey makes it an appropriate coupler on rougher surfaces to fill the air gap between silicon substrate and acoustic transducer. For coupling of sample to transducer, a small drop of honey is put on ultrasonic transducer surface and honey is spread evenly on the part of the transducer surface that is to contact the sample. Then thin film sample was put on the transducer and sample was slightly pressed with tweezers make

several short movement along the transducer surface to ensure optimal spread of honey and better contact between surfaces. The ultrasonic transducer was excited with a continuous sine wave generator from 0.1 to 5 MHz frequency and 0-1 V signal. Schematic of AFAM set-up utilized for our experiments is shown in Fig. 3.1 (a). The cantilever probe was brought to sample contact in repulsive mode and I^{st} & II^{nd} contact resonance frequencies were measured at many different points on HfO_2 thin film. Mean contact resonance frequency was used for further calculations. Contact resonance frequencies measurement was also performed on reference samples viz., BK7 glass, Silicon (100) and Sapphire, whose indentation modulii are known. Two references together were used to eliminate the requirement of geometry and indentation modulus of the measuring cantilever probe used for computation of indentation modulus of thin films in the present experiment. Contact resonance measurement was carried out using NT-MDT, Russia-make P47H system and diamond like carbon (DLC) coated tip on Si cantilever has been used for the entire experiment. DLC coated tip was chosen because of its long durability, high hardness and high resistance to the changes in geometry because of measurements. In AFAM, a laser beam deflection feedback mechanism is employed which controls the force between the tip and sample.

3.1.2.3. GIXR and FESEM measurements

Density of the films has been estimated from GIXR measurements carried out on an X-ray reflectometer. Detailed theory of X-ray reflectivity is described in ref. [74]. The measurements have been carried out using Cu K_α (1.54Å) source at grazing angle of incidence in the range of 0-0.5° with angular resolution of 0.01°. Principle of GIXR measurements is discussed in section 2.2.6 of chapter 2. Cross-sectional morphology of the samples was recorded by FESEM system.

3.1.2.4. EXAFS measurements

Theoretical background of EXAFS is already discussed in Chapter 2 of the thesis. In the present study, EXAFS measurements were performed on obliquely deposited HfO_2 thin films to probe the local structure surrounding. The EXAFS measurements have been carried out at the Energy-Scanning EXAFS beam line (BL-9) at the INDUS-2 Synchrotron Source (2.5 GeV, 100 mA) at Raja Ramanna Centre for Advanced Technology (RRCAT), Indore, India [70, 104]. This beamline operates in energy range of 4 KeV to 25 KeV. The beamline optics consist of an Rh/Pt coated collimating meridional cylindrical mirror and the collimated beam reflected by the mirror is monochromatized by a Si (111) (crystal spacing = 6.2709) based double crystal monochromator (DCM). The second crystal of DCM is a sagittal cylinder used for horizontal focusing while an Rh/Pt coated bendable post mirror facing down is used for vertical focusing of the beam at the sample position. Rejection of the higher harmonics content in the X-ray beam is performed by detuning the second crystal of DCM. In the present case, EXAFS measurements at Hf L3-edge have been performed in fluorescence mode. In fluorescence mode, sample is placed at 45^o to the incident X-ray beam and the fluorescence signal (I_f) is detected using a Si drift detector placed at 90^o to the incident X-ray beam. An ionization chamber is used prior to the sample to measure the incident X ray flux (I_0) and the absorbance of the sample ($\mu = \frac{I_f}{I_0}$) is obtained as a function of energy by scanning the monochromator over the specified energy range.

3.1.3. Computation of Indentation Modulus

AFAM technique and detailed methodology of contact resonance frequency measurement have been discussed extensively in references [95, 96]. In order to relate the measured contact resonance frequency quantitatively to the sample elastic properties, cantilever can be modelled as rectangular uniform beam. Contact stiffness k^* is evaluated from contact

resonance frequency using the characteristic equation for test sample-cantilever coupled vibrations. The derivation of characteristic equation from equation of motion of flexural vibrations as well as torsional vibrations of cantilever tip has been discussed in references [60, 94]. Elastic, adhesion and friction forces always play significant roles when cantilever tip comes in contact with sample surface. Such forces are nonlinear function of distance between the tip and the sample surface. Analytical solution of such equation of motion is a rather cumbersome task. But by assuming linear response for small vibration amplitude, tip-sample interaction can be approximated by vertical & lateral spring dashpot system [96]. The total length of cantilever can be defined as $L = L_1 + L'$. L_1 is the actual position of the tip from cantilever base. It is well known that [94, 105, 106] normal contact stiffness k^* depends much more on the sensor tip position L_1 than on any other parameters such as tip-surface angle differing from normal, lateral contact stiffness, lateral damping constant & air damping. In general, by neglecting tip mass and above mentioned parameters, tip-sample coupled system reduces to a simple system as shown in Fig. 3.1(b). In the simplest model, only vertical contact stiffness k^* representing the interaction force describes the vibrations of the surface coupled cantilever. A static normal load, significantly greater than the adhesion force, is applied on the cantilever in order to neglect the effect of adhesion forces on tip-sample interaction. This way, the elastic force becomes dominating in tip-sample interaction. The characteristic equation for normal contact stiffness for the simplified system is given by [63, 96]:

$$k^* = \frac{\left(\frac{2}{3}\right) k_c (k_n L r)^3 (1 + \cos k_n L \cosh k_n L)}{\left[\begin{array}{l} \left\{\left(\sinh k_n L r \cos k_n L r - \cosh k_n L r \sin k_n L r\right)\left(1 + \cos k_n L(1-r)\cosh k_n L(1-r)\right)\right\} \\ + \left\{\begin{array}{l}\left(\cosh k_n L(1-r)\sin k_n L(1-r) - \sinh k_n L(1-r)\cos k_n L(1-r)\right) \\ \left(1 - \cos k_n L r \cosh k_n L r\right)\end{array}\right\} \end{array}\right]} \quad (3.1)$$

Where $r=L_1/L$, k_n is wave number of n^{th} eigenmode and k_c is the spring constant or stiffness of a rectangular cantilever. To determine the value of k^* from Eq. 3.1, values of k_c, k_nL and L_1 are required. Value of k_c can be determined from Sadar normal method [107] by using free cantilever resonance frequency spectra which are achieved by exciting cantilever using a piezo-frequency generator. The resonance frequencies f_n of the cantilever are related to wave number k_n and they are given by [96]:

$$k_nL = C_BL\sqrt{f_n} \tag{3.2}$$

Where $k_n = \frac{2\pi}{\lambda_n}$: λ_n is acoustic wavelength. C_B is the cantilever characteristic constant that depends on density, Modulus of elasticity (E) and geometry of cantilever. For free vibration condition of cantilever (when tip is far from sample surface), tip-sample contact stiffness (k^*) is zero and for this condition Eq. 3.1 reduces to

$$1+\cos k_nL\cosh k_nL = 0 \tag{3.3}$$

This is the characteristic equation for free flexural vibrations of cantilever. For different vibration mode (n), solutions of Eq. 3.3 are given by [84]:

$$k_1L = 1.8751, k_2L = 4.69, k_3L = 7.85..... \tag{3.4}$$

By putting the values of kL and resonance frequency f in Eq. 3.2, the value of C_BL can be obtained precisely without knowing the mechanical or elastic properties of cantilever. In order to determine the actual tip position and corresponding contact stiffness, we have used the following criteria

$$k^*(f_1, L_1/L) = k^*(f_2, L_1/L) \tag{3.5}$$

Here f_1 & f_2 are 1st and 2nd contact resonance frequencies. The solution of above equation is determined numerically by taking range of L_1/L from 0.85 to 0.98. For most of the cantilevers, the value L_1/L lies in this range. From Eq. 3.5, the value of L_1/L is evaluated and

by substituting the value L_1/L in Eq. 3.1, contact stiffness is determined. The main error in estimation of k^* is due to uncertainty in geometry of tip.

Finally, in order to determine indentation modulus, the contact between tip and sample surface is considered by Hertzian contact mechanism [64]. With Hertzian contact consideration between spherical tip and flat sample surface, normal contact stiffness for a given normal static load is given by

$$k^* = \sqrt[3]{6E^{*2}RF_N} \tag{3.6}$$

Where E^* is reduced Young's modulus of elasticity and E^* is related to the indentation modulus of tip and sample by following relation

$$\frac{1}{E^*} = \frac{1}{M_t} + \frac{1}{M_s} \tag{3.7}$$

Here M_t & M_s are indentation modulus of tip and sample respectively. Hertzian contact radius (nm) is given as following

$$a = \sqrt[3]{3F_N R / 4E^*} \tag{3.8}$$

From Eq. 3.6 and 3.8, following can be deduced

$$a = \frac{k^*}{2E^*} \tag{3.9}$$

To make elastic forces dominant, stiff cantilever is used and high static load F_N is applied. For indentation modulus measurements using AFAM, a reference material with known indentation modulus, usually an amorphous or a single-crystal material with known orientation, is used to derive the indentation modulus of the test sample using a relation which follows Eq. 3.6 [63]:

$$\frac{E_s^*}{E_r^*} = \left(\frac{k_s^*}{k_r^*}\right)^n \tag{3.10}$$

Where k_s & k_r are normal contact stiffness and E_s & E_r are reduced modulus of elasticity for test and reference samples respectively. Here n=3/2 for spherical tip in contact with flat surface and n=1 for flat tip in contact with flat sample. By combining Eq. 3.7 and 3.10, indentation modulus of sample can be expressed as:

$$\frac{1}{M_s} = \frac{1}{M_r}\left(\frac{k_r^*}{k_s^*}\right)^n + \frac{1}{M_t}\left[\left(\frac{k_r^*}{k_s^*}\right)^n - 1\right] \tag{3.11}$$

Here indentation modulus of probe tip is assumed as that of bulk material. Manufacturers usually do not measure indentation modulus of tip and only quote reported values. In our case it is even more ambiguous because it is a DLC coated tip. Such an assumption will lead to major uncertainties in the determination of indentation modulus of test sample and uncertainty can be ≥ 20%. Uncertainty in indentation modulus of tip could be reduced by using dual reference method discussed earlier. Indentation modulus of sample using two references can be written as following [65]:

$$M_s = \frac{\left(k^*_{r1} \big/ k^*_{r2}\right)^n - 1}{\left(k^*_{r1} \big/ k^*_{s}\right)^n \left[\frac{1}{M_{r2}} - \frac{1}{M_{r1}}\right] + \left(k^*_{r1} \big/ k^*_{r2}\right)^n \left[\frac{1}{M_{r1}} - \frac{1}{M_{r2}}\right]} \tag{3.12}$$

Here k^*_{r1}, M_{r1} and k^*_{r2}, M_{r2} are contact stiffness & indentation modulus of reference sample-1 and 2 respectively. Dual reference method is insensitive to tip geometry or is marginally affected by tip geometry [65]. Dual reference method permits the calculations of the indentation modulus of the tip and is given by following relation [65].

$$M_T = \frac{\left\{(k^*_{r1})^n - (k^*_{r2})^n\right\} M_{r1} M_{r2}}{(k^*_{r2})^n M_{r1} - (k^*_{r1})^n M_{r2}} \tag{3.13}$$

This way, by choosing two suitable references of known indentation modulus, the indentation modulus of tip can be determined with an uncertainty as low as 1%.

3.1.4. Results and Discussion

3.1.4.1. Elastic and micro-structural properties

Fundamental and first free resonance frequencies for used DLC coated cantilever probe are shown in Fig. 3.2 (a). For computing contact stiffness of test thin films, accurate value of spring constant (k_c) of the cantilever is required. Cantilever probe manufacturers do not quote exact value of k_c for individual probe but quote a range of possible values. In order to determine k_c accurately of used probe, fundamental free resonance spectra have been fitted using formulation proposed by Sadar, a methodology known as Sadar normal method. Fundamental free resonance frequency for the cantilever probe used is 193.8 kHz and computed k_c is 8.7 N/m. 1^{st} and 2^{nd} contact resonance frequency spectra have been measured for entire batch of thin films. To keep parity in normal contact resonance measurements, same normal static load of 1919 nN has been applied on cantilever tip for entire measurement. As mentioned in section 3.1.3, if adhesion forces between cantilever tip and test sample, while being in contact, are comparable to normal static load, Hertzian contact mechanism fails. Normal static load has been estimated from force-distance spectroscopy in AFM measurements. Force distance curves for sample SAMP-4 are shown in Fig. 3.4. Adhesion forces have been determined from pull-off region of force distance curves for all the samples. Magnitude of such forces is 24.5 nN for SAMP-4, and lies between 15 to 30 nN for entire batch of films. To eliminate the effect of such non-linear adhesive forces, a sufficiently high normal static load of 1919 nN has been applied on cantilever tip. In Fig. 3.2 (b), 1^{st} & 2^{nd} contact resonances have been plotted as a function of applied static load. Resonance curves follow a Lorentzian shape and both amplitude & frequency of contact resonances increase with static load. Such behavior of contact resonances with static load follows flexural vibration theory [60]. Contact stiffness determined using characteristic Eq. 3.1 for 1^{st} & 2^{nd} contact resonances have been computed numerically for L_1/L ranging from 0.85 to 0.98.The

actual tip position and contact stiffness have been determined by using Eq. 3.5, in which contact stiffness obtained from 1st and 2nd contact resonance

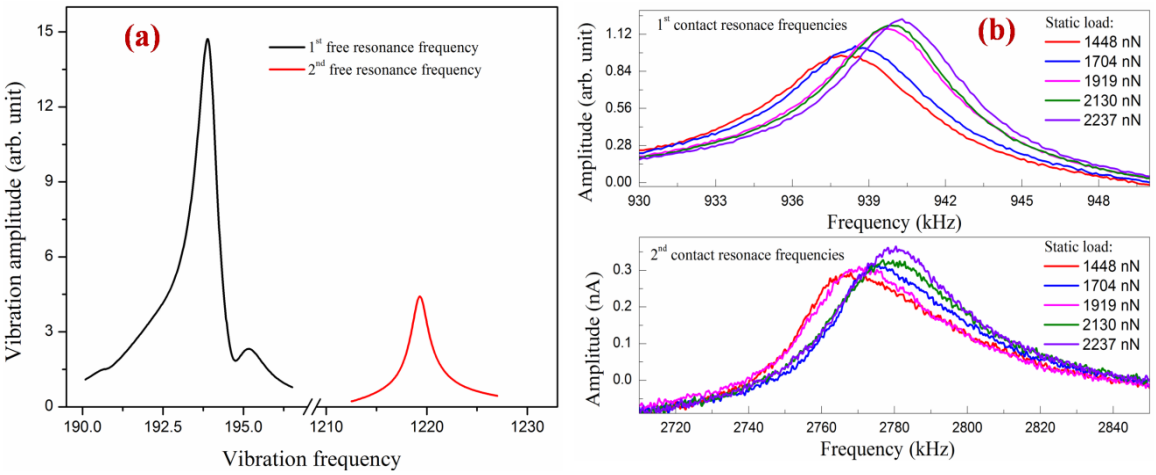

Fig. 3.2 *(a): Fundamental and 1st overtone of free resonance frequency of cantilever probe. (b). Plot of 1st and 2nd tip-sample contact resonance frequencies as a function applied static load for thin film SAMP-5.*

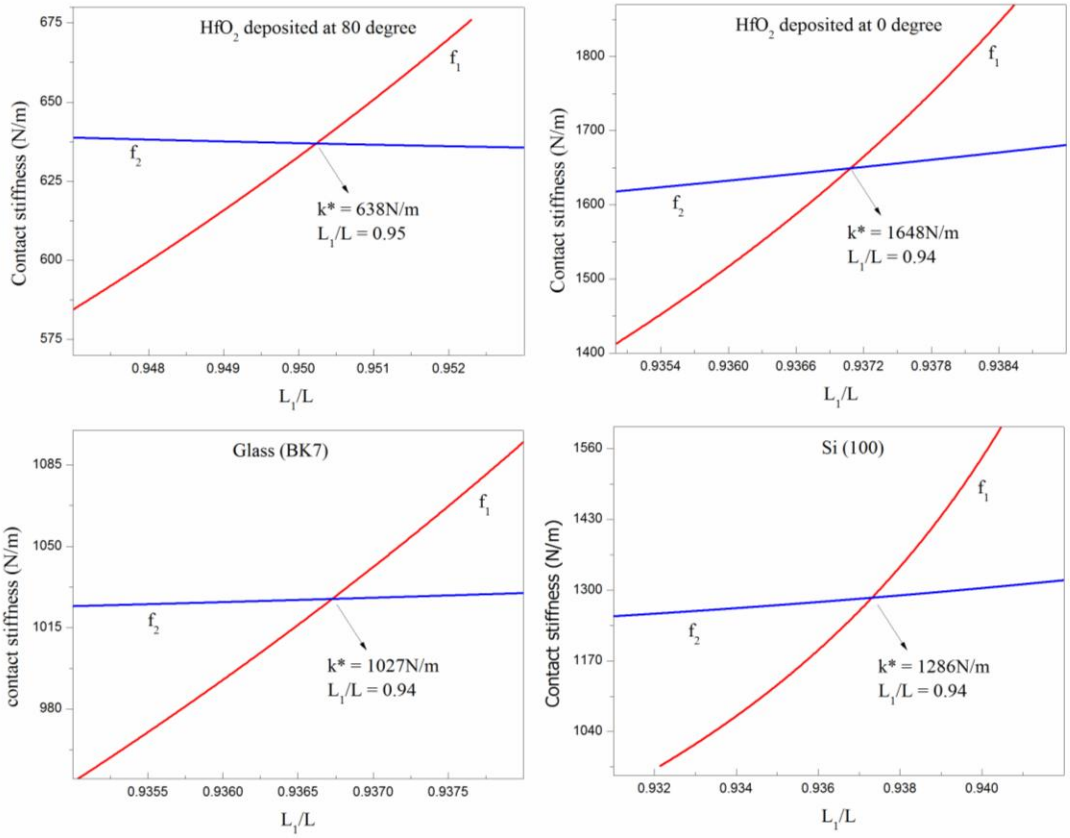

Fig. 3.3*: Plot of contact stiffness for 1st and 2nd contact resonance frequencies as a function of L_1/L for SAMP-1 & SAMP-5 and glass & Si (100) references.*

frequencies are equated. Computed contact stiffness values for Si (100), BK7 glass, Sapphire and obliquely deposited HfO_2 thin films are listed in Table 3.1 and Table 3.2 with corresponding L_1/L values. Actual tip position lies between (L_1/L) 0.94 to 0.95 and normal contact stiffness lies between 638 to 1648 N/m for these films. Ratio k^*/k_c varies from 73 to 189 which is close to 100 and the ratio in this range is considered as low.

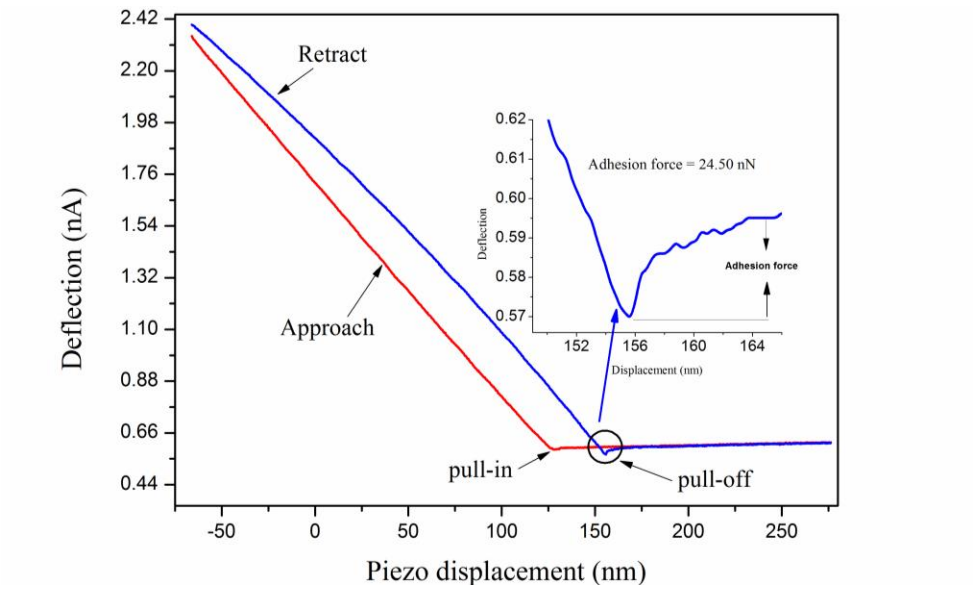

Fig. 3.4*: Plot of force-distance curves taken by AFM for SAMP-4. In inset pull-off curve is highlighted to determine tip-sample adhesion force.*

Table 3.1*: Contact resonance frequencies, contact stiffness and indentation modulus of references; Silicon (100), BK7 Glass and Sapphire.*

Name of sample	1st contact resonance frequency (kHz)	2nd contact resonance frequency (kHz)	Contact stiffness (N/m)	Ratio (L_1/L)	Indentation modulus (GPa)
Si (100)	935	2624	1286	0.94	135 ± 3
BK7 Glass	928	2473	1025	0.94	89 ± 2
Sapphire	945	2860	2113	0.94	420 ± 20

If ratio becomes of order of 1000 or exceeds 1000, it is considered as high. Consequently; k^*/k_c ratio being low as described in reference [97], the lateral forces between cantilever tip

and test sample are negligible and the influence of lateral contact stiffness on contact resonance frequencies is not significant which can be neglected. Contact stiffness plots for 1st and 2nd contact resonance frequencies as a function of effective tip position *(L_1/L)* for HfO_2 thin film SAMP-1, SAMP-5, BK7 glass and Si (100) are shown in Fig. 3.3. Intersection of two curves gives contact stiffness and actual tip position. Uncertainty in normal contact stiffness calculations is around 0.5%; mainly due to uncertainly in contact resonance

Table 3.2*: Contact resonance frequencies, contact stiffness and indentation modulus of HfO_2 thin films deposited at different angles.*

Sample name	1st Contact Resonance Frequency (kHz)	2nd Contact Resonance Frequency (kHz)	Contact Stiffness (N/m)	Ratio (L_1/L)	Indentation Modulus (GPa)
SAMP-1	877	2131	638	0.95	42 ± 7
SAMP-2	909	2573	1260	0.95	130 ± 3
SAMP-3	940	2670	1379	0.94	154 ± 4
SAMP-4	941	2715	1496	0.94	180 ± 6
SAMP-5	941	2760	1648	0.94	221 ± 8

Table 3.3: *Results of SEM, AFM and GIXR measurements*

Sample name	Film deposition angle (α) (degree)	Measured Column tilt angle (β) (degree)	Theoretical Column tilt angle (β) (degree)	Measured Film density (g/cc)	Theoretical film density (g/cc)	Thickness measured by FESEM (nm)	RMS roughness measured by GIXR (nm)
SAMP-1	80 ± 1	55 ± 2	55.1 ± .5	3.5 ± 0.2	2.9 ± 0.3	531 ± 2	2.1
SAMP-2	68 ± 1	37 ± 2	49.8 ± 5	6.1 ± 0.2	5.0 ± 0.2	590 ± 2	0.5
SAMP-3	57 ± 1	33 ± 2	43.8 ± .6	7.6 ± 0.2	6.4 ± 0.2	488 ± 2	0.6
SAMP-4	40 ± 1	12 ± 2	33.2 ± .7	8.4 ± 0.2	7.9 ± 0.1	361 ± 2	0.7
SAMP-5	0 ± 1	0	0 ± 1	9.1 ± 0.2	9.1	629 ± 2	0.7

frequencies. It can also be noted that contact radius (a) for a load of 1919 nN, as calculated from Eq. 3.9, is 5 to 8 nm for entire batch of thin films and thickness value as listed in Table 3.3 is between 361 to 629 nm. It is worth to note that film thickness values are significantly higher than '3a', which is generally accepted as the minimum thickness for neglecting stresses produced by film-substrate interface [92] and hence effect of substrate elastic properties on contact stiffness measurement of thin film samples can be neglected. Since the value of Poisson's ratio is not known for a thin film, we have evaluated indentation modulus rather than Young's modulus of elasticity. Dual reference method as discussed in introduction has been adopted to determine indentation modulii of the thin films. Although, in dual reference method, determination of indentation modulus is insensitive or very less sensitive to the geometry of cantilever tip, we have considered both spherical and flat tip and have taken mean of two cases. With such consideration, uncertainty is further reduced. As described in reference [65], uncertainty in dual reference method to determine indentation modulus is least when contact stiffness of two references bracket the stiffness of test sample. Consequently, for SAMP-1 & SAMP-2, BK7 glass & Si (100) references and for SAMP-3, SAMP-4 and SAMP-5; Si (100) & Sapphire references have been chosen. Eq. 3.12 has been adopted to compute indentation modulii and values are listed in Table 3.2. Indentation modulii for BK7 glass, Si (100) and sapphire has been taken from references. From Table 3.2, it is clear that indentation modulus is least for GLAD HfO_2 with a mean value of 42 GPa and increases with deposition angle with highest value of 221 GPa for SAMP-5, deposited at normal angle, which is matching with elasticity value reported by K. Tapily *et al*. [108] for atomic layer deposited HfO_2 thin film. Sources of uncertainly in the determination of indentation modulii are uncertainty in tip geometry and indentation modulii of the references. In the present case, uncertainty in indentation modulii is less than 4% in the samples, except for SAMP-1. For SAMP-1, uncertainty is 16.7% and such a high uncertainty is the

consequence of lower normal contact stiffness value of SAMP-1 than both BK7 glass and Si (100) references. Indentation modulus for used probe was calculated using Eq. 3.13 and found to be 462 ± 6 GPa.

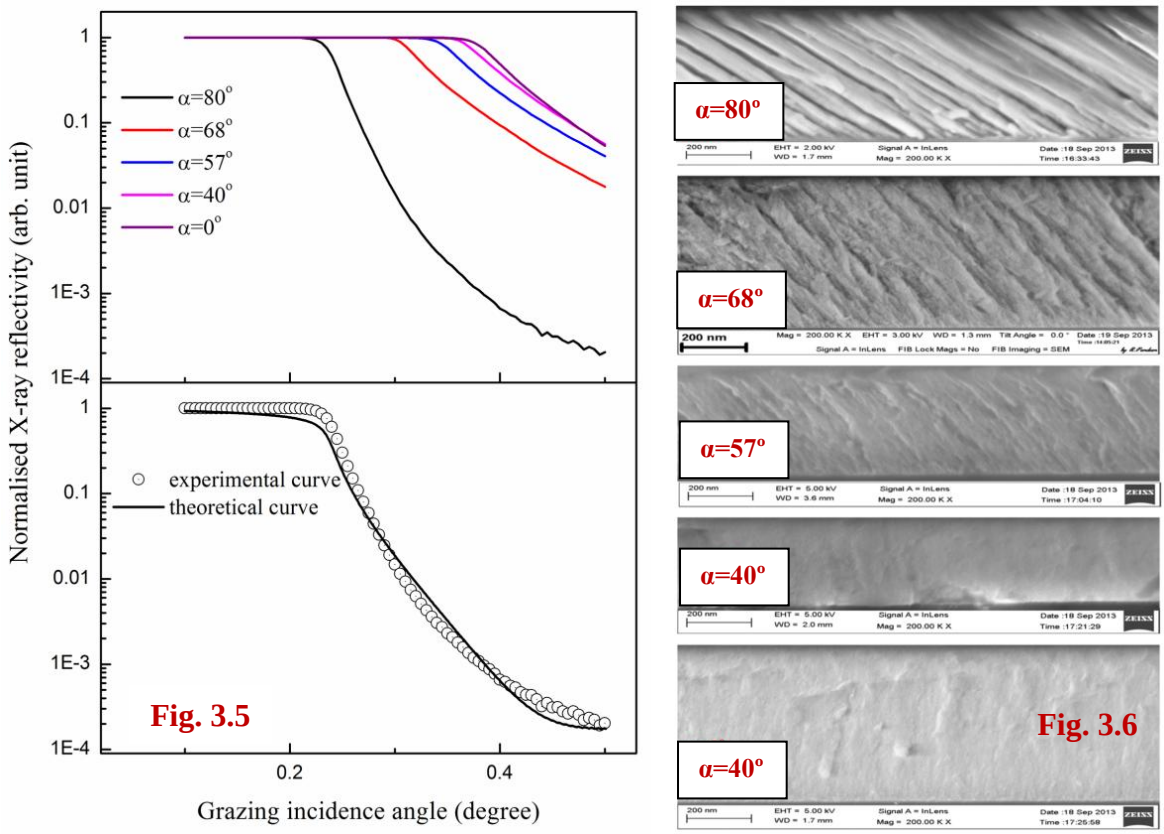

Fig. 3.5*: GIXR curves of films SAMP-1, SAMP-2, SAMP-3, SAMP-4 and SAMP-5. Experimental and theoretically simulated curves for SAMP-1 are also shown.* ***Fig. 3.6****: FESEM cross-sectional morphology for all obliquely deposited HfO_2 films.*

Normalized GIXR spectra for all the HfO_2 thin films are shown in Fig. 3.5. To determine film density and RMS surface roughness, experimental spectra have been simulated with theoretical formulation by χ^2 minimization using open source code IMD under XOP software package [109]. Density and RMS surface roughness values estimated through GIXR data analysis, are listed in Table 3.3. Cross-sectional morphology of the films has been measured by FESEM and is presented in Fig. 3.6. For SAMP-1, tilted columns are fully matured and measured tilt angle is 55°. It can be seen from FESEM images that void fraction

is highest in SAMP-1 and it decreases as the angle α decreases. Column tilt angle (β) and film thickness measured from cross-sectional SEM morphology for entire thin films are listed in Table 3.3.We have also calculated column tilt angle (β) and film density (ρ) theoretically using ballistic growth model with limited ad-atom diffusion, proposed by Tait *et al.* [20]. As per model, $\beta = \alpha - arcsin\left(\frac{1-\cos\alpha}{2}\right)$ and $\rho = \rho_0\left(\frac{2\cos\alpha}{1+\cos\alpha}\right)$; where ρ_0 is the density of film deposited at $\alpha = 0$. These theoretical formulations give values only to first approximation and actual values may differ significantly from theoretical values. At high oblique angle, measured β matches with ballistic model whereas at smaller deposition angle, ballistic model fails to match with measured column tilt angle. It is also well known that ballistic model best explains such nanostructure thin films at large deposition angles [20, 110]. Moreover, in real films, chamber pressure, rate of deposition and non-monotonic behavior also perturb the growth and tilt angle of columns. Indentation modulus and density of films are plotted in Fig. 3.7 (a) as a function of angle of deposition and follow a nonlinearly decreasing trend. Decrease in film density with α is the consequence of increase in film porosity due to tilted columnar microstructure. Increase in the films porosity with the increase in angle α leads to the decrease in indentation modulus or elastic modulus of the films. In Fig. 3.7 (b), experimental and theoretical curves of normalized indentation modulus with film porosity are shown. Theoretical curves have been generated using Boccaccini formulation considering spherical as well as cylindrical pores [111]. It can be noted that experimental data points are in between two theoretical cases (spherical & cylindrical pore geometry). It indicates the presence of complex or mixed pore geometry in obliquely deposited porous HfO_2 thin films. Similar trend has also been reported earlier [111-113].

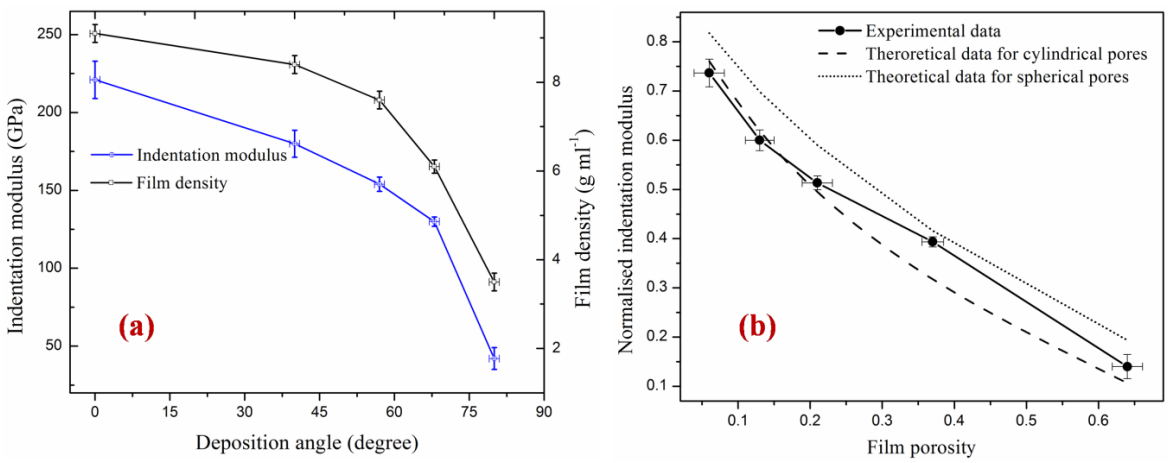

Fig. 3.7 *(a): Variation of indentation modulus and density of obliquely deposited HfO_2 thin films. (b): Experimental and theoretical curves of normalized indentation modulus as a function of film porosity.*

3.1.4.2. Local structure

XANES spectrum is highly sensitive to the coordination geometry and oxidation state of the absorbing atom. For HfO_2 films, the highest peak observed in XANES spectra is the transition of $2p_{3/2}$ electron into 5d states and the region above the edge is the transition to 6s continuum [114, 115]. No significant edge shift or change in the intensity of EXAFS spectra is observed up to the deposition angle of 40° (SAMP-4), however white-line intensity is slightly reduced for the film deposited at α= 0° (SAMP-5). The edge position suggests that all the samples are in same oxidation state. Cho *et al*. simulated the XANES spectra of t-HfO_2 and m-HfO_2 using ab-initio multiple scattering XAFS code and the presence of tetragonal phase is identified by the enhancement of small feature (denoted by 'A' in Fig. 3.8) after the white line peak. Low intensity feature in absorption coefficient spectra indicates the predominant presence of monoclinic phase for all the obliquely deposited films. Fig. 3.8 shows the normalized EXAFS spectra of HfO_2 films. In order to take care of the oscillations in the absorption spectra, $\mu(E)$ has been converted to absorption function $\chi(E)$ [116] which is energy dependent. The energy dependent absorption coefficient $\chi(E)$ has been converted to the wave number dependent absorption coefficient $\chi(k)$ using the relation,

$$K = \sqrt{\frac{2m(E - E_0)}{\hbar^2}} \qquad (3.14)$$

where, m is the electron mass. $\chi(k)$ is weighted by k^3 to amplify the oscillation at high k and the $\chi(k)k^3$ functions are Fourier transformed in R space (distance space) to generate the $\chi(R)$ versus R spectra in terms of the real distances from the center of the absorbing atom. The set of EXAFS data analysis program available within IFEFFIT software package have been used for EXAFS data analysis [117].

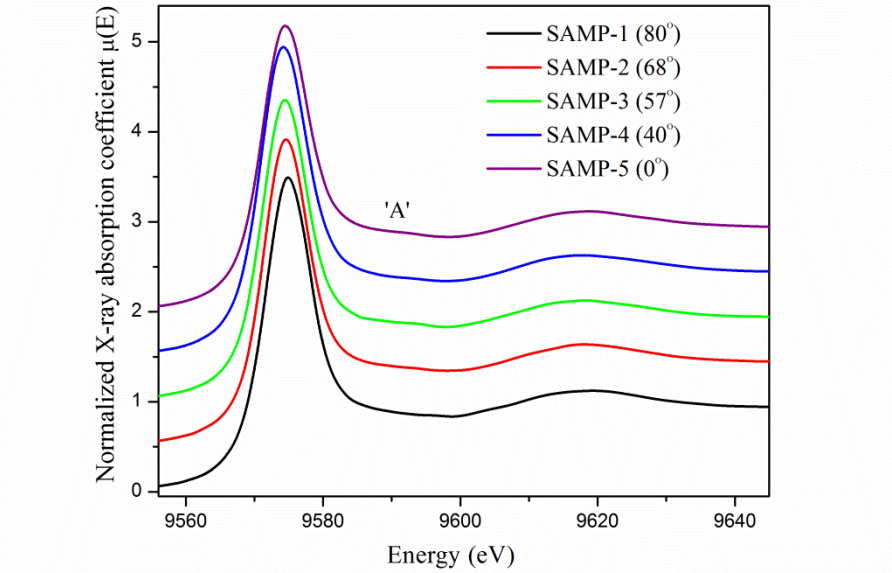

***Fig. 3.8**: Normalized EXAFS spectra of obliquely deposited HfO_2 films.*

The $\chi(R)$ versus R plots generated (Fourier transform range k =2.0-10.0 Å^{-1}) for all the films from '$\mu(E)$ versus E' spectra following the methodology described above are shown for HfO_2 films measured at Hf L3-edge in Fig. 3.9. The structural parameters (atomic coordination and lattice parameters) of m-HfO_2 and t-HfO_2 used for simulation of theoretical EXAFS spectra of the samples have been obtained from ref. [118, 119] and the best fit $\chi(R)$ versus R plots (fitting range R =1.0-3.5 Å) of the films have been shown in Fig. 3.9 along with the experimental data for all the samples. The bond distances, co-ordination numbers (including scattering amplitudes) and disorder (Debye-Waller) factors (σ^2), which give the

mean square fluctuations in the distances, have been used as fitting parameters. The best fit results of the above are summarized in Table 3.4. First peak at 1.6 Å (phase uncorrected spectrum) in Fourier transform spectrum of SAMP-1(α=80°) is contribution of

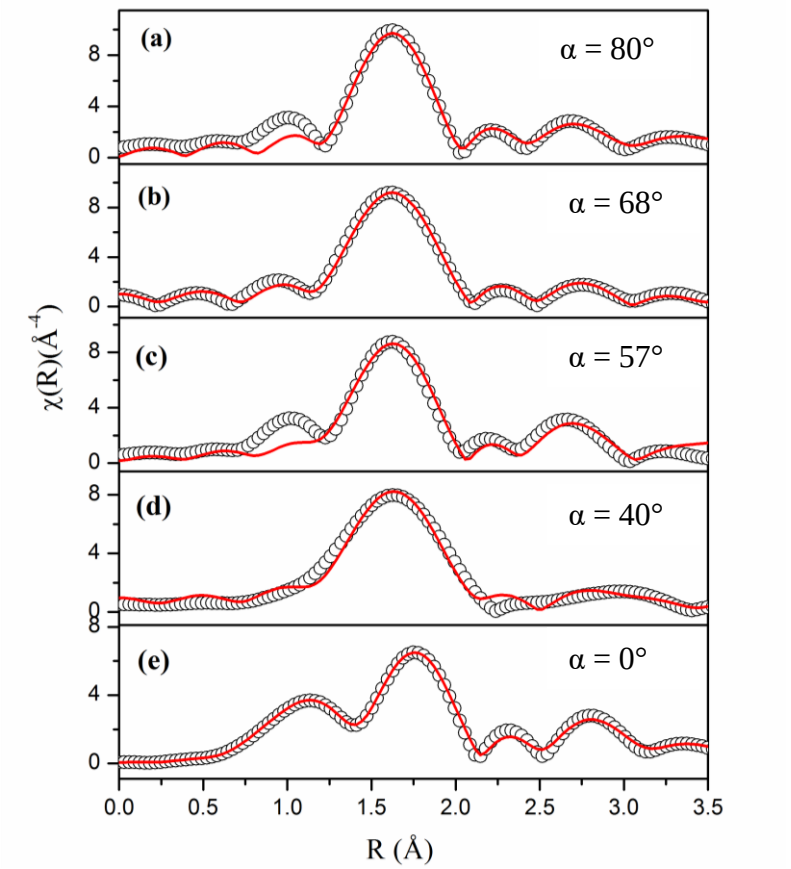

***Fig. 3.9**: Measured and theoretical plots of χ (R) vs. R for all the HfO_2 films at Hf L3-edge.*

Hf-O path at the bond length ~ 2.08 Å and 2.30 Å with five and two oxygen atoms at each coordination shell respectively. The small peak around 1 Å is contribution of low frequency oscillations of the background and not from the EXAFS signal. Similar Fourier transform spectrum has also been observed by Lysaght *et al.* in HfO_2 thin films deposited on Si substrate [120]. The coordination number obtained for first coordination peak from EXAFS fitting is in good agreement with other reports [114, 120]. The second peak around 2.9 Å is contribution of Hf-Hf coordination shell. The second peak is quite different for polymorphs of HfO_2. The theoretical EXAFS spectra shown in Fig. 3.10, are generated from the cubic (space group F_{3m3}), tetragonal (space group $P4_2/nmc$), monoclinic (space group $P2_1/c$) and

orthorhombic (Space group Pnam and Pbca) phase with ideal coordination number and Debye-Waller factor was kept at 0.003 $Å^2$. The FT EXAFS spectrum of the SAMP-1 shown in Fig. 3.9 resembles with theoretically generated spectra for monoclinic phase. The first peak

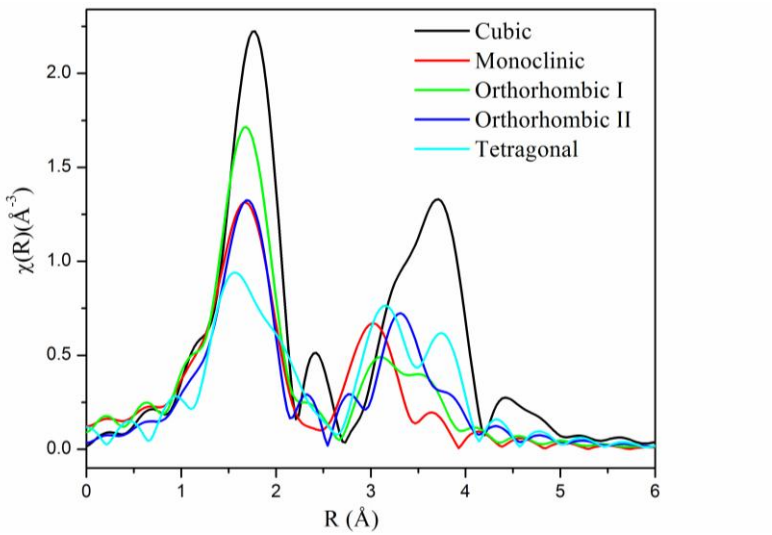

***Fig. 3.10**: Theoretically generated different EXAFS spectra (χ (R) vs. R) for different polymorphs of HfO_2.*

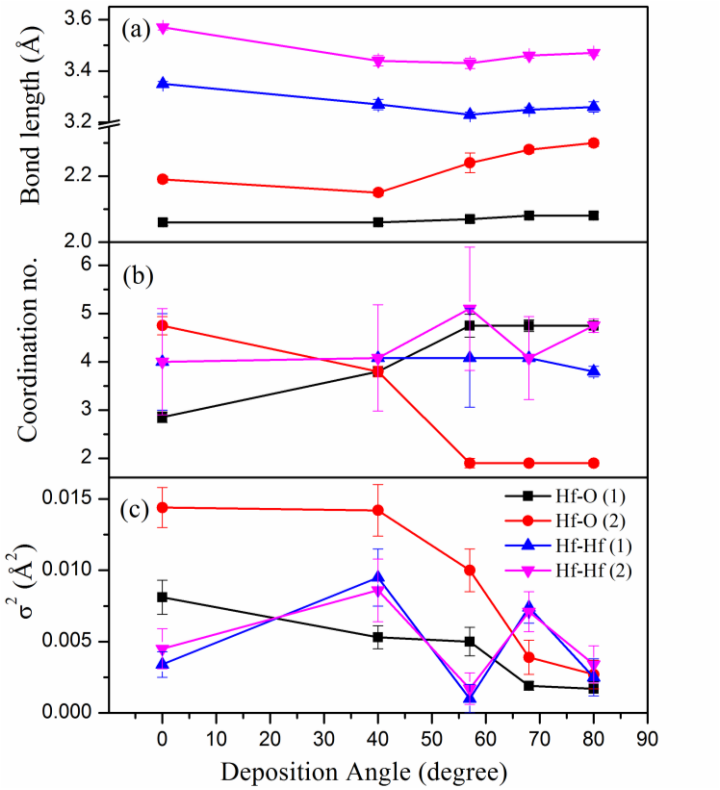

***Fig. 3.11**: Plots of different parameters obtained from EXAFS analysis for HfO_2 thin films deposited at different angles.*

Table 3.4: *Fitting parameters obtained from EXAFS analysis.*

Paths	Parameters	α = 80°	α = 68°	α = 57°	α = 40°	α = 0°
Hf-O	R(Å)	2.08 ± 0.01	2.08 ± 0.01	2.07 ± 0.01	2.06 ± 0.01	2.06 ± 0 .01
	N	4.75 ± 0.14	4.75 ± 0.12	4.75 ± 0.24	3.80±0.11	2.85 ± 0.11
	σ^2 (Å^2)	0.0017 ± 0.0005	0.0019 ± 0.0003	0.0050 ± 0.001	0.0053 ± 0.0008	0.0081 ± 0.0012
Hf-O	R(Å)	2.30 ± 0.01	2.28 ± 0.01	2.24 ± 0.03	2.15 ± 0.01	2.19 ± 0.01
	N	1.90 ± 0.06	1.90 ± 0.05	1.90 ± 0.10	3.80 ± 0.11	4.75±0.19
	σ^2 (Å^2)	0.0027± 0.001	0.0039 ± 0.0012	0.010 ± 0.0015	0.0142 ± 0.0018	0.0144 ± 0.0014
Hf-Hf	R(Å)	3.26 ± 0.02	3.25 ± 0.01	3.23 ± 0.01	3.27 ± 0.02	3.35 ± 0.01
	N	3.8 ± 0.11	4.08 ± 0.86	4.10 ± 1.02	4.08 ± 1.10	4.80 ± 1.00
	σ^2 (Å^2)	0.0025 ± 0.0013	0.0074 ± 0.0011	0.001 ± 0.001	0.0095 ± 0.002	0.0034 ± 0.0009
Hf-Hf	R(Å)	3.47 ± 0.01	3.46 ± 0.01	3.43 ± 0.02	3.44 ± 0.02	3.57 ± 0.01
	N	4.75 ± 0.14	4.08 ± 0.86	5.12 ± 1.28	4.08 ± 1.10	4.80 ± 1.01
	σ^2 (Å^2)	0.0034 ± 0.0013	0.0071± 0.0014	0.0017± 0.0011	0.0086 ± 0.0022	0.0045 ± 0.0014

is similar for the samples SAMP-1, SAMP-2 and SAMP-3 (α= 80°, 68, and 57°) and further decrease in angle α leads to peak broadening (SAMP-4, α = 40°) and finally, the peak splits in to two peaks for normally deposited film (SAMP-5). However, in case of SAMP-4 and SAMP-5, the second coordination peak is shifted to slightly higher bond length distance which indicates the presence of tetragonal phase in small amount. The fitting results are plotted with deposition angle in Fig. 3.11. It has been observed the bond- lengths are similar up to the sample deposited at 80° to 57° for Hf-O and Hf-Hf co-ordination shells. The Hf-O bond length decreases for 40° and 0°. Theoretical EXAFS spectrum generated from monoclinic phase shows five oxygen atoms at 2.10 Å and two oxygen atoms at 2.24 Å in first coordination shell. On the other hand the structure generated from tetragonal phase shows 4 oxygen atoms at 2.06 Å and 4 oxygen atoms at 2.39 Å. The coordination number increases for Hf-O (2) shell and decreases for Hf-O (1) coordination shell for SAMP-4 and ~ 4 oxygen atoms are in each Hf-O coordination shell. The change in the coordination number is indicating the presence of tetragonal phase. In case of second coordination shell Hf-Hf, bond length increases for SAMP-4 and SAMP-5. A small increase in Hf-Hf bond length is indication of presence of tetragonal phase along with monoclinic phase. The Debye Waller

factor or disorder factor, which signifies the disorder in the structure, shows increasing trend with the reduction in the deposition angle.

Lysaght *et al*. discussed the effect of grain size for tetragonal to monoclinic transformation [120]. The increase in the grain size changes the tetragonal phase to monoclinic phase. In part-2 of this chapter, morphological properties pertaining to grain size variation with deposition angle will be discussed extensively. It is shown in this work that decrease in the glancing angle leads to reduction in surface grain size due to decrease in shadowing effects and column slanting angle. The presence of the tetragonal phase for low glancing angle samples supports the reduction of grain size in the sample.

3.1.5. Summary

A set of HfO_2 thin films have been deposited on Si (100) at several deposition angles by reactive EB evaporation. Such obliquely deposited films are known to be porous and their mechanical and environmental stabilities are important issues. In order to assess mechanical stability of such thin films, indentation modulii of an entire batch of thin films have been estimated by AFAM technique. Films have also been tested for their micro-structural properties by FESEM and GIXR measurements. FESEM cross-sectional morphology shows high porosity in thin film deposited at glancing angle (80°) & tilted columnar growth and porosity decreases as the angle of deposition decreases. Variation of film density with tilt angle has been obtained through GIXR measurements. It is observed that indentation modulus is the least with a value of 42 GPa for GLAD film and highest for normally deposited film with value 221 GPa. It is concluded that the trend of decreasing indentation modulus of HfO_2 thin films is an attribute of increase in porosity with angle of deposition and porosity variation is the consequence of change in microstructure of films due to change in growth conditions.

EXAFS measurements show that monoclinic is the prominent phase of obliquely deposited HfO_2 thin films. However, a small contribution of tetragonal phase is observed for films deposited at lower deposition angles (40° and 0°). Presence of tetragonal phase for HfO_2 films deposited at lower angles can be attributed to the lower grain size.

3.2. Characterization of Micro-Roughness Parameters and Optical Properties

3.2.1. Introduction

It is well understood that surface morphology affects the functionality of thin film and multilayer devices for optical and other applications [121]. Surface morphology strongly perturbs the amount and distribution of scattered light from optical components or devices and such scattering is a performance limiting factor. Hence, it is of high importance to characterize micro-roughness parameters of obliquely deposited HfO_2 thin films to assess their surface morphological properties. Generally root mean square (RMS) roughness of surface is taken as the parameter to characterize surface morphology. However, roughness is computed from RMS distribution of heights only and does not take into account the lateral distribution of surface features. Power spectral density (PSD) provides more complete description of surface topography. PSD describes two aspects of surface roughness viz., the distribution of heights from a mean plane and the lateral distances over which height variations occur [98, 122]. Moreover, PSD also provides useful information on superstructures and fractals of surfaces. Fractal geometry and scaling concept can concisely describe the rough surface morphology [123, 124]. Surface morphology at different scales is believed to be self-similar and related to the fractal geometry. Fractal analysis can extract different kinds of information from measured surface morphology and that makes fractal approach a very attractive and useful in describing surface statistics of thin films [125-127].

In the present work, a set of HfO_2 thin films has been deposited by EB evaporation using oblique angle deposition technique. 2-D extended PSD has been computed from measured AFM data for all the obliquely deposited HfO_2 thin films by combining PSD of three different scan sizes. Different PSD models in combination have been fitted with the computed PSD to extract fractal parameters, correlation length, intrinsic RMS roughness and contribution of aggregates or superstructures to the surface roughness. Further, the refractive index and film thicknesses have been computed from transmission measurements. Very interesting correlations among micro-roughness parameters, refractive index and angle of deposition of the thin films have been obtained in this study.

3.2.2. Experimental Detail

In this part of the chapter, HfO_2 thin films were deposited at angles (α) of 0°, 40°, 50°, 57°, 62°, 68° and 80° on fused silica substrate on the same deposition system and under the same deposition process parameters as given in section 3.1.2.1 of this chapter.

AFM system was used for morphological measurements. Si cantilever probe with grown super sharp diamond like carbon (DLC) tip having tip curvature 1-3 nm, resonance frequency 198 kHz and force constant 8.8 N/m has been used for morphological measurements. Length and width of the cantilever probe used were 125 and 35 μm respectively. DLC AFM probe being very hard and anti-abrasive was chosen to get the consistency in the measurements [27]. Three different measurements having scan sizes, 2.5x2.5, 5x5 and 10x10 μm^2 with spatial resolution of 512x512 points, have been taken for all the films. For optical characterization, transmission measurements were performed from 300-1200 nm with a wavelength resolution of 1 nm on UV-VIS-NIR spectrophotometer.

3.2.3. Computation and Modeling

3.2.3.1. Extended power spectral density

PSD function can be derived from many different measurements such as, morphological measurement by surface profilometer, bi-directional reflectance distribution function and AFM measurement of surface profile [122, 128]. Among all, AFM is widely used and an excellent tool to characterize rough surfaces having height irregularities not more than few microns. There are large numbers of publications which describe surface statistics thoroughly [129, 130]. In the present paper, we have adopted the formulation described in refs. [131, 132] for the computation of PSD function from AFM scans as follows:

$$S_2(f_x f_y) = \frac{1}{L^2}\left[\sum_{m=1}^{N}\sum_{n=1}^{N} Z_{mn} e^{-2\pi i \Delta L(f_x m + f_y n)} (\Delta L)^2\right]^2 \qquad (3.15)$$

Here S_2 is the 2-dimensional PSD function, L^2 is the scanned surface area, N is the number of data points in both X and Y direction of scanned area, Z_{mn} is the surface profile height at position (m,n), f_x and f_y are the spatial frequencies in X and Y directions respectively. ΔL (L/N) is the sampling interval. Computation of PSD is further followed by transition to polar coordinates in frequency space and angular averaging (φ):

$$S_2(f) = \frac{1}{\pi}\int_0^{2\pi} S_2(f,\phi) d\phi \qquad (3.16)$$

As the PSD depends only on one parameter, it will be plotted in all our figures as a ‘slice’ of the 2-D PSD with unit ‘(length)^4’.

PSD obtained from single AFM scan has roughness in limited band of spatial frequencies and the band width depends on scan area and sampling interval. Artefacts can also constrain frequency band width of PSD. Fortunately such band width limitation can be

eliminated by combing topographical measurement performed on different scan size provided following conditions are satisfied:

(1) Spatial frequency range on which different scan size measurements are performed should overlap partially.

(2) Different PSD should be of the same order of magnitude in the overlap region.

With the conditions mentioned above, combined PSD at a frequency is given by geometrical averaging:

$$PSD_{combined}(f) = \left[\prod_{i=1}^{M} PSD_i(f) \right]^{1/M} \tag{3.17}$$

Here *M* is the PSD overlapping at concerned frequencies.

In the present work, PSD functions have been computed separately for scan area, 2.5x2.5, 5x5, and 10x10 μm^2 and combined together in a suitable manner taking care of all the conditions mentioned above. Experimental computation needs appropriate analysis models so that an extensive interpretation of PSD can provide deep insight of morphological statistical parameters of obliquely deposited HfO_2 thin films. Several mathematical models alone or in combinations have been proposed and used by researchers to interpret experimental PSD. The mostly used extended model for PSD of thin films is the sum of Henkel transforms of the Gaussian and exponential autocorrelation functions [133]. However, such model fails when wide spatial frequency range is considered. To describe roughness over large spectral frequencies, PSD model should comprise contribution from substrate, pure thin film and aggregates or superstructures.PSD of substrates generally follows inverse power law with spatial frequency (assuming fractal like surfaces) and is given as follows [134]:

$$PSD_{fractal}(f; K, \gamma) = \frac{K}{f^{\gamma+1}} \tag{3.18}$$

Here *K* is spectral strength of fractal and γ is fractal spectral indices. This PSD formulation follows self-affine surfaces only and fractal dimension *Fd* is given as follows:

$$Fd = \frac{4-\gamma}{2} \quad ; 0 < \gamma < 2 \tag{3.19}$$

When γ = 0 i.e. *Fd* = 2, surface is extreme fractal, for *Fd =1.5*, surface is Brownian fractal and for *Fd=1*, surface is marginal fractal. Apart from substrate fractal contribution towards total roughness, thin films also exhibit strong fractal characters especially at higher spectral frequencies. PSD of pure thin film is conventionally characterized by ABC or *k*-correlation model [135]:

$$PSD_{ABC} = \frac{A}{(1+B^2 f^2)^{(C+1)/2}} \tag{3.20}$$

Here, *A*, *B*, and *C* are model parameters. PSD function generated from Eq. 3.15 depicts a "knee" which is determined by model parameter *B*. At small *f* values, well below the knee, the PSD is determined by *A*. At high f values, beyond the knee, surface is fractal and the PSD is determined by parameter *C*. Equivalent RMS roughness (σ) and correlation length (τ) are related to parameters A, B and C as following:

$$\sigma_{ABC}^2 = \frac{2\pi A}{B^2(C-1)}, \tau_{ABC}^2 = \frac{(C-1)^2 B^2}{2\pi^2 C} \tag{3.21}$$

Here, σ is the contribution of pure thin film to total RMS surface roughness and its value is determined by vertical features on thin film surface. The parameter, τ accounts for lateral features and is equal to the size of geometrical grain on the surface of thin film. Models discussed so far are monotonically decreasing function of spatial frequency and do not account for any local maxima in PSD while experimental PSD functions of our films exhibits one or two local maxima due to contributions from aggregates. Such peaks in experimental PSD can be accounted by using Gaussian function with its peak shifted to a non-zero spatial frequency as described in ref. [136]. For our thin films, we have used the combination of all the three PSD models and the combined formulation is as follows:

$$PSD_{Total} = \frac{K}{f^{\gamma+1}} + \frac{A}{(1+B^2 f^2)^{(C+1)/2}} + \sum_m \pi\sigma_{sh,m}^2 \tau_{sh,m}^2 \, exp\left\{-\pi^2 \tau_{sh,m}^2 (f - f_{sh,m})^2\right\} \quad (3.22)$$

Here, σ_{sh} and τ_{sh} correspond to height and size of superstructure. PSD functions of all the thin films have been fitted using above formalism to obtain useful surface statistical parameters.

3.2.3.2. Determination of optical constants

Prior to the determination of optical constants of thin film, substrate transmission spectra was fitted using Cauchy's dispersion relation [72] to estimate substrate refractive index. Subsequently, transmission spectra of single layer thin film were fitted using Sellmeier's dispersion model and χ^2 (chi) square minimization [71, 72] was carried out to determine the best fit values of the fitting parameters including refractive index and thickness of the films.

3.2.4. Results and discussion

3.2.4.1. Micro-roughness parameters

As mentioned above, we have performed AFM scans of same size at 8 different places over thin film surface. In Fig. 3.13, average PSD function of a representative film deposited at an angle 62°, computed from Eq. 3.15 for scan size 2.5x2.5 μm^2 at different places is shown. It is worth to notice that after averaging, fluctuations in PSD profile are reduced significantly. Extended PSD functions which have been computed from Eq. 3.15, 3.16 and 3.17, are plotted in Fig. 3.14 for all the films. The PSD function of film at 80° depicts a big jump from others. Such a jump is the attribute of bigger vertical and lateral features on the surface of thin film deposited at 80°. The Eq. 3.22 for combined PSD model has been used to fit the experimental extended PSD. The best fit parameters such as intrinsic film roughness and correlation length etc. are listed in Table 3.5. Experimental and fitted PSD for thin films deposited at angles 80° and 0° along with contributions of different model components to total PSD are shown in Fig.

3.15 (a) and Fig. 3.15 (b) respectively. Fitting quality justifies the use of the combined PSD model. It can be noted from Table 3.5 that all the films except the film at 80°, has been fitted using two shifted Gaussian peaks. PSD of film at 80° fits very well using single shifted Gaussian peak only. Fig. 3.16 presents a very interesting trend of intrinsic RMS roughness (σ_{ABC}) and spectral strength of fractal (K) with respect to angle *α*. For lower values of *α*, σ_{ABC} is nearly constant (from 0 to 50^{o}). For intermediate angles (50° to 70°), it depicts a decreasing trend and then again increases steeply with an increase in angle α (α ≥ 70°) exhibiting the highest value for the film deposited at 80°. Such variation can be explained in the light of atomic shadowing, re-emission and diffusion of ad-atoms. At glancing angle (α ~ 80°) as shown Fig. 3.12, the velocity component $V\cos\theta$ (*θ=90-α)* of incoming ad-atoms along the substrate surface is highest (Θ~10°) and it makes ad-atoms to diffuse on substrate surface and try to smoothen surface.

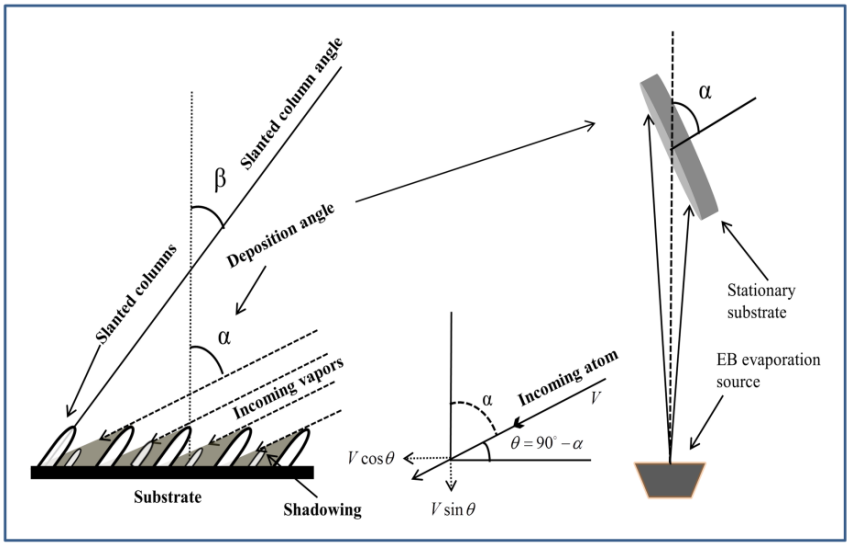

***Fig. 3.12**: Schematic of oblique angle deposition and mechanism for slanted columnar growth due to shadowing effects.*

However, in EB evaporation technique, diffusion due to ad-atom velocity along surface is very small. The velocity component $V\sin\theta$ of ad-atom perpendicular to the plane of

substrate is lowest and hence sticking probability of ad-atom to substrate is lowest at α = 80°. Consequently, re-emission of ad-atoms is highest and it gives smoothing effect to the surface of film with slanted angle columnar growth [137].

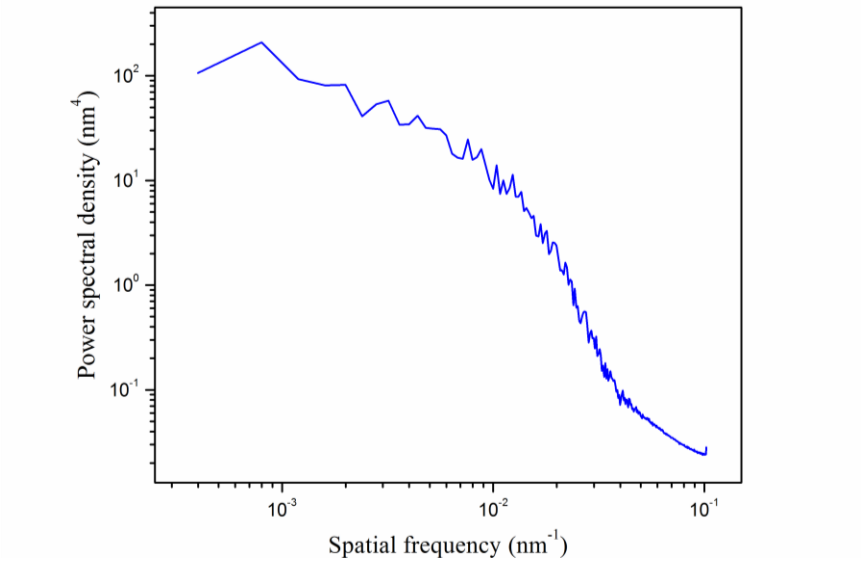

***Fig. 3.13**: Shows the reduction of noise in PSD by averaging of PSD functions of scans size 2.5 x 2.5 µm^2 measured at 8 different places for the film deposited at an angle of 62°.*

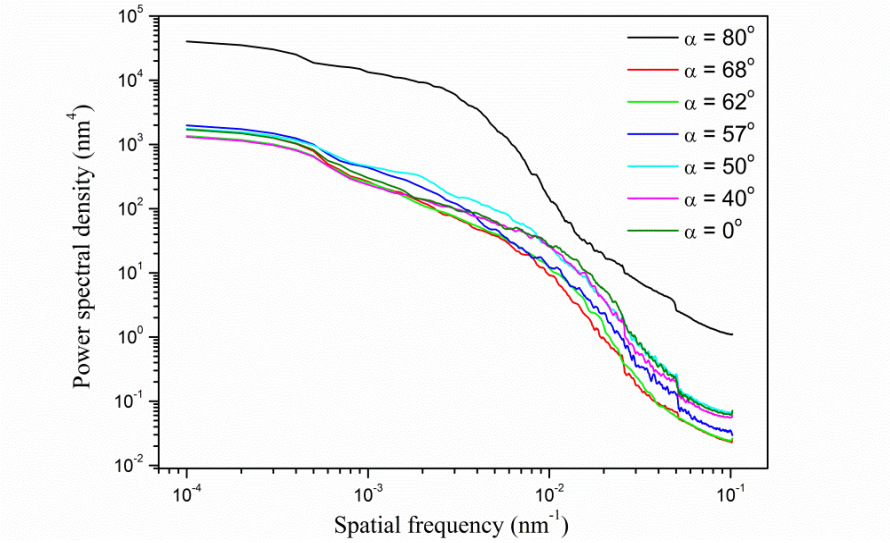

***Fig. 3.14**: Displays extended PSD for all the obliquely deposited HfO_2 thin films.*

On the other hand, surface roughening due to atomic shadowing effect is very high and dominates surface smoothing effects due re-emission and diffusion of ad-atoms at α = 80° [3, 137]. Consequently, GLAD film depicts the highest surface roughness amongst all. As the

angle α decreases, shadowing effect tends to diminish very fast [3]. Sticking probability of ad-atoms increases whereas $V\cos\theta$ decreases with the decrease in angle α. For angle α below 70°, shadowing offers very small roughening effects. Even though re-emission and diffusion of ad-atoms also decreases with decrease in angle α, smoothing due to re-emission and diffusion of ad-atoms starts dominating surface roughening due to shadowing effects. Consequently, effective smoothing of surface for intermediate angles (70°-57°) occurs and σ_{ABC} depicts the lowest values for intermediate oblique angles. As the angle α decreases further, atomic shadowing creates negligible roughening effects. Below 50° angle of deposition, slanted columnar growth tends to disappear and straight and dense columnar growth occurs [27]. Smoothing effect also decreases due to low re-emission and diffusion of ad-atom for lower values of angle α. As a result, σ_{ABC} increases slightly and then saturates as the angle α tends to 0° (normal deposition). Spectral strength of fractal (K), which is the measure of strength of fractal components in surface, follows the similar trend as of σ_{ABC} with angle α. Similar trend of σ_{ABC} and K indicates a proportionality relation between them. As listed in Table 3.5, correlation length (τ_{ABC}) represents the surface grain size which increases monotonically from angle α = 0° to α = 65°. The grain size increases steeply with further increase in angle α. The lowest and the highest value of grain size are 26.7 and 74.6 nm for thin films at 0° and 80° respectively. The variation of grain size with angle α is also corroborated by 2-D AFM surface morphologies shown in Fig. 3.17.The highest grain size of film at 80° is the consequence of dominant atomic shadowing effects at high oblique angle. Diameter of slanted columns is very high (~ 50-100 nm) at glancing angles deposition as shown in Fig. 3.6, which ultimately leads to bigger grain size on surface. Decrease in angle α leads to reduction in surface grain size due to a decrease in shadowing effects and column slanting angle. In Table 3.5, the values of fractal indices (γ) and fractal dimension (Fd) are listed. The value of γ increases gradually with angle α and saturates for $\alpha \geq 62°$.

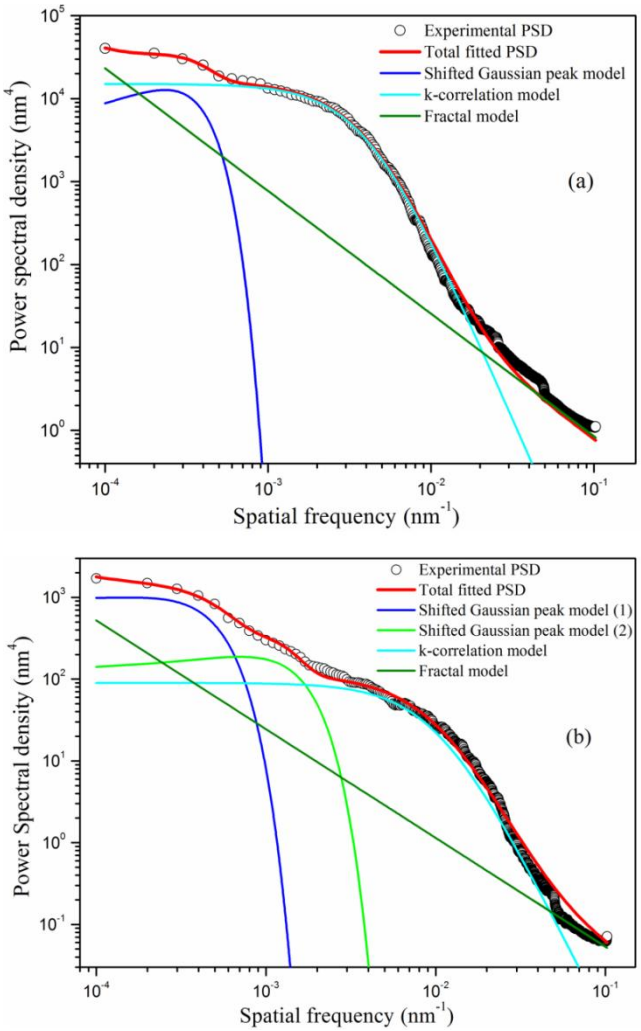

Fig. 3.15(a), (b)*: Experimental and fitted extended PSD of thin film deposited at angles 80° and 0° respectively. Fitted PSD has also been de-convoluted in different model components.*

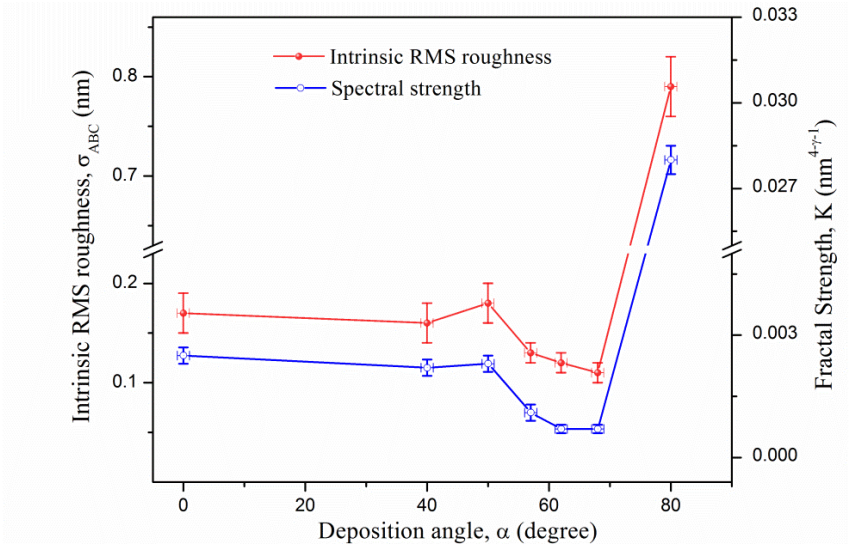

Fig. 3.16*: Variation of intrinsic RMS roughness and fractal spectral strength of obliquely deposited HfO_2 thin films with angle of deposition.*

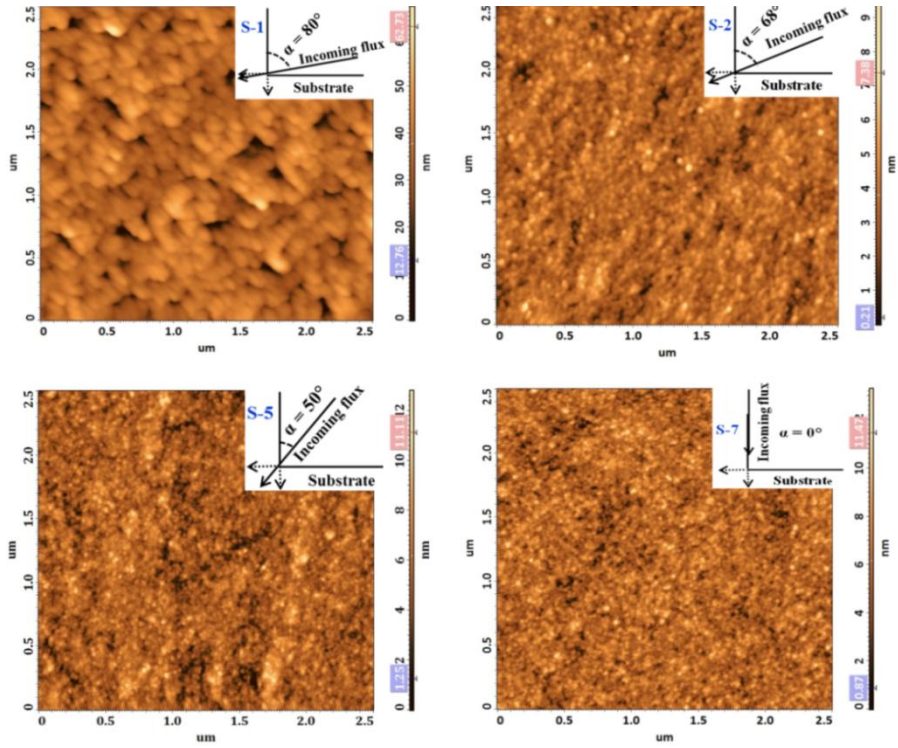

Fig. 3.17*: *2-D AFM images of obliquely deposited HfO_2 thin films.

The value of γ varies from 0.33 to 0.48 and hence *Fd* varies from 1.84 to 1.76. The value of *Fd* is close to 2 for all the film samples. It indicates that thin film surfaces are between extreme and Brownian fractal. Relatively lower fractal dimension for near glancing angle deposited films indicates that the thin film surfaces are more close to Brownian fractal. The values of σ_1, τ_1 and σ_2, τ_2 which are roughness contribution and correlation length of aggregates or superstructures for shifted Gaussian peak-1 and peak-2 respectively, are listed in Table 3.5. Fig. 3.15 (a) and (b) indicate that the contribution of aggregates to total PSD is dominant for lower spatial frequencies and negligible for higher frequencies. Aggregates size and their contribution towards PSD vary randomly with α and hence no correlation can be set between shifted Gaussian peak parameters and deposition angle α.

3.2.4.2. Optical properties

Fig. 3.18 (a) presents the transmission spectra of all the thin films. Transmission spectra depict a decrease in contrast of interference fringes with the increase in angle α. Such

***Table 3.5**: Fitting and derived morphological parameters from modelling of extended power spectral density function.*

Deposition angle, α (degree)	Γ	K ($nm^{4-\gamma-1}$) $x10^{-4}$	A (nm^4)	B (nm)	C	σ_{ABC} (nm)	τ_{ABC} (nm)	F_d	σ_1 (nm) $x10^{-4}$	τ_1 (nm)	f_{s1} (nm^{-1}) $x10^{-5}$	σ_2 (nm) $x10^{-4}$	τ_2 (nm)	f_{s2} (nm^{-1}) $x10^{-4}$
0	0.33	25	90	98	3.15	0.17 ± 0.02	26.7 ± 0.8	1.84	214	841	17	273	283	7
40	0.36	22	110	105	3.35	0.16 ± 0.02	30.8 ± 0.8	1.82	170	870	22	210	250	6
50	0.38	23	188	121	3.45	0.18 ± 0.02	36.3 ± 0.8	1.81	174	945	25	344	249	9
57	0.40	11	102	125	3.45	0.13 ± 0.01	37.1 ± 0.8	1.80	232	835	15	500	200	5
62	0.48	7	95	130	3.50	0.12 ± 0.01	39.1 ± 0.8	1.76	167	948	21	176	380	9
68	0.48	7	99	147	3.50	0.11 ± 0.01	44.1 ± 0.8	1.76	194	940	19	246	291	6
80	0.48	280	15076	248	3.50	0.79 ± 0.03	74.6 ± 0.9	1.76	437	1510	24	Nil	nil	nil

outcome may be attributed to the increase in porosity in the films with increase in angle α. Again variation in film porosity is governed by film microstructure which changes due to varying atomic shadowing effect with deposition angle. It may also be noted from Fig. 3.18 (a) that for film at 80°, absorption for wavelengths less than 350 nm increases very fast and this may be due to the contribution of multiple reflections of light between the columns inside the film and due to high diffused scattering from rough surface [77, 138]. Multiple reflections inside thin film deposited at the glancing angle, arise from high inter-columnar distance. As the angle α decreases, inter columnar distance reduces steeply and become very small compared to wavelengths of interest for lower values of angle α. Hence, the films deposited at lower oblique angle do not show any additional absorption. In Fig. 3.18 (b), experimental and fitted transmission curves are shown for a representative film deposited at 62°. Suitability of Sellmeier's dispersion model is justified by the fitting quality. Film thicknesses determined from modeling of transmission data are 622, 487, 390, 478, 398, 426 and 421 nm for the films deposited at angles 80°, 68°, 62°, 57°, 50°, 40°, and 0° respectively.

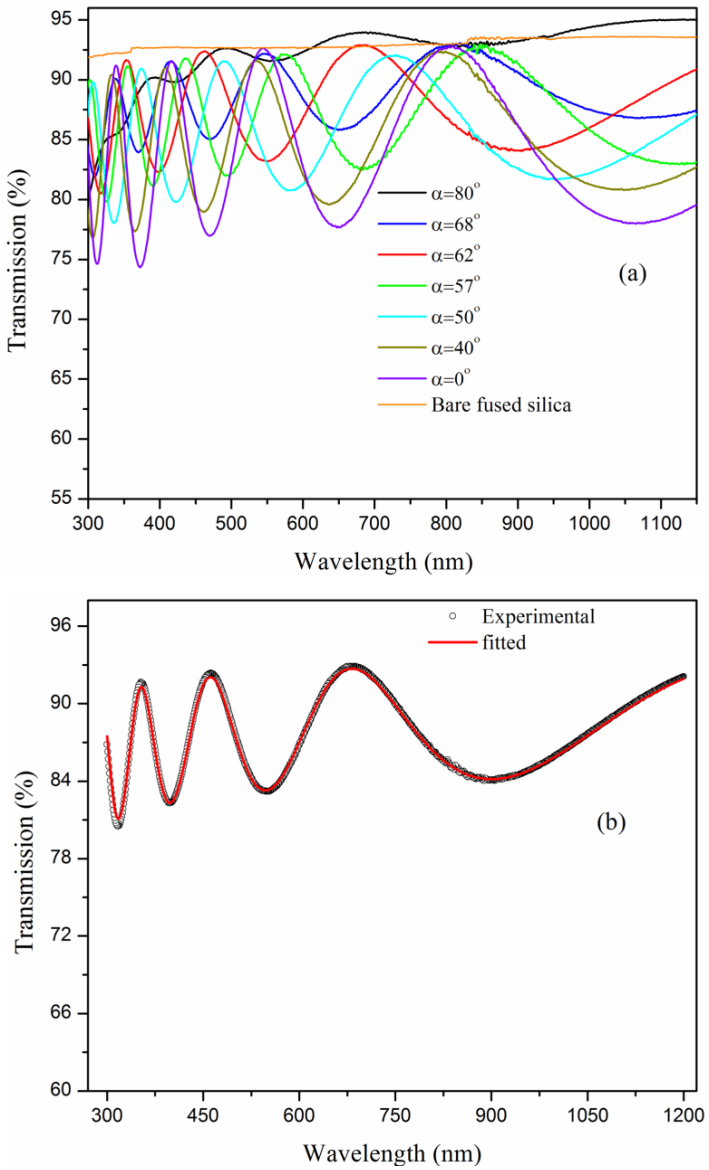

Fig. 3.18 *(a): Measured transmission spectra for all obliquely deposited HfO_2 thin films and* ***(b)*** *Measured spectra and fitted curve using the Sellmeier's dispersion model for the film deposited at an angle of 62°.*

Fig. 3.19 presents the dispersion of refractive index of all the films deposited at different angles. It is obvious that all the films show the similar dispersion in refractive index. As the angle α increases from 0° to 62°, dispersive values of refractive index decrease gradually. However, as the angle α increases further, refractive index starts decreasing steeply and possesses the lowest dispersive values for GLAD (80°) thin film. Decrease in refractive index with α is the consequence of increase in film porosity.

Finally, the variation of grain size and refractive index with deposition angle are plotted together in Fig. 3.20. It is found that grain size depicts an opposite trend of variation compared to refractive index with deposition angle α. Such behavior indicates a strong correlation between grain size and refractive index. Refractive index at wavelength of 600 nm varies from 1.37 to 1.93 as the angle α varies from 80° to 0°. The lowest refractive index of 1.37 is exhibited by GLAD film and is less than the refractive index of fused silica substrate (n=1.45 at λ=600 nm). Consequently, thin film deposited at 80° gives an antireflection effect [71] due to interference between light reflected from air/film and film/substrate interfaces and the same is shown in Fig 3.18 (a). From above discussion, it is concluded that variation in microstructure of obliquely deposited HfO_2 thin film due to varying deposition angle has great impact on their optical and morphological properties.

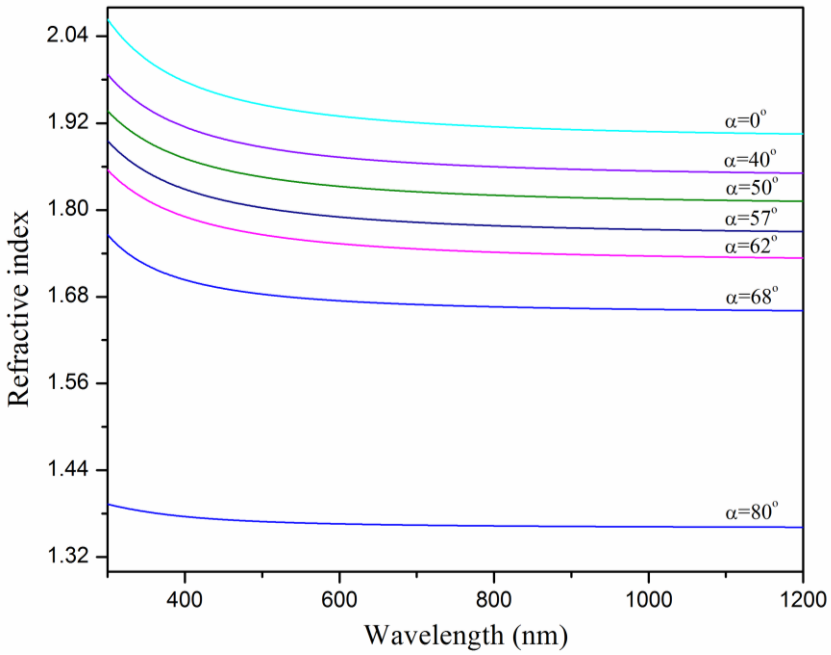

***Fig. 3.19**: Plot of dispersive refractive index for all the HfO_2 thin films.*

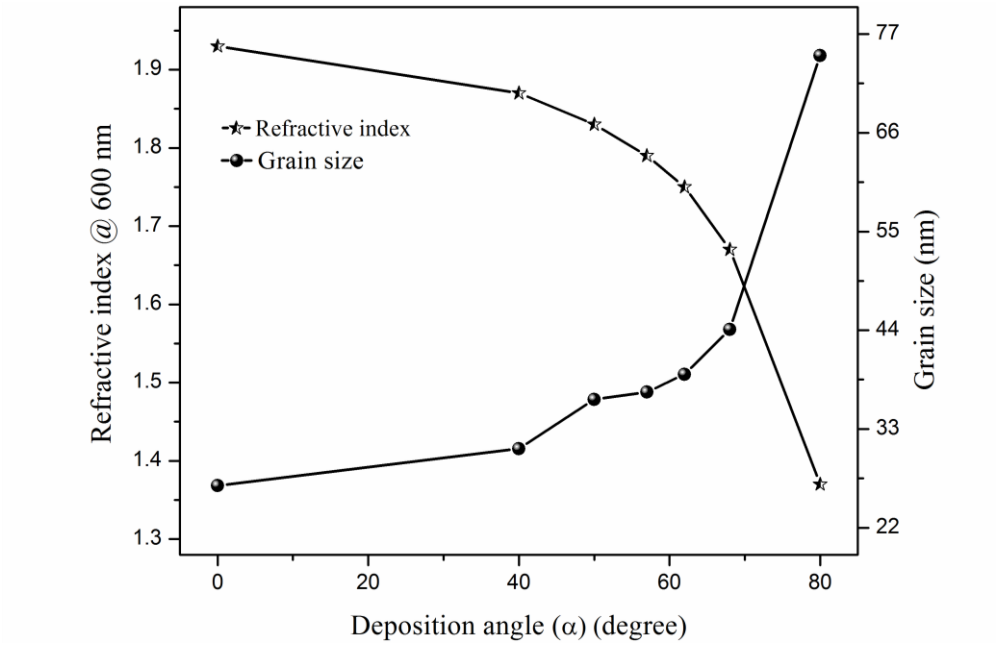

***Fig. 3.20**: Variation of refractive index and grain size with angle of deposition.*

3.2.5. Summary

Several HfO_2 thin films have been deposited at different oblique angles varying from 0° to 80° by reactive electron beam evaporation technique. Such thin films possess special microstructures due to atomic shadowing and limited ad-atom diffusion during growth. Varying microstructure with deposition angle affects morphological and optical properties of thin film. Effect of deposition angle on morphological and optical properties of obliquely deposited HfO_2 thin films has been studied extensively through extended power spectral density and optical transmission measurements. Among all the thin films, GLAD film exhibits the highest grain size and intrinsic RMS surface roughness. Intrinsic roughness and fractal spectral strength obtained from the analysis of extended power spectral density follow the similar trend with deposition angle. Behavior of surface morphological statistical parameters and refractive index with deposition angles have been explained by the combined effect of atomic shadowing, re-emission of ad-atoms and diffusion of ad-atoms.

CHAPTER 4: GLANCING ANGLE DEPOSITION OF HfO_2 THIN FILMS BY MAGNETRON SPUTTERING

4.1. Introduction

As discussed in chapter 1 and 3, GLAD thin films are often porous and RMS surface roughness is higher compared to the normal thin films [139, 140] due to ballistic atomic shadowing effects. Even though films with such porous and rough surface morphology are undesirable in many of the application including multilayer thin film based optical devices, this has got certain advantages also. For example, GLAD thin films find application as broad-band antireflection coatings [141, 142], photonic band-gap crystals [40] omni-directional reflectors [143], sensors [144], super-hydrophobic coatings [145] etc., due to the porous interior and rough surface nature of the films.

One of the vital requirements for making porous thin films with nanostructures is the collimation of the deposition flux [3, 140] which is a favorable feature of evaporative deposition technique. A plenty of work on GLAD has been carried out by physical evaporation technique where a flux of particles is supplied from an evaporation source under high vacuum which ensures a collision-less regime of the particle movement. The magnetron sputtering which suffers from wide angular distribution of deposition flux and workability at higher pressure is comparatively less explored [140] for glancing angle deposition. Hafnium oxide (HfO_2) as discussed in chapter 3, is a technologically important optical material which is widely studied both by conventional magnetron sputtering deposition technique [146] as

well as other physical vapour deposition techniques [147, 148]. However, study on GLAD HfO_2 thin films especially by magnetron sputtering is scanty. Present investigation of RF magnetron sputtered HfO_2 thin film is primarily oriented towards glancing angle processes and various related outcomes. The recent work [149] on GLAD magnetron sputtering deposited HfO_2 thin films shows that the films exhibit high water contact angle proving the suitability of such films as hydrophobic thin film layer. But, their study of optical properties shows very less reduction in refractive index (r.i.) and hence less porosity of the films; specifically their obtained r.i. is in the rage of 1.90 to 1.93 while the values of refractive index for HfO_2 thin films in literature varies from 1.85 to 2.15 [150-152].

Present investigation is especially aimed at exploring the effect of target to substrate distance on morphological, optical and structural properties of RF magnetron sputtered HfO_2 thin films being deposited under glancing angle. Target to substrate distance (D_{TS}) is an important parameter in controlling the growth and quality of thin film. The average energy of the sputtered atoms is of the order of several eV [153] and the energy of the ad-atoms due to the collision, deposition flux density, deposition flux collimation [3] gets changed with increase in target to substrate distance. These are all important factors of deposition dynamics which can affect the properties of films. Thaveedeetrakul *et al.* [154] reported that due to the energy loss of the ad-atoms with increasing D_{TS}, there is lesser surface diffusion and hence lesser crystallinity of the DC magnetron sputtered zirconia thin films. Jeong *et al.* [155] reported that with decreasing D_{TS}, the growth rate increases while the electrical resistivity as well as crystal size in the aluminium-doped ZnO films decreases. Wuhrer *et al.* [156] has reported that with increase in D_{TS}, AFM RMS roughness increases for sputter deposited nano-structured titanium-aluminium nitride coatings.

In present work, the effect of substrate-target distance on the crystallinity, surface morphology and optical properties of HfO_2 thin films deposited under glancing angles using

RF magnetron sputtering technique has been studied. Under present investigations two sets of HfO_2 thin films have been deposited at 82° and 86° of glancing angle; each set being deposited at four different targets to substrate distances in the range 70 to 125 mm by radio frequency magnetron sputtering deposition technique. AFM measurements of the samples have been carried out for morphological study. The spectroscopic ellipsometry have been carried out for optical study of the thin films. Densities of few of the samples have been estimated through GIXR measurement. Crystallographic structure of the samples was studied by GIXRD measurement.

4.2. Experiments

The HfO_2 thin films have been deposited on silicon wafer by RF magnetron sputtering deposition technique (custom made deposition system) with target (Cerac, 99.9% purity) having diameter of 76 mm and thickness 5 mm. Detailed description of the sputtering system has been given in chapter 1 of this thesis. Prior to each deposition, base pressure of 1.0 $x10^{-6}$ mbar was achieved in the deposition chamber and HfO_2 target was pre-sputtered [146, 157] for ~ 300 sec at high RF power (500 W) to remove surface contamination, if any. All the films were deposited at 5.6 x 10^{-3} mbar argon (Ar) gas pressure and at 250 Watt of RF power. A multichannel quartz crystal (Maxtech Inc. model: MDC-360 C) was positioned in between target and substrate as shown in Fig. 4.1. It is to be noted that since the quartz crystal thickness monitor is at fixed height, the thickness value derived from there is only taken as guiding parameter for monitoring the process stability rather than for exact quantitative thickness determination. For present investigations two sets of HfO_2 thin film have been deposited at 82° and 86° of glancing angle as shown in Fig. 4.1; each set being deposited at four different target to substrate distances visualizing 70 mm, 90 mm, 110 mm, 125 mm by RF magnetron sputtering deposition technique. Duration of deposition for each sample was varied for different samples in order to keep approximately similar thickness according to the

measured deposition rate by online quartz crystal thickness monitor. For the reason mentioned previously, exact value of thickness of the film could be monitored by spectroscopic ellipsometry as mentioned below. The typical deposition rate was in the range of 1 nm/min - 5.6 nm/min.

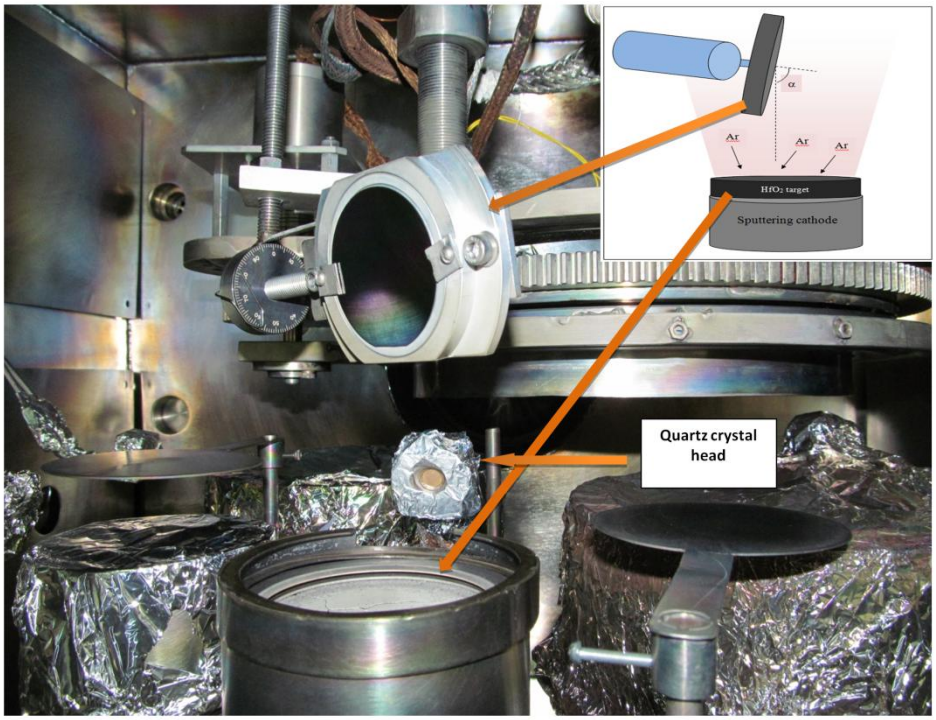

Fig. 4.1: *RF magnetron sputtering system with GLAD set-up (schematic is shown in inset).*

Morphological characterization of the films has been carried out by AFM measurements. Semi-contact mode of the AFM with super sharp DLC tip grown on Si cantilever, having radius of curvature 1-3 nm, force constant 8 N/m and resonance frequency 190 kHz, has been chosen for the efficient topographic measurements of the thin films. Optical characterization of the films has been carried out by rotating polarizer type spectroscopic ellipsometer. The ellipsometry spectrum was measured for the samples in the wavelength range 200-900 nm at 70° angle of incidence. GIXR measurement has also been carried out for few of the samples in order to estimate the density to cross check the trend in refractive index as estimated from

ellipsometry. The GIXR measurements have been carried out by using a 1.54A° Cu Kα source (Brooker D8 discover) in the glancing angle range of 0 to ~ 0.9° in steps of 0.005°.

Structural study of GLAD samples was carried out by Rigaku Ultima-IV XRD machine by recording the GIXRD pattern of the samples in 2θ geometry with a scan speed of 1° per minute in the angular range 20-80°. The grazing incidence angle of X-ray on the sample was kept at ~ 0.5°.

Since the spatial non-uniformity in the GLAD deposited samples is quite likely to occur, all the above measurements have been taken at the centre of the 1 inch diameter sample in order to retain the consistency.

4.3. Results and Discussion

4.3.1. Morphological Properties

All the HfO_2 samples were subjected to AFM measurements to examine the variation of surface morphology due the change in target to substrate distance and the effect of deposition angle on it. Fig. 4.2 shows 3D AFM image of all the HfO_2 GLAD samples at different D_{TS} for both at 82° and 86° angles of deposition. It can be seen from Fig. 4.2 that compared to other samples, the sample deposited at 110 mm D_{TS} and at 82° glancing angle exhibits prominent nanostructures. The surface roughness calculation yields that the estimated values of RMS roughness of the films lies in the range 2 to 12 nm.

Fig. 4.3 shows the 2-dimensional (2D) morphological AFM images of all the HfO_2 films which show the 2-D projected images of the grains which can be mainly classified as approximately circular and elliptical in shape. To further confirm their shape (in some of the films), we also carried out measurement by rotating the samples and found that shape of the grain remains unaltered with only the surface feature being rotated. The approximate shape

and dimension of these 2-D projected grains are tabulated in Table 4.1. The error in grain size mentioned in the table represents the deviation of the estimated value from its mean value as

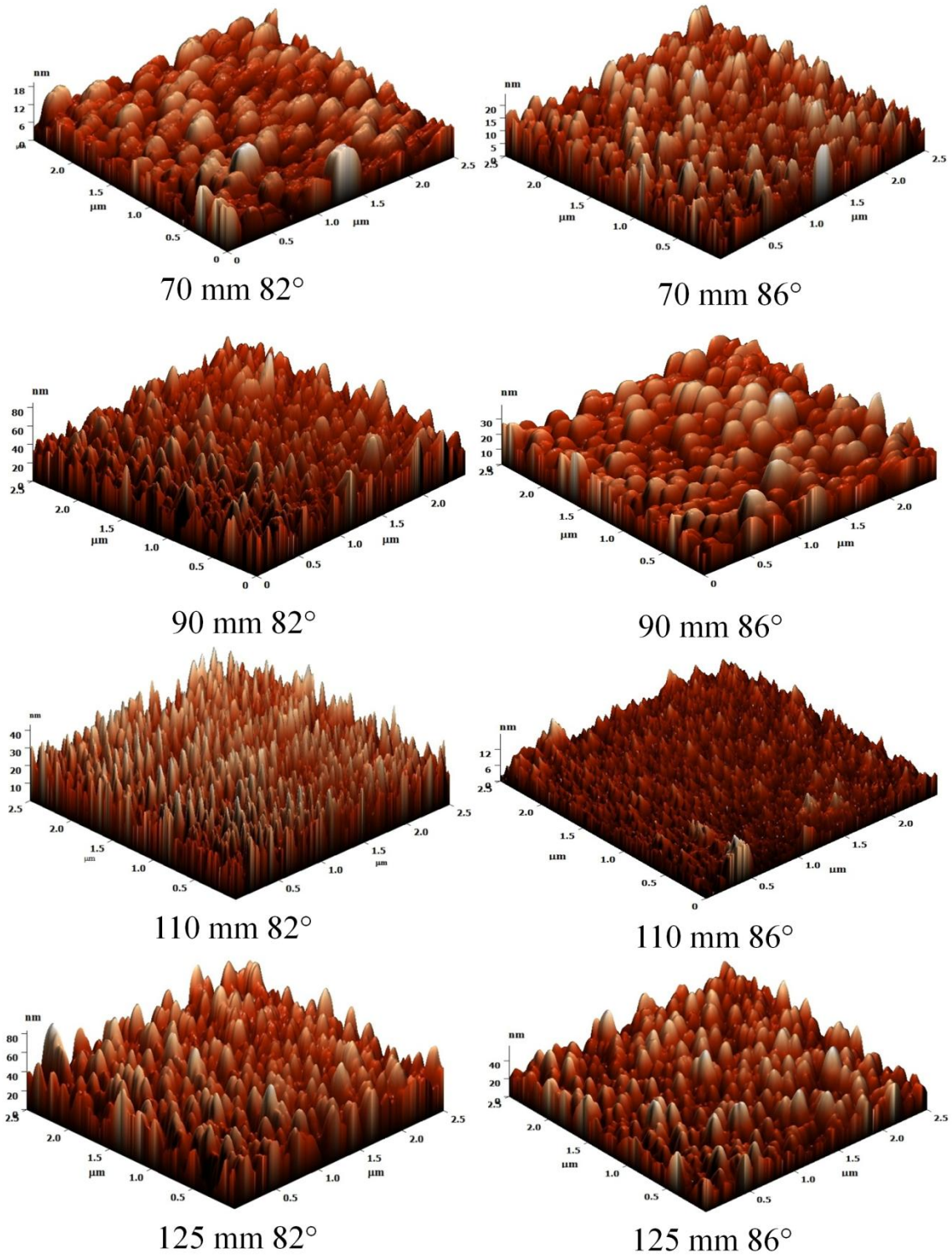

Fig. 4.2: *AFM images of HfO_2 GLAD films deposited at different target-substrate distance and at 82° and 86° angles of deposition (X axis: 2.5µm, Y axis: 2.5 µm, Z axis: is nm unit).*

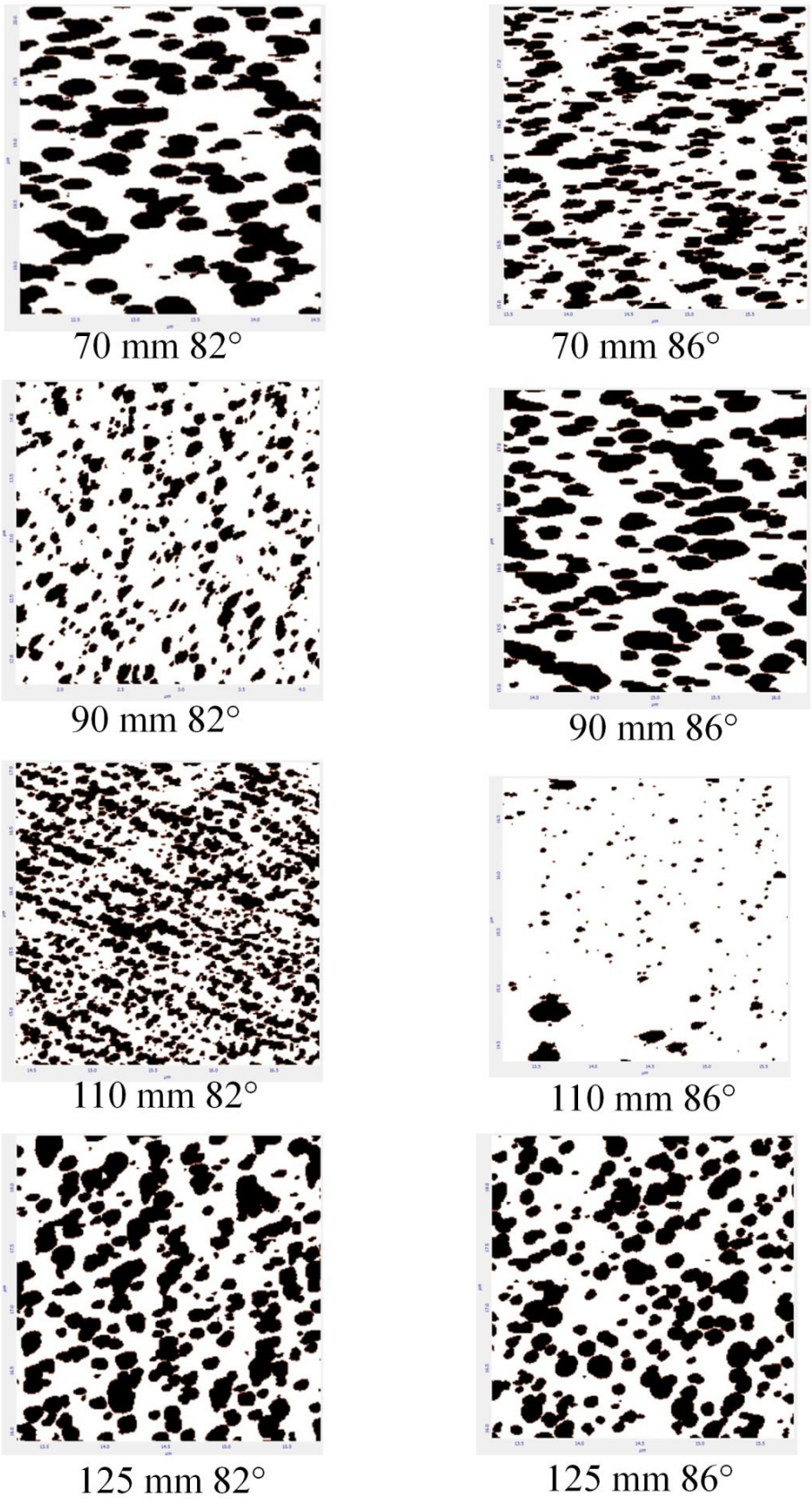

Fig. 4.3: *Surface morphological images (grain size) of HfO_2 thin films deposited at different target-substrate distances and 82° and 86° angles of deposition.*

estimated over 20 numbers of grains for each samples. The table shows that for both 82° and 86° glancing angle of depositions, for lower D_{TS} the grains are elliptical in shape and as D_{TS} has increased beyond approximately 70-90 mm, the grains are predominately circular in shape. This is probably because at shorter D_{TS}, the higher kinetic energy (KE) of ad-atoms has caused higher nucleation density [158] and higher surface diffusion. As a consequence, elongated grains of approximately elliptical in shape are produced by method of coalescence [159] of the neighboring grains.

Table 4.1*: Geometrical shape and size of grains on surface of GLAD HfO_2 thin films as obtained from AFM measurements.*

Deposition angle (82°)			
D_{TS} (mm)	Grain shape	Grain size (nm)	Average grain area (nm^2)
70	Elliptical	(270 ± 20) x (120 ± 20)	25,446 ± 6124
90	Circular	130 ± 20	13,351 ± 4108
110	Circular	80 ± 10	5056 ± 1264
125	Circular	150 ± 20	17,775 ± 4740
Deposition angle (86°)			
D_{TS} (mm)	Grain shape	Grain size (nm)	Average grain area (nm^2)
70	Elliptical	(240 ± 20) x (90 ± 10)	17,064 ± 3312
90	Elliptical	(260 ± 20) x (110 ± 10)	22,594 ± 3312
110	Circular	70 ± 10	3871 ± 1083
125	Circular	140 ± 20	15,484 ± 4335

The average grain area was calculated from these images and plotted in Fig. 4.4. The area of elliptical grains were calculated by approximating the grains as an ellipse with a defined minor and major axis which are equal to the larger and smaller diameter of the actual grains [160]. The error bar of grain area was calculated based on the grain size mentioned in Table 4.1. Fig. 4.4 shows that for both sets of films, grain area has decreased with increase in D_{TS} in

the range 70-110 mm but with the subsequent increase in $D_{TS,}$ the grain area has increased. To further verify the trend of this graph, we have added three more additional points for both the angles of deposition at 60 mm, 100 mm and 135 mm target to substrate distance. The evolution of grain area with target to substrate distance is in accordance with the deposition rate. The higher deposition rate has resulted in larger diffusion [161] of the ad-atoms probably causing the increase in grain size. The correlation of morphology with the deposition rate was also demonstrated by Jie *et al.* [50] where the study on GLAD HfO_2 thin films deposited by EB evaporation technique showed that the shape factor defined by the ratio of deposition rate to the substrate rotation speed plays an important role in determining the morphology of the samples.

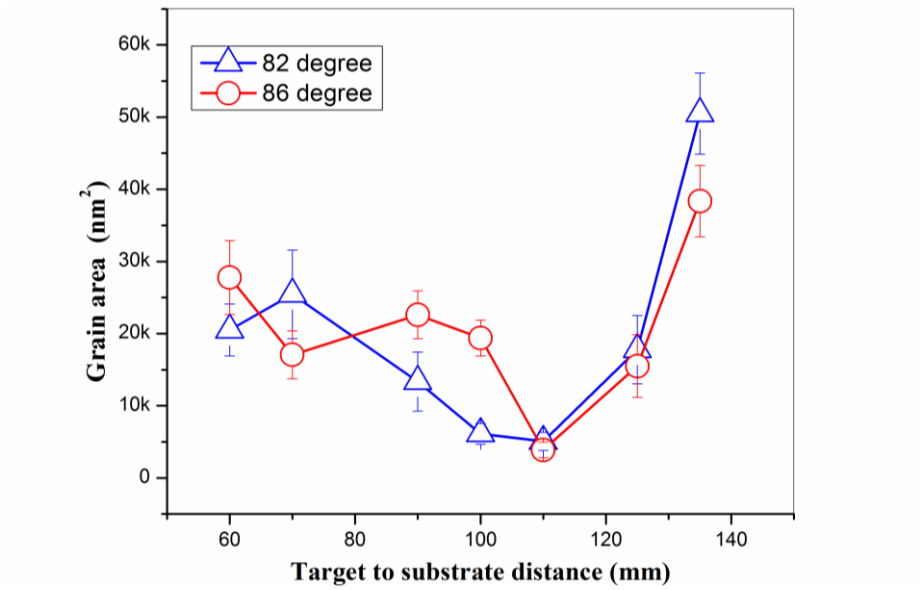

Fig. 4.4: *Plot of grain area as obtained from AFM images vs. target to substrate distance at 82° and 86° angles of deposition.*

4.3.2. Structural Study by GIXRD Measurement

GIXRD measurements were performed on all the HfO_2 samples in order to investigate the structural properties of the samples. Grazing incidence mode was chosen since the samples under study are in thin film form. Fig. 4.5 (a) and (b) show the GIXRD plot of the samples deposited at 86° and 82° angle of deposition. Comparing the GIXRD data with the standard

data (powder diffraction file – international centre for diffraction data, PCPDF), we find that all the films show polycrystalline mono-clinic crystal structure (PCPDF file number: 78-0050). GIXRD peak of all the samples at around 28.4° corresponds to (-11 1) plane of monoclinic crystal structure which along with other peaks suggests that our HfO_2 samples have grown with monoclinic crystal structure. The planes corresponding to the peaks of GIXRD data are also indicated in the respective spectra. For 70 mm DTS, the crystallinity has degraded in going from 86° to 82° angle of deposition. For rest of the samples which are deposited at D_{TS} in the range 90-125 mm, the crystallinity has improved in going from 86° to 82° angle of deposition. With the decrease in deposition angle, shadowing effect decreases and hence the surface diffusion of ad-atoms increases [49] which probably results in improvement in crystallinity. Increase in crystallinity with the decrease in deposition angle was also previously observed by Wang *et al.* [162] for GLAD ZnS thin films deposited by EB evaporation. It is noteworthy that the GIXRD measurement of our earlier published [146]

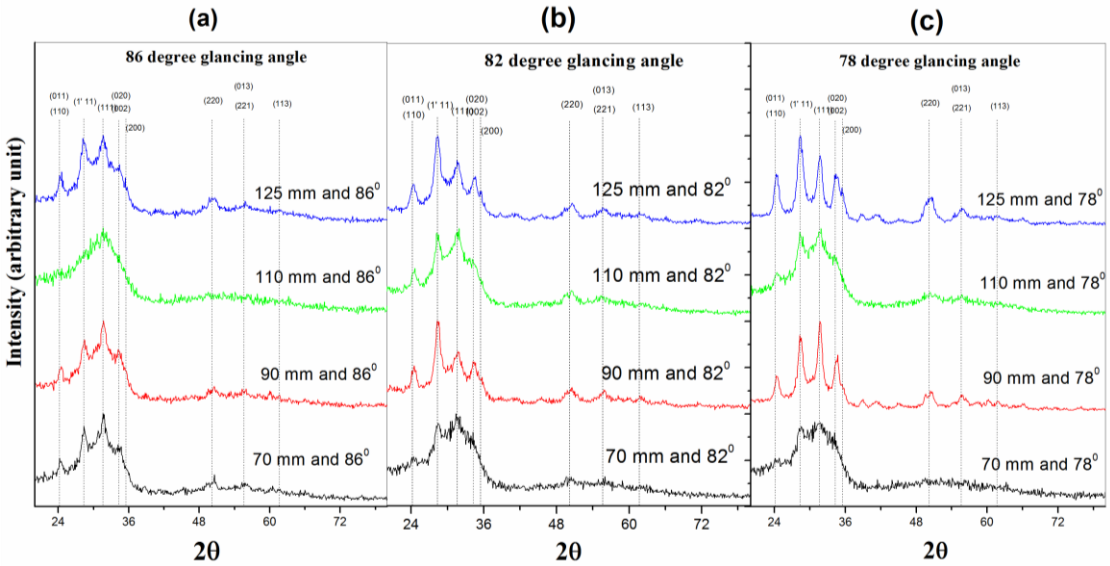

***Fig. 4.5**: GIXRD data of HfO_2 thin films deposited at (a). 86° (b). 82° and (c). 78° glancing angle for various target-substrate distance.*

HfO_2 thin films deposited by magnetron sputtering which was at normal flux incidence angle, exhibited much better crystallinity since normal angle of deposition does not suffer from the

reduction in surface diffusion due to the shadowing effect. However at shorter distance visualizing 70 mm DTS, due to the enhanced substrate temperature, sufficient surface diffusion [154] of ad-atoms may be expected, but larger deposition rates at 82° compared to 86° opposes the ad-atoms to get arranged in crystalline form. That is why at 70 mm D_{TS}, the crystallinity has got degraded in going from 86° to 82° angle of deposition. To verify the above trend of crystallinity with the reduction in deposition angle, the whole set of samples has been deposited at one more glancing angle visualizing 78° angle of deposition and displayed in Fig. 4.5 (c). It shows similar variation of crystallinity for samples deposited at 70 mm and 90–125 mm target to substrate distance.

4.3.3. Optical study by spectroscopic ellipsometry

Ellipsometry is already discussed in section 2.2.5.2 of chapter 2. In present work, optical constants and film thickness of GLAD HfO_2 thin film have been determined using spectroscopic ellipsometry as follows.

Thin film deposition by physical vapour deposition processes is in general characterized by presence of voids in the layers. For present analysis, each sample has been modelled as one surface layer of 0–20 nm thickness having fixed void percentage of 50%, a bulk layer which is a homogeneous mixture of HfO_2 material and variable percentage of air as a void and an interface layer in between the film and the substrate, which is again an homogeneous mixture of HfO_2 material and certain variable amount of void presence. In the inset of Fig. 4.6, the schematic of sample layer structure model as described above is shown for a representative sample. The calculation of the effective dielectric constant of the layers has been done using the Bruggeman Effective Medium Approximation (EMA) [163], while Tauc–Lorentz dispersion model [164] was used as a dispersion relation for the HfO_2 material part in the above layer structure. The Tauc–Lorentz [TL] dispersion model [164] relies upon five parameters A_{TL}, C_L, E_0, E_g, ε (∞) to describe the wavelength dependence of complex

refractive index. Here A_{TL} is the strength of the transition, C_L is the broadening of the transition, E_0 is the peak transition energy, E_g is the band gap, and ε (∞) is the dielectric constant at infinite energy or zero wavelength. Assuming the above sample structure with trial thicknesses, void fractions and parameters of dispersion relation for the different layers as fitting parameters, the measured ellipsometric spectra are fitted by minimizing the Root Mean Squared Error (RMSE) value between the measured and calculated values of the ellipsometric parameters tan(ψ) and cos(Δ) and defined as [165]:

$$RMSE = \left[\frac{1}{(2N-P)} \sum_{i}^{N} \left\{ (\tan\Psi_i^{exp} - \tan\Psi_i^{cal})^2 + (\cos\Delta_i^{exp} - \cos\Delta_i^{cal})^2 \right\} \right]^{\frac{1}{2}} \quad (4.1)$$

where N is the number of data points and P is the number of model parameters. Fig. 4.6 shows the experimental and fitted ellipsometry data for a representative HfO_2 sample deposited at 82° angle and at 110 mm D_{TS}. Fig. 4.7 displays the simulated dispersion curve of the material part of HfO_2 along with Tauc–Lorentz parameters for a representative sample. The error in determining thickness and effective refractive index is expected to be within ± 2 nm and ± 0.01 respectively under the present treatment. It is pertinent to note that we got reasonably good fitting with the above conventional structure model although a more rigorous ellipsometry model suitable for nanostructures may be required.

To check the spatial uniformity of our GLAD HfO_2 films, we performed the ellipsometry measurement at four positions 10 mm apart (top, bottom, left and right) of each sample. The measured spectra of one such representative sample are shown in Fig. 4.8 and the estimated values of thickness and r.i. at above mentioned four positions on this sample are reported in the tabular form in the inset of the same figure. It is clearly seen that there is only a variation of 7 nm in thickness and 0.01 in r.i. over 10 mm distance in lateral direction, whereas in vertical direction the variation is around 27 nm in thickness and 0.03 in r.i. over 10 mm spatial separation. Similar magnitude of variation was observed in all the other

measured samples also which indicates that our GLAD deposited samples are pretty uniform in lateral direction both in terms of thickness and refractive index. To get rid of any ambiguity in thickness and refractive index variation in vertical direction, while comparing different samples, we have consistently taken the measurements at the centre point of each sample. The average thickness of the film deposited at 82° is ~138 nm with a standard deviation of 28 nm accounting the thickness variation for different substrate– target distances and similarly the average thickness of the films deposited at 86° is ~105 nm with a standard deviation of 35 nm.

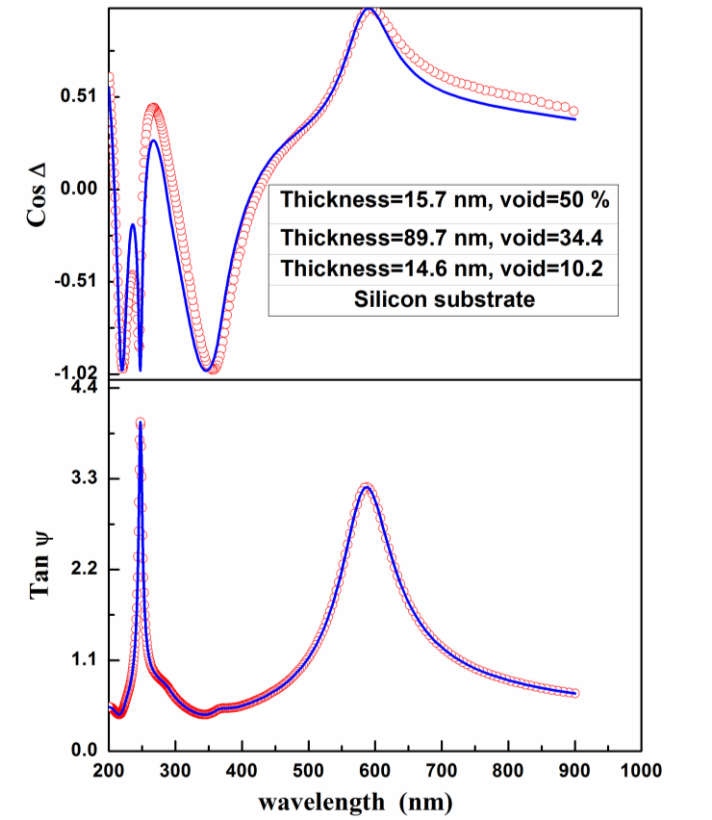

***Fig. 4.6**: Plot of **e**xperimental and best-fit theoretical values of tan (ψ) and cos (Δ) vs. wavelength for a representative HfO_2 film deposited at 82° angle and at 110 mm target-substrate distance.(oooooo: Experimental data; ------: theoretical data). Sample layer structure model used for ellipsometry data analysis is shown in inset.*

The deposition rate was calculated by dividing the estimated thickness (from analysis of spectroscopic ellipsometry data by the above means) by duration of deposition time and is shown in Fig. 4.9. As can be seen from Fig. 4.9, the deposition rate decreases with the

increase in D_{TS} in the range of 70-110 mm for both the set of films due to the decrease in deposition flux density (with increasing D_{TS}). Similar result has also been reported by Jeong *et al.* [155] and Wuhrer *et al.* [156]. However, in going from 110 to 125 mm D_{TS}, the deposition rate has increased rather than decreasing for both the set of films. This is probably due to the fact that at D_{TS} larger than110 mm, the increased sticking coefficient factor dominates the effect of decreased deposition flux density since the sticking coefficient

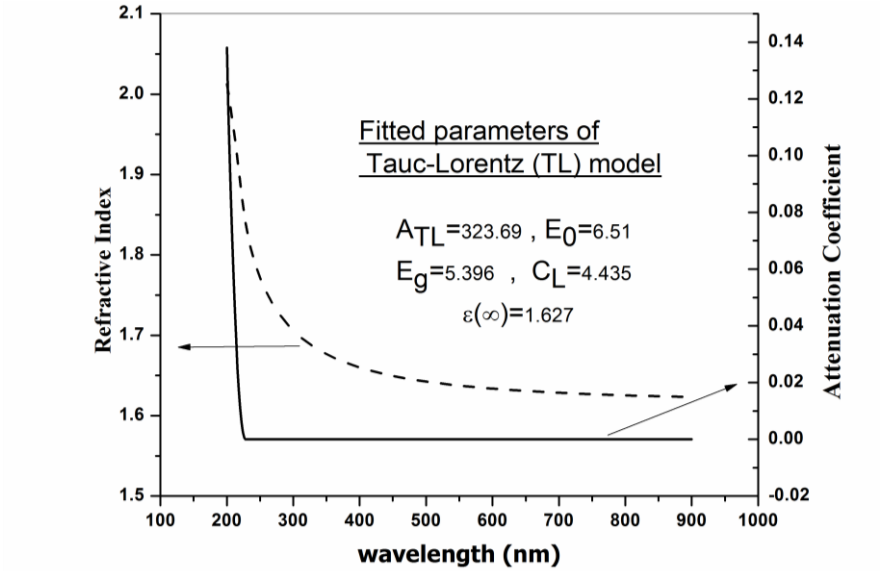

Fig. 4.7*: Dispersion curve of a representative HfO_2 thin film (deposited at 82° and 110 target to substrate distance) as obtained from ellipsometric measurements. Fitted values of Tauc-Lorentz parameters are also given in inset.*

increases with the increase in D_{TS} [166]. Regardless of target to substrate distance, the deposition rate for 82° deposition angle is larger than that of 86° deposition angles which is caused by the larger number of deposition flux faced by the substrate surface at lower deposition angle, as evident from Fig. 4.1.

Fig. 4.10 shows the plot of effective refractive index of the HfO_2 films with the variation of D_{TS} for both set of samples. Comparing Figs. 4.9 and 4.10, we can see that effective refractive index follows almost a similar trend as that of deposition rate. We attribute this trend of refractive index to the fact that higher deposition rate increases the substrate temperature which increases the diffusion rate of ad-atoms and reduces the porosity

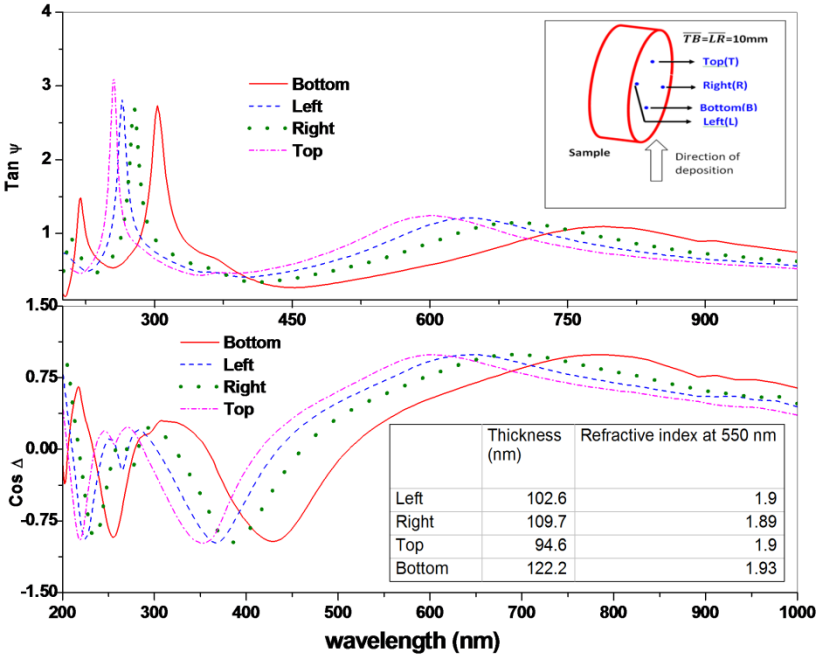

Fig. 4.8: *Measured ellipsometry spectra at four positions 10 mm apart (spots of measurement are shown in the inset) of the HfO_2 sample deposited at 82° angle and 70 mm target to substrate distance (table in inset displays the estimated values of thickness and refractive index at four positions).*

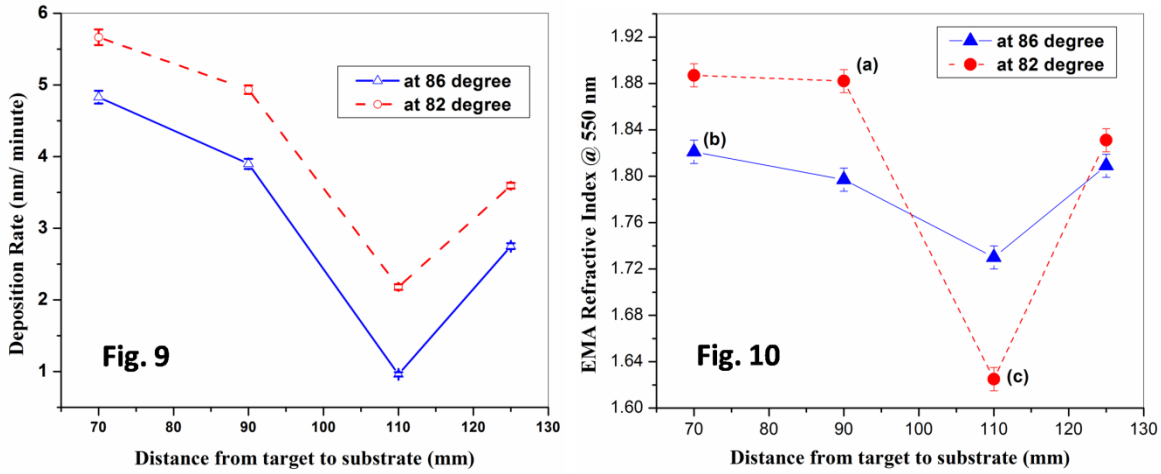

Fig. 4.9*: Variation of estimated deposition rate as a function of distance D_{TS} for 82° and 86° of deposition.* ***Fig. 4.10****: Variation of effective refractive index of the HfO_2 GLAD films obtained from ellipsometeric measurements as a function of D_{TS} for 82° and 86° angle of deposition (the data points marked as 'a', 'b', 'c' in the figure are the ones for which GIXR was carried out in order to verify the trend of density).*

and increases the refractive index. However, at 110 mm D_{TS}, the r.i. at 86° is greater than that at 82°. As shown in Fig. 4.5, the sample deposited at 86° with 110 mm D_{TS} shows very little crystallinity and almost shows amorphous like structure. The deposition rate, KE of the ad-

atoms, collimation of the deposition flux etc., might have promoted this high index amorphous like structure and thus the films deposited at 82° and 110 mm D_{TS} shows lowest r.i. compared to all other films.

4.3.4. Determination of film density by GIXR measurements

GIXR measurements were performed selectively on three samples; visualizing on the samples (a) deposited at 82° deposition angle at 90 mm target-substrate distance (b) deposited at 86° deposition angle at 70 mm target-substrate distance (c) deposited at 82° deposition angle at 110 mm target-substrate distance in order to verify the trend in effective refractive index obtained from ellipsometry measurement and are indicated in Fig. 4.10. Since the

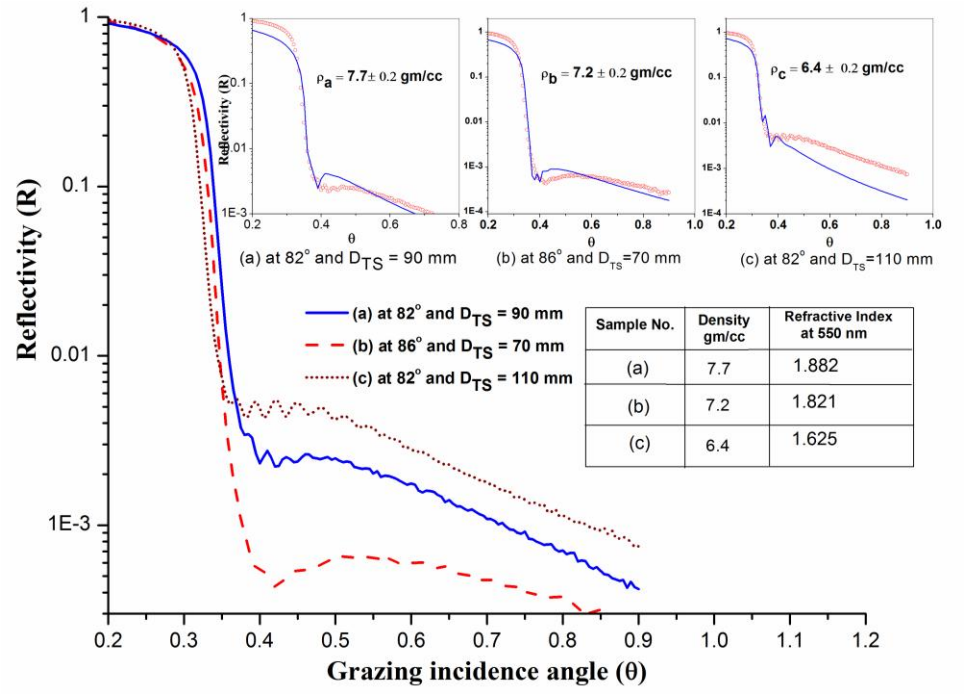

Sample No.	Density gm/cc	Refractive Index at 550 nm
(a)	7.7	1.882
(b)	7.2	1.821
(c)	6.4	1.625

Fig. 4.11*: GIXR data of three GLAD HfO_2 thin films; namely the film (a) deposited at 82° deposition angle and at 90 mm target-substrate distance (b) deposited at 86° deposition angle and at 70 mm target-substrate distance (c) deposited at 82° deposition angle and at 110 mm target-substrate distance.*

thickness (~100 nm as obtained from ellipsometry measurement) and surface roughness (~ 10 nm as obtained from AFM measurement) are pretty high, the Kiessig [167] oscillations do not appear in XRR data as shown in Fig. 4.11 and thickness of the samples cannot be

estimated from these data. Only density of the films was estimated by fitting the XRR data around critical angle. The experimental and simulated X-ray reflectivity plots are shown in Fig. 4.11. The calculated densities from XRR data and refractive index as calculated from ellipsometry of these samples are shown in tabular form in the inset of Fig. 4.11. As can be seen, the trend of the estimated densities is in the similar order with the trend of EMA refractive index as labeled by 'a' 'b' and 'c' in the figure.

4.4. Summary

HfO_2 thin films have been deposited keeping substrate at glancing angle with the deposition flux by RF magnetron sputtering deposition technique at two different angles of depositions 82° and at 86° and at four different targets to substrate distances visualizing 70 mm, 90 mm, 110 mm and 125 mm. From the morphological, optical and structural studies of the above described samples following observations could be made.

(i) At optimum distance D_{TS} = 110 mm and at 82° angle of deposition the film exhibits prominent nanostructures as observed from AFM image.

(ii) At lower D_{TS} (70-90 mm) the grains, obtained by AFM imaging, are elliptical in shape and as the D_{TS} increases the surface grains are circular in shape. The fact has been explained in light of the variation in ad atom kinetic energy.

(iii) The grain area has initially decreased with increase in D_{TS} in the range 70 to 110 mm and grain area has increased in going from 110 mm to 125 mm D_{TS} which is in accordance with the trend of deposition rate. The competition between deposition flux density and the sticking coefficient has lead to minimum deposition rate and hence minimum grain area at D_{TS}=110 mm. Regardless of target to substrate distance, the deposition rate for 82° deposition angle is larger than that of 86° deposition angle which is due to the fact that at lower deposition angle the substrate surface faces larger number of deposition flux.

(iv) The effective refractive index follows almost similar trend as that of deposition rate except at 110 mm D_{TS} for which the film deposited at 82° exhibits lower r.i. compared to that at 86°. At 86° angle and 110 mm D_{TS}, the formation of amorphous crystallographic structure is responsible for relatively higher index compared to that at 82°.

(v) Crystallographic structural study of the films shows that all the films have formed in polycrystalline monoclinic crystal structure. At lower D_{TS}, the crystallinity has improved with increase in deposition angle due to the reduction in deposition rate which helps in organizing the atoms in more crystalline form. However at higher D_{TS} (> 90 mm), the crystallinity has degraded with increase in deposition angle which is due to the lesser diffusion due to the enhanced shadowing effect at higher deposition angle.

Overall, this can be inferred from this study that the optimum value of target to substrate distance lies in the range of 100-120 mm for depositing low refractive index HfO_2 thin film under glancing angle deposition by RF magnetron sputtering technique.

CHAPTER 5: GLANCING ANGLE DEPOSITION OF ZrO_2 THIN FILMS

This chapter is devoted to glancing angle deposition of ZrO_2 thin films deposited by magnetron sputtering and EB evaporation. This chapter has been described in two parts as following.

5.1. Glancing Angle Deposition of ZrO_2 Thin Films by Magnetron Sputtering

5.1.1. Introduction

As discussed in earlier chapters, glancing angle deposition of thin films has been an attractive field for researchers and technologists in the recent years due to their fascinating physical and chemical properties. By employing the variation in deposition parameters such as substrate rotation (ω), angle and rate of deposition, and substrate temperature, different microstructures resulting in unique physical and chemical properties can be achieved. The porous microstructure is responsible for unique properties which are exploited for various applications such as energy harvesting and storage devices, fuel cell and hydrogen storage, sensors, optical devices, wetting and micro fluidics, biomaterial and biosensors [1, 3, 4]. Deposition of GLAD thin films can be carried out by various techniques such as electron beam (EB) and thermal evaporation, pulsed laser deposition, plasma enhanced chemical vapor deposition and magnetron sputtering techniques [4]. Out of these techniques, EB and thermal evaporation are known to produce the most porous micro structures due to the directional movement, and low energy and scattering of ad-atoms. Other techniques, especially magnetron sputtering being an energetic process produce merged porous

microstructure rather than separate nano rods for glancing angles ≥ 80º. Among the various parameters, the deposition method and the parameter, ω have great influence over columnar morphology and hence various properties of GLAD films. Therefore studying GLAD films deposited by different coating techniques at different ω values assumes importance.

ZrO_2 exhibits excellent optical, mechanical, electrical, chemical and thermal properties which enable it to become an important material for applications in various fields [168]. Various properties of ZrO_2 thin film prepared by different deposition processes under normal deposition have been investigated by many researchers [169-175]. From optical applications point of view, ZrO_2 has high refractive index, high laser induced damage threshold and good optical transparency in near UV to mid IR wavelength region [176-179]. GLAD ZrO_2 thin films fabricated under varying deposition parameters such as deposition angle and substrate rotation have also been explored by researchers to probe their properties. Wang, *et al*. had investigated the influence of angle of deposition and substrate rotation on optical and columnar micro-structural properties, surface morphology and birefringence in refractive index of EB evaporated ZrO_2 thin films [48, 49]. Levichkova, *et al.* have discussed the influence of angle of deposition on DC electrical conductivity, micro-hardness, and optical anisotropy in EB evaporated GLAD ZrO_2 thin films [180]. Park, *et al.* have realized a wideband circular polarization reflector using GLAD ZrO_2 and other oxide thin films deposited by EB evaporation [143]. Hdgkinson, *et al.* have demonstrated and measured biaxial anisotropy in refractive index of GLAD ZrO_2 thin films at stationary substrate by EB evaporation [181]. However, most of the work carried out on GLAD ZrO_2 thin films is on EB deposited films. As mentioned earlier, films deposited by sputtering show different micro-structural properties resulting specially from lower porosity at a given deposition angle in comparison to EB coated films. Therefore study of such thin films deposited by magnetron sputtering is of great importance. In the present work, we report the study of optical,

morphological and micro-structural, and mechanical (residual stresses) properties of GLAD ZrO_2 thin films deposited by RF magnetron sputtering with varying, ω. All the parameters obtained from different characterizations of GLAD films have been compared with that of normally deposited (ND) ZrO_2 thin film.

5.1.2. Experimental Details

ZrO_2 thin films have been deposited by RF magnetron sputtering in ND and GLAD configuration. GLAD films have been deposited at glancing angle (82°) on Si (111) substrate for different substrate rotation values, ω = 0.5, 1.0, 1.5, 3.0 and 4.0 rpm. Thin film samples are designated as S-1, S-2, S-3, S-4 and S-5 respectively. ND ZrO_2 film has been designated as S-6. GLAD sputtering set-up utilizes a DC stepper motor for substrate rotation and is shown in Fig. 2.5 (chapter 2). Substrate to target distance was kept at 70 mm to get stable plasma and good deposition rate. Base pressure of $1.5x10^{-5}$ mbar was achieved using turbo-molecular pump backed by rotary pump in order to reduce the contaminations in films. Deposition pressure was maintained at 3 $x10^{-3}$ mbar inside the vacuum chamber with sputtering gas (Argon) flow rate of 19 SCCM controlled by mass flow controller. Sputtering was carried out at RF power of 250 Watts with a target size of 3 inches giving a deposition rate ~ 2 Å/s for ND film. Actual deposition rate for GLAD films was reduced radically due to low sticking coefficient. MDC make quartz crystal thickness monitor was used to monitor and control the rate of deposition and film thickness. ZrO_2 target was pre-sputtered for 300 seconds to remove any possible contamination from its surface. Crystal structure of films was examined by recording GIXRD pattern. Morphological measurements of the films were carried out by AFM system in tapping mode with a super sharp DLC tip grown on silicon cantilever having radius of curvature ~1 nm and spring constant of 8.1 N/m. In order to explore microstructure and determine thickness of the films, cross-sectional morphology was recorded by FESEM system. Optical characterization of GLAD ZrO_2 thin films has been

carried out by rotating polarizer type spectroscopic ellipsometer. Ellipsometric measurements of the films were performed in the wavelength range of 200-800 nm at 70° angle of incidence of light beam. To derive residual stresses, change in the curvatures of the Si substrates was measured by recording the shapes of Si substrates before and after the deposition of thin films using laser Fizeau interferometer.

5.1.3. Results and discussion

5.1.3.1. Structural Properties

X-ray diffraction spectra recorded in grazing incidence configuration are shown in Fig. 5.1 for all the ZrO_2 films. Major X-ray diffraction Peaks for GLAD ZrO_2 films were observed at 2θ = 24°, 28.1°, 30.2°, 31.5°, 34°, 34.4, 44.8 and assigned to the crystalline planes of monoclinic and tetragonal phase with directions m (110), m (-111), t (101), m (111), m (002), m (020) and m (112) respectively. The plane's directions are in agreement with the published results [182-184]. GLAD films show a preferential growth for crystalline plane of monoclinic phase in m (110) direction. Generally, the most intense XRD peak for ND ZrO_2 films corresponds to m (-111) direction ($2\theta \sim 28.2°$). It is observed from Fig. 5.1 that this peak is nearly absent for GLAD films. Since different crystal planes grow at different rates, the vertical growth (perpendicular to substrate) rate is sensitive to the orientation of the crystal. The crystallites having orientation with the greatest vertical growth are most likely to grow and preferential growth in that direction of crystallographic planes occurs [3]. In GLAD films, the ad-atom strikes substrate surface at glancing angle and leads to the preferential growth in m (110) direction perpendicular to substrate planes. Another important observation is the presence of tetragonal phase positioned at 30.2° with directions (101), while it is not common to get tetragonal phase of ZrO_2 at room temperature. Tetragonal peak for GLAD films was fitted with Lorentzian curve. The obtained FWHM ($B_{1/2}$) is 0.63° ± 0.01°. The crystallite

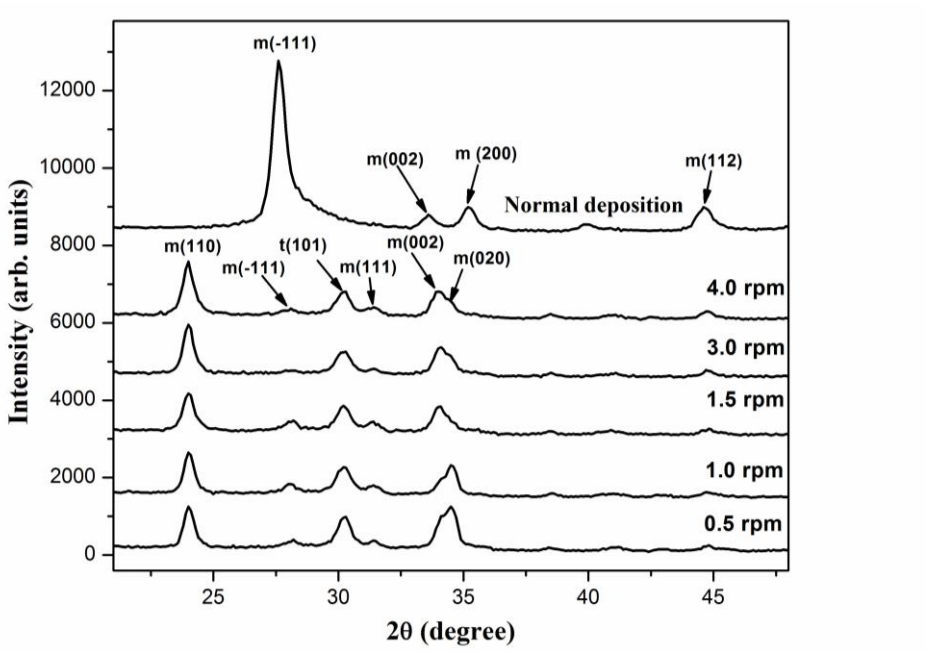

Fig. 5.1: *GIXRD spectra of GLAD and ND ZrO_2 thin films.*

size *(t)* was calculated to be 13.6 ± 0.2 nm using Scherrer equation [184] : $t = 0.94\lambda/(B_{1/2}\cos\theta)$. This clearly indicates that the tetragonal ZrO_2 is in nanocrystalline form. At room temperature, monoclinic is the most stable phase of ZrO_2 due to thermo dynamic conditions [185] and tetragonal is high temperature phase which generally occurs at temperature $\geq$ 600°. Researchers have reported that high temperature tetragonal phase of ZrO_2 could also be obtained at room temperature without adding any stabilizing doping by two methods such as high pressures [186] and fabricating material with very fine crystal grains [187, 188]. The critical diameter of tetragonal phase crystallite to stabilize the tetragonal at room temperature is ≤ 30 nm [187, 188]. Since in present case, crystallite size is ~13.6 nm, the presence of tetragonal phase is attributed to fine tetragonal crystallites. The crystallite size effect is explained in terms of the lower surface energy of the tetragonal phase (770 erg/cm^2) compared to that of rather stable monoclinic phase (1130 erg/cm^2), which compensates for the chemical free energy [187]. FWHM of the dominant monoclinic peak at 24º is obtained to be ~ 0.45 degree while the crystallite size is in the range 18.5 to 19.5 nm. For ND film (S-6), XRD peaks were observed at 2θ = 27.6º, 33.7 º, 35.2 º and 44.6 º

corresponding to the monoclinic phase with directions m (-111), m (002), m (200), and m (112) respectively. The peaks shift to lower 2θ value, which may be the result of compressive residual stress. ND film depicts preferential growth in m (-111) directions. For such film, energetic ad-atoms strike on substrate vertically and cause the greatest vertical growth of m (-111) reflection planes. It can be noted that the peak at m (-111) is asymmetric and extended towards higher 2θ values. This may be due to the merging of small peaks of t (101) and m (111) with intense peak of m (-111). It can hence be inferred that the ND and GLAD films show different preferential crystal growth directions with the presence of tetragonal phase.

5.1.3.2. Surface and cross-sectional morphological properties

Surface morphology of ZrO_2 films was investigated by AFM in tapping mode using DLC tip. DLC tip offers high resistance to abrasion and changes in its geometry caused by measurements due to its high hardness, adding accuracy and consistency to the measurement. For quantitative analysis of surfaces of such films, one dimensional height-height correlation function (HHCF) has been computed from AFM measurements using following formulations [131, 189]:

$$H(r_x) = \frac{1}{N(N-m)} \sum_{l=1}^{N} \sum_{n=1}^{N-m} (z_{n+m,l} - z_{n,l})^2 \tag{5.1}$$

Here m = $r_x/\Delta x$. The HHCF function thus can be evaluated in a discrete set of r_x value separated by sampling interval Δx. In the above formulation, scan data points have been taken equal in x and y direction. HHCF prominently describes the grain structure in thin films. To get the useful surface parameters, we have fitted the measured function with calculated one for self affine surfaces using following Gaussian function [190]:

$$H(r) = 2\sigma^2 \left[1 - \exp(-(r/\xi)^{2\alpha})\right] \tag{5.2}$$

Where σ is RMS roughness or often termed as interfacial width and describes the fluctuations of heights around the mean plane. Exponent *'α'* is "Herst" or roughness exponent. It describes grain morphology and depicts the wiggliness of the local slope on the surface. Higher value of α (≤ 1) implies less high frequency contribution to line edge roughness [191]

***Table 5.1**: Morphological parameters and film thickness estimated from AFM and FESEM measurements.*

Sample name	AFM RMS roughness (nm)	Correlation length (ξ) (nm)	Roughness exponent (α)	Film thickness from FESEM (nm)
S-1	4.6 ± 0.1	21.8 ± 0.6	0.86 ± 0.06	160 ± 1
S-2	4.4 ± 0.1	21.5 ± 0.4	0.94 ± 0.05	129 ± 1
S-3	5.0 ± 0.1	21.3 ± 0.5	0.93 ± 0.06	128 ± 1
S-4	5.1 ± 0.1	20.4 ± 0.4	0.97 ± 0.03	136 ± 1
S-5	5.0 ± 0.1	18.9 ± 0.5	0.94 ± 0.05	140 ± 1
S-6	1.0 ± 0.1	16.5 ± 0.05	0.90 ± 0.01	176 ± 1

or smoother line edge. The parameter, ξ is lateral correlation length and it describes the largest distance in which the height is still correlated over the surface. Fig. 5.2 (a) shows the measured HHCF functions for all the ZrO_2 films. Higher counts of HHCF stand for higher surface roughness. It can be noted that for all the GLAD films, counts of HHCF are close to each other whereas for ND film, HHCF value is relatively lower. Fig. 5.2 (b) shows the measured and fitted HHCF curves for a representative of ZrO_2 films, S-1. The parameters derived from the fitting are listed in Table 5.1. RMS roughness (σ) for GLAD ZrO_2 films varies between 4.4 and 5.1 nm and there is no significant influence of parameter, ω on roughness. The value of σ for ND film is 1 nm which is 4 to 5 times lower than that of GLAD films. Such behavior of roughness for GLAD and ND films can be explained in terms of re-emission of ad-atoms and atomic shadowing [137, 189] which the two main factors are

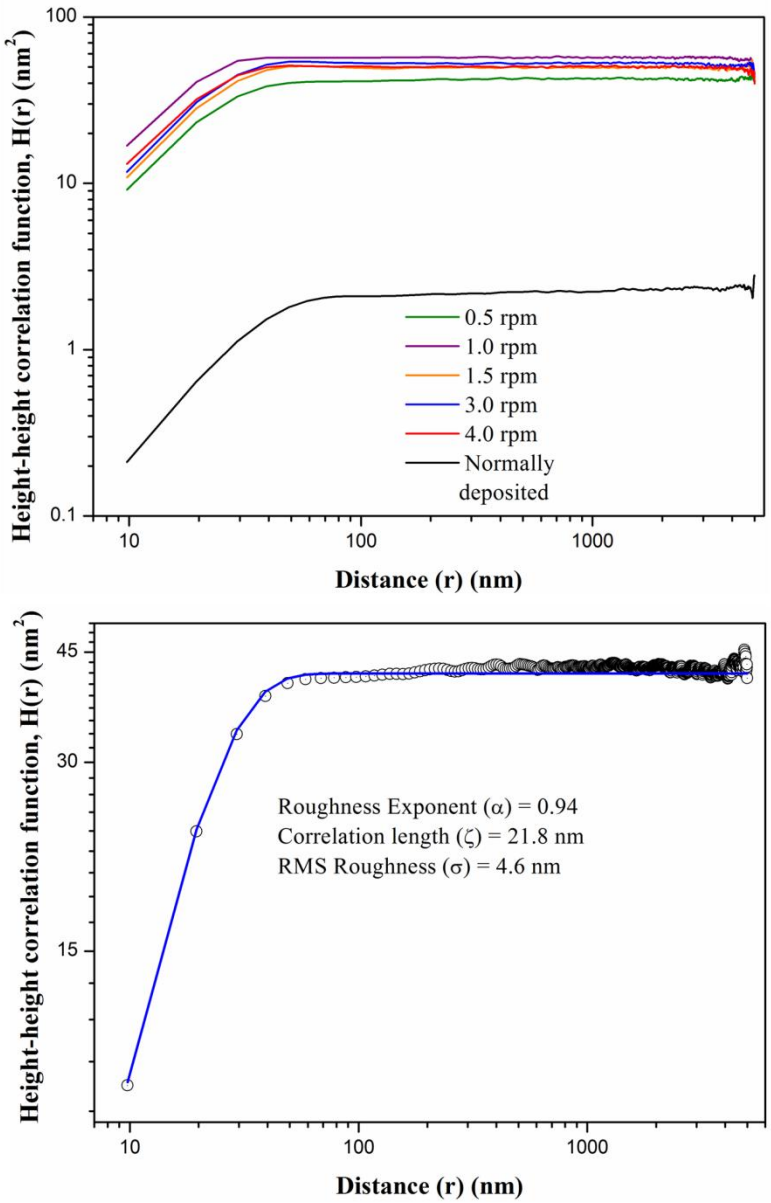

Fig. 5.2 *(a): Measured height-height correlation function for all the ZrO_2 thin films. (b). measured and fitted height-height correlation function for film, S-1 (GLAD, ω=0.5 rpm).*

contributing to the surface roughness of thin films. The sticking coefficient of ad-atoms for the ND film in the present case is highest which is attributed to lower re-emission of ad-atoms leading to lower smoothing effect [137, 189]. Roughening effects due to atomic shadowing are negligible for ND film. Collectively, both these effects do not contribute to the roughening significantly and smooth surface grows. On the other hand, atomic shadowing for GLAD films is prominent giving rise to high roughening effects. However, smoothing effect also increases due to the increase in re-emission caused by decrease in sticking coefficient,

the combined effect leads to the effective roughening of the surfaces of GLAD films. Variation of correlation length, ξ which is the measure of surface grain size, with respect to substrate rotation, ω, is shown in Fig. 5.3. Correlation length, ξ decreases gradually with the increase in ω leading to the inference that average grain size decreases with ω. AFM images of thin films S-1, S-3, and S-4 (as shown in Fig. 5.4) also corroborate the decrease in grain size with the increase in ω. Fig. 5.4, which includes the zoomed 3D images, depicts a transition from non-circular grains having irregular shape to circular grains. AFM surface morphologies also show that the void fraction increases with the increase in ω for GLAD films. It can be inferred that nano columns get finer and circular with the increase in ω. The value of roughness exponent α is listed in Table 5.1 and it remains almost unchanged with ω except for sample, S-1 (GLAD, 0.5 rpm). Value of α for S-1 is 0.86, which is the lowest among all the GLAD films. It signifies the relatively wigglier surface for S-1 (grains possess sharp edges). The wiggly surface for S-1 and S-6 (ND) can also be seen from Fig. 5.4. AFM image of GLAD films other than S-1 depict a smooth variation at grain boundaries. Higher grain density present in the films S-1 and S-6 is responsible for higher wiggly surface (lower α value). FESEM cross-sectional morphology of all the ZrO_2 films is shown in Fig. 5.5. It can be seen that GLAD films depict a porous erect columnar structure which is caused by ballistic atomic shadowing during the growth of the films. However columns are not distinct and are merged due to the energetic deposition process. Thickness of the films has also been measured from cross-sectional morphological images and is listed in Table 5.1.

5.1.3.3. Optical properties

Optical properties of ZrO_2 thin films have been estimated from ellipsometric measurements. Principle of ellipsometry is already discussed in section 2.2.5.2 of chapter 2.

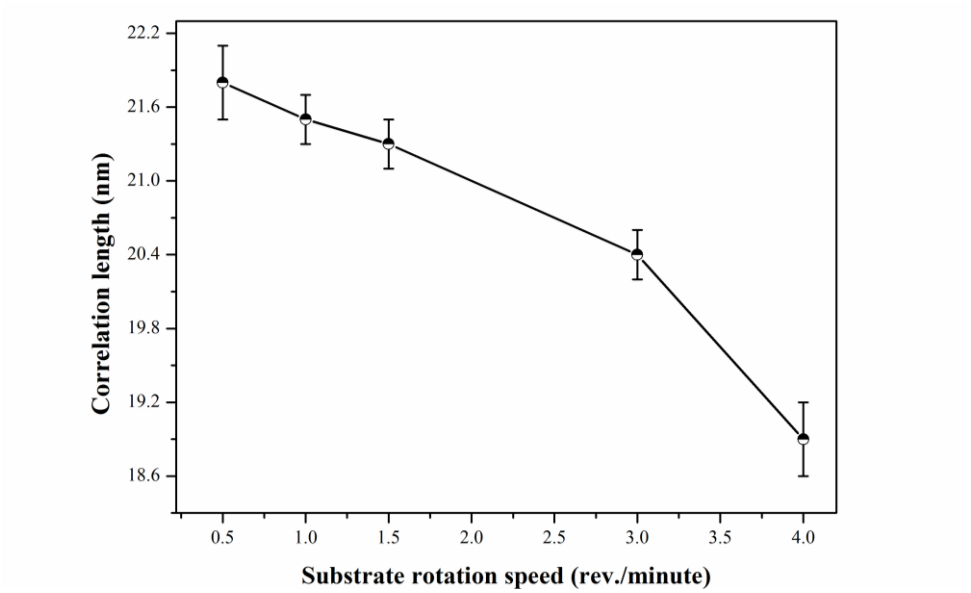

Fig. 5.3: *Plot of variation of correlation length for GLAD ZrO_2 thin films with substrate rotation (ω).*

In rotating polarizer type ellipsometry, the time dependent signal, *I(t)* at each wavelength is described by the general formula [192] :

$$I(t) = I_0(1 + \alpha\cos(2\eta t) + \beta\sin(2\eta t)) \tag{5.3}$$

Where η is the rotational frequency of the polarizer and α and β are the normalized Fourier coefficients with which the ellipsometric parameters ψ and Δ *(already discussed in chapter 2)* are related through following expression:

$$\alpha = \frac{\tan^2\psi - \tan^2 A}{\tan^2\psi + \tan^2 A} \quad , \quad \beta = \frac{2\tan\psi\cos\Delta\tan A}{\tan^2\psi + \tan^2 A} \tag{5.4}$$

Here A is the angle of analyzer. Even though ψ and Δ are physically more meaningful ellipsometric parameters, the more directly obtained ellipsometric parameters α and β (at analyser angle of 45°) have been used for present analysis.

It is well known that thin films deposited by physical vapor deposition contain voids. The fraction of voids in the films depends on deposition technique and process parameters.

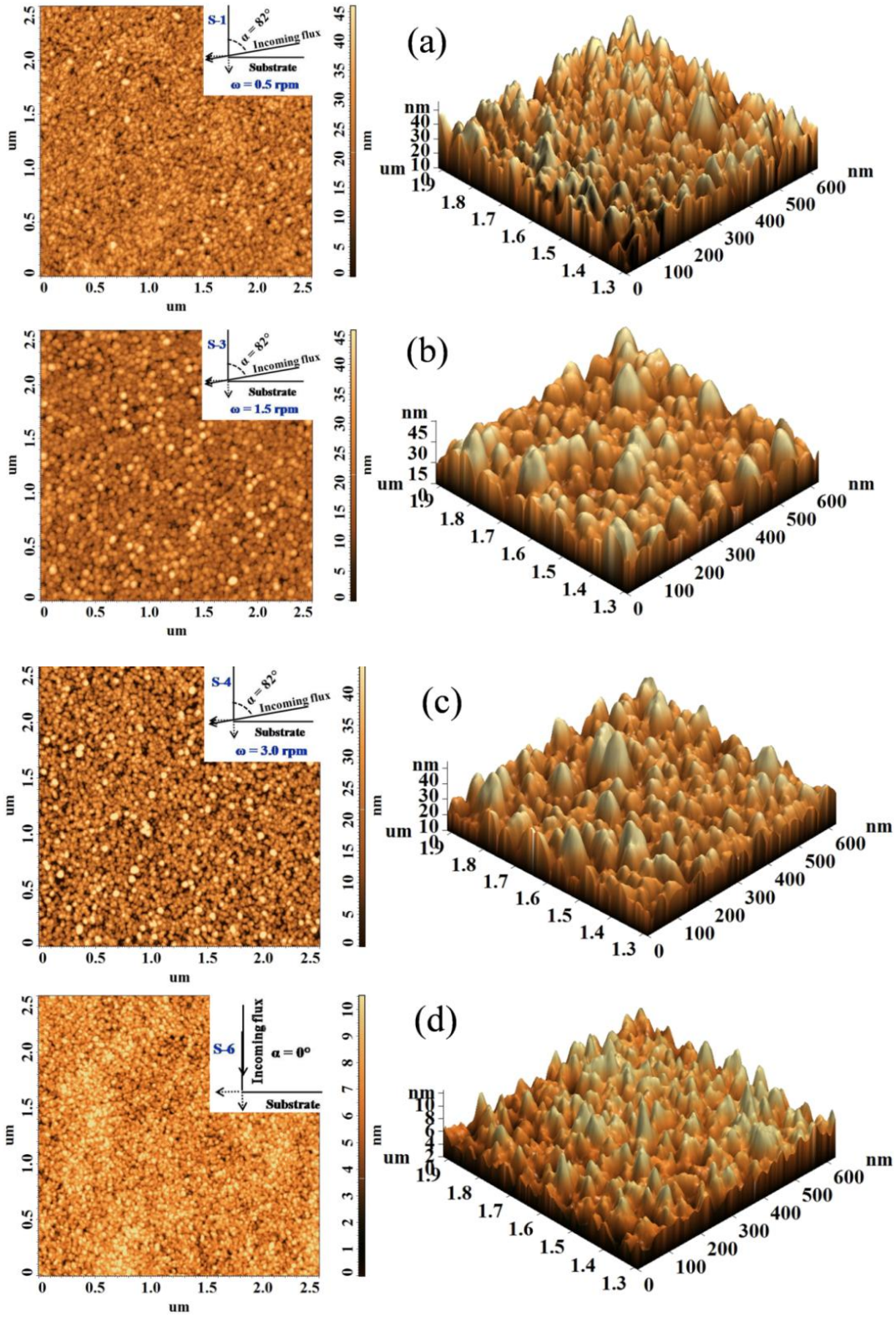

Fig. 5.4 *(a, b, c, d): 2-D AFM images of GLAD and ND ZrO_2 thin film. Zoomed 3-D morphology has also been shown in the right of* ***Fig. 5.4*** *to highlight grain geometry.*

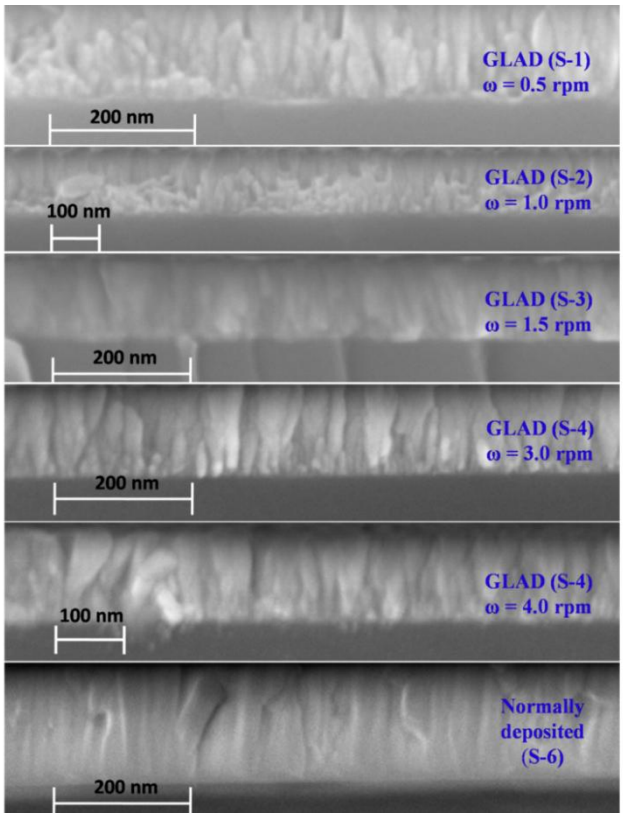

Fig. 5.5: *FESEM cross-sectional images of GLAD and ND ZrO_2 thin films.*

Magnetron sputtering is an energetic deposition technique and the films grown by it have dense microstructure having low fraction of voids [193]. However, in the present study of sputtered ZrO_2 films grown in GLAD configuration, the void fraction is significant due to atomic shadowing effects for ad-atoms. Considering the porous nature of such films, each film has been modeled as two layers of ZrO_2 consisting different void and material component fractions. Both the layers have been assumed to follow the same dispersion relation for refractive index. Top layer (surface) being in direct contact with air is more porous. The thickness of top layer in the model ranges from 17-22 nm. The underlying layer is modeled as a bulk layer having homogeneous mixture of ZrO_2 and voids, where different samples have different fractions of material to void ratios. The model layer structure for

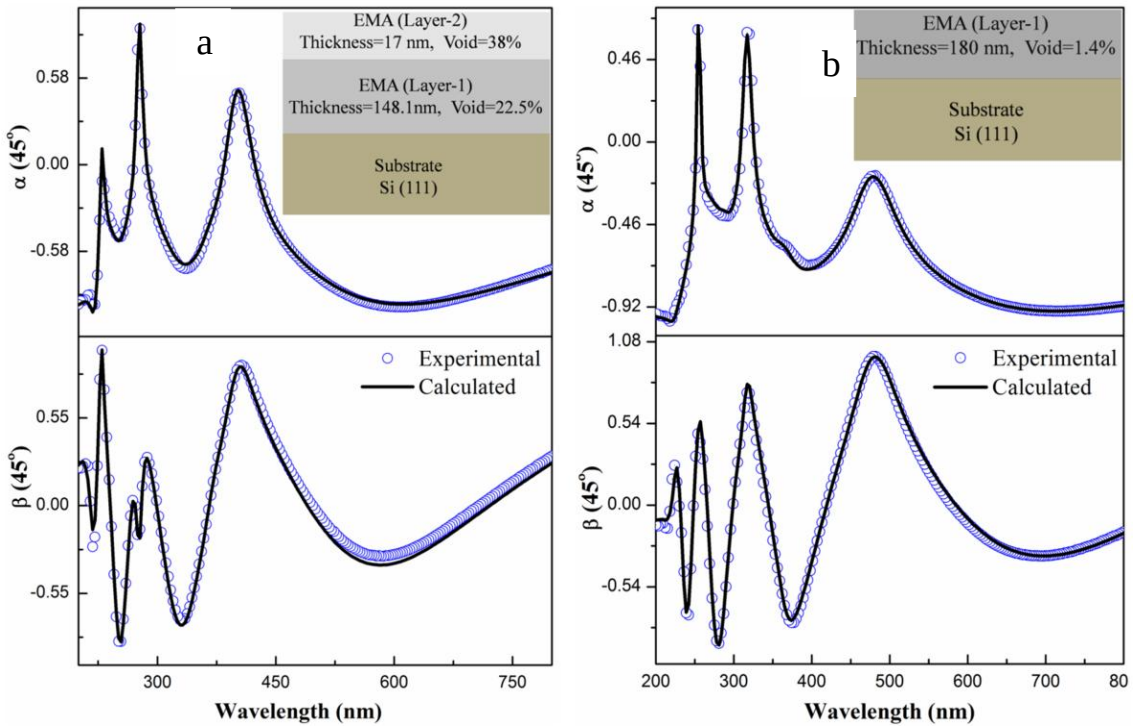

Fig. 5.6 *(a), (b): Measured and fitted ellipsometric spectra of parameters, α (45°) and β (45°) for film, S-1(GLAD, ω=0.5 rpm) and S-6 (ND). In inset, model layer structures are shown.*

representative ZrO_2 thin films, S-1 and S-6, are shown in inset of Fig. 5.6 (a) and (b) respectively. The porosity in the bulk layer is small even in GLAD configuration [194] for films deposited by sputtering in contrast to EB deposited films at the same angle. Hence, such films have been assumed optically isotropic for ellipsometric modeling. The effective refractive index has been determined using Bruggman effective medium approximation [195]. Cody-Lorentz dispersion model [196] which is an improved version of Tauc-Lorentz dispersion formulation [164] was used for ZrO_2 material component in all the layer structures.

Taking initial trial values of layer thicknesses, void fraction and model fitting parameters, the measured ellipsometric spectra were fitted by minimizing root mean squared value (*RMSE*) between measured and theoretically generated ellipsometric parameters α (45°) and β (45°) as follows [194]:

$$RMSE = \left[\{1/(2N-P)\}\sum_i^N \{(\alpha_i^{\exp}(45°) - \alpha_i^{cal}(45°))^2 + (\beta_i^{\exp}(45°) - \beta_i^{cal}(45°))^2\}\right]^{1/2} \quad (5.5)$$

Where N is the number of data points and P is the number of fitting parameters. In Fig. 5.6 (a) and (b), experimental and fitted curves of α (45º) and β (45º) are shown. Theoretical curves fit very well with measured curves, which justifies the selection of Cody-Lorentz dispersion relation and correctness of chosen layer structures. All the films except S-6 (ND) have been modeled using 2-layer structure. The film, S-6 has a dense micro-structure with a low void fraction and hence the ellipsometric curves fits very well with only a single layer structure. Derived film thickness, refractive index of each layer, effective refractive index and extinction coefficient from ellipsometric analysis for ZrO_2 thin films are listed in Table 5.2. It can be noted that thickness values obtained from ellipsometric analysis are consistent with the values obtained from FESEM measurements. This also justifies the methodology used for analysis of ellipsometric measurements. Dispersive values of effective refractive index of all the ZrO_2 films are plotted in Fig. 5.7 (a). The film, S-6 (ND) shows greater refractive index (2.178) compared to the GLAD films (1.901-2.011). The similar values of refractive index for magnetron sputtered normally deposited ZrO_2 thin films have also been reported in literature [197-199]. The lowering in refractive index of GLAD films is the attribute of prominent atomic shadowing effects which introduces porosity in the films. As can be noted from Table 5.2, the least difference of refractive index between GLAD and ND film is 0.167 which is smaller compared to GLAD films deposited by EB evaporation under similar deposition angle configuration [189]. This can be understood in terms of ad-atom energy and of the voids. These results in lower porosity in sputtered GLAD films compared to thermal evaporated GLAD films deposited at the same angle. Effective rate of deposition was calculated from measured post deposition film thickness and deposition time. The rate of deposition for ND film is 2.06 Å/s whereas for GLAD films, it lies between 0.64 and 0.74 Å/s as listed in Table 5.2. Such abrupt reduction in deposition rate for GLAD films is also

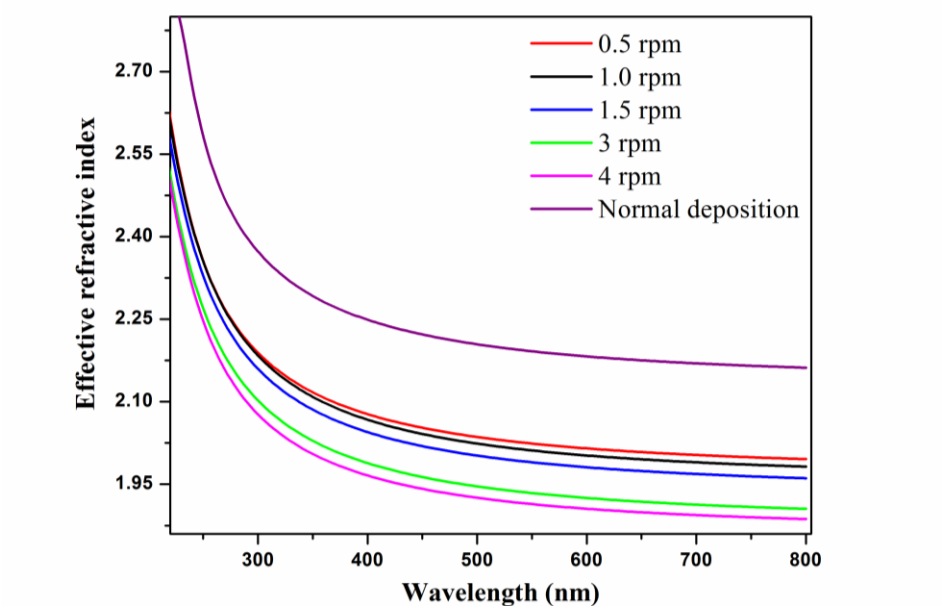

Fig. 5.7 *(a): Dispersive curves of effective refractive index of all the ZrO_2.*

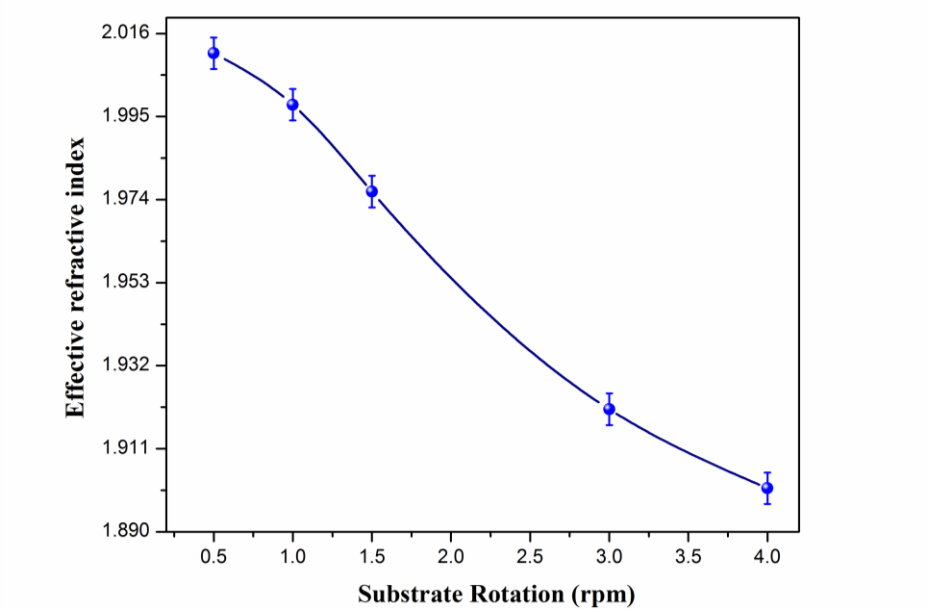

Fig. 5.7 *(b): Variation of effective refractive index with substrate rotation (ω) for GLAD ZrO_2 films.*

supported by earlier reported results [3, 4]. The lower deposition rate for GLAD films is attributed to the reduction in sticking coefficient due to high incident angle of ad-atoms on the substrate [189]. Deposition rate for GLAD films increases monotonically with the increase in ω (0.50 - 4.0 rpm), suggesting that column length increases with ω. Hence the columns get finer with the increase in ω. Consequently, void fraction increases with increasing ω.

***Table 5.2**: Optical constants and layer structure of GLAD and ND ZrO_2 thin films derived from ellipsometric measurements.*

Sample name	Substrate rotation speed (rpm)	(Layer-1) Refractive index	(Layer-2) Refractive index	(Layer-1) Thickness (nm)	(Layer-2) Thickness (nm)	Total Thickness (nm)	Effective Refractive index @ 632 nm	Extinction coefficient @ 260 nm	Effective rate of deposition (Å/s)
S-1	0.5	2.034	1.807	148.1	17.0	165.1	2.011	$1.0x10^{-3}$	0.64
S-2	1.0	2.032	1.815	108.0	20.6	128.6	1.998	$1.8x10^{-3}$	0.67
S-3	1.5	2.014	1.791	108.0	22.0	130.0	1.976	$2.6x10^{-3}$	0.67
S-4	3	1.951	1.722	118.0	18.4	136.4	1.921	$2x10^{-3}$	0.71
S-5	4	1.944	1.659	120.9	21.3	142.2	1.901	$2.7x10^{-3}$	0.74
S-6	Normal deposition	2.178	nil	180.0	nil	180.0	2.178	$3.3x10^{-4}$	2.06

This is also corroborated by AFM morphology. There are earlier reports on effect of parameter, ω on columnar microstructure but most of them are for EB evaporation [200]. Fig. 5.7 (b) shows the variation of effective refractive index of GLAD ZrO_2 films with parameter, ω. Refractive index decreases from 2.011 to 1.901 with the increase in ω. This decrease again can be attributed to the change in columnar micro-structure with the increase in ω. AFM micro-graphs show an increase in voids with increasing ω, which supports the trend of reduction in effective refractive index. Index varies relatively slower for higher rotation speeds (≥ 3 rpm) implying that the evolution of columnar microstructure gets saturated for higher values of ω. It can also be noted from Table 5.2 that extinction coefficient (k@260nm) for GLAD ZrO_2 films (~10^{-3}) is one order higher than that of ND film (~10^{-4}). Higher k values for GLAD films can be the result of higher scattering losses in UV region due to high surface roughness. High contribution of light scattering towards k value for GLAD films has been reported elsewhere [77, 138].

5.1.3.4. Residual stress analysis

Residual stress in thin films can be measured by measuring the surface shape deformation of the substrate which takes place after the coating. The radii of curvatures of the substrate are measured before and after the coating to determine the change in curvature due to the deposition. If R_1 and R_2 are radii of the substrate curvature before and after film deposition respectively then residual stress in a thin film can be derived from Stoney's equation [201] as follows:

$$\sigma = \frac{1}{6}\left(\frac{E_s}{1-\upsilon_s}\right)\left(\frac{1}{R_2}-\frac{1}{R_1}\right)\left(\frac{t_f^2}{t_s}\right) \tag{5.6}$$

Where E_s and v_s are Young's modulus and Poisson's ratio of the substrate respectively and t_s and t_f are thicknesses of substrate and film respectively. For the validity of Stoney's formula, thickness of the film should be much less than that of substrate ($t_f << t_s$). For present analysis sign convention for compressive and tensile stress has been taken negative and positive respectively. Surface profiles were obtained by the analysis of two beam interference fringes formed between the substrate and an optical flat standard in a laser Fizeau interferometer [202]. The complex surface shapes have been fitted to Zernike polynomial function [202] for extracting the spherical shape component from the overall surface shape. The effective radius of curvature of the substrate has been calculated from curvature profiles using the following equation [203]:

$$R = \frac{r^2}{2s} + \frac{s}{2} \tag{5.7}$$

Here R is radius of substrate (circular) and s is the sag in the curvature profile. The surface profiles of substrate before and after deposition of GLAD film are shown in Fig. 5.8. Changes in surface profile after coatings are clearly visible. The value of Si (111) substrate parameters for the calculation of stress are: E_s=188 GPa [204], v_s=0.28, and $t_{s=}$ 0.3 mm. ND ZrO_2 film shows a high compressive stress of 5259 ± 500 MPa whereas GLAD films exhibit relatively much lower stress varying between -60 MPa to +184 MPa.

ND film shows a continuous and dense microstructure with no visible columns as observed from FESEM images presented in Fig. 5.5. High compressive stress in ND films can be explained either by atomic peening [205-207] or ad-atom diffusion [205, 208-210]. Atomic peening governs the stresses where high energy incoming atom or particle strikes the growing surface causing local atomic displacement and hence densification of films. Ad-atom diffusion model assumes that excess ad-atoms get incorporated in grain boundaries leading to higher densities than expected in equilibrium. However, these two methods of film

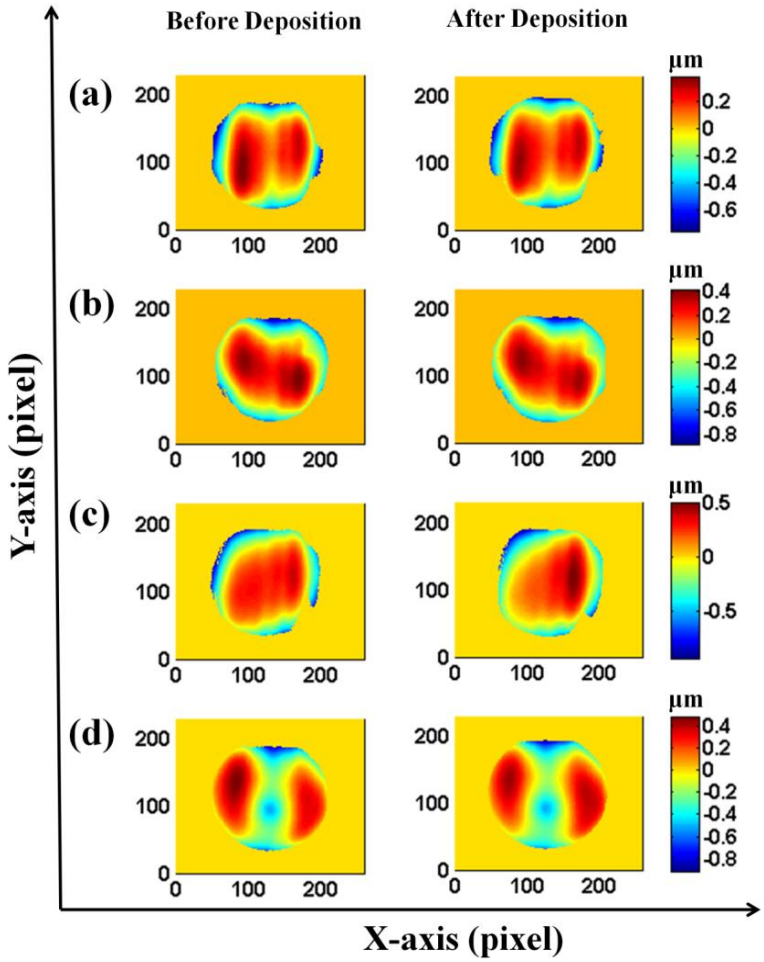

Fig. 5.8 *(a, b, c, d): Surface contours of Si substrate before and after deposition of GLAD ZrO_2 films, S-1, S-2, S-4, and S-5 respectively.*

densification are different. Ad-atom diffusion dominates at high substrate temperature under high atomic mobility over surface while atomic peening dominates in case of high kinetic energy of ad-atom. Densification of thin films leads to large compressive stress due to

reduction in inter-atomic distance and/or defects at grain boundary [205, 211]. In present case, we have not heated substrate and hence atomic peening process is mainly responsible for high compressive stress in ND ZrO_2 film. For GLAD film, reduction in stress can be attributed to the evolution of porous columnar microstructure caused by prominent atomic shadowing effects. Inter-atomic distance between the atoms on the edges of columns which are facing each other becomes comparable (or larger) than the equilibrium inter-atomic distance in GLAD films. Tension is generated in the columns due to resulting inter-atomic attraction between them. The variation of the estimated stress in the ZrO_2 GLAD films is shown in Fig. 5.9. The film, S-1 with the least value of parameter ω depicts a compressive stress of -63 MPa and as the parameter, ω increases further, stress switches from compressive to tensile with gradually increasing magnitude. This variation can be explained in terms of variation of inter-columnar distance in GLAD microstructure with ω. As described in section 1.3.3,

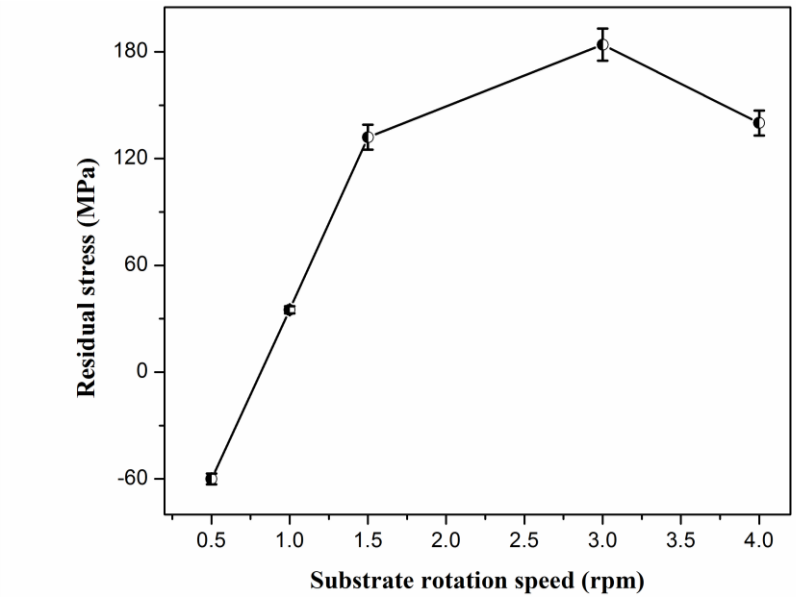

Fig. 5.9*: Plot of residual stress vs. substrate rotation (ω) for GLAD ZrO_2 thin films.*

columns get finer with the increase in ω and consequently, the average inter-columnar distance increases, eventually becoming more than the equilibrium value. This increase in

inter-columnar distance with the increase in ω leads to the increase in tensile stress. However, the sample S-5 (4 rpm) having the lowest packing density shows a lower tensile stress than S-4 (3 rpm). This can be attributed to the decrease in the slope of inter-atomic attractive forces with high inter-atomic separation [211, 212].

5.1.4. Conclusion

Several ZrO_2 thin films have been deposited at glancing angle of 82º at different substrate rotations by RF magnetron sputtering. For comparison, ZrO_2 film has also been deposited at normal angle of 0º. Structural, morphological, optical and mechanical properties of ZrO_2 films have been studied extensively. GLAD films depict preferential structural growth in monoclinic phase with (110) direction whereas ND film depicts a strong preferential growth in m (-111) direction. Preferential growth in different directions has been attributed to different angle of deposition for GLAD and ND ZrO_2 films. GIXRD spectra of ZrO_2 films also display tetragonal peak with t (11-1) direction. Fine nanocrystalline structure is responsible for the occurrence of room temperature tetragonal phase. Geometrical grain size (correlation length) decreases with the increase in substrate rotation for GLAD films. AFM images show an evolution of surface grain from non-circular to circular shape with increased voids with the increase in substrate rotation. 3-D AFM images indicate that nano-columns get more cylindrical and finer with substrate rotation. GLAD films exhibit lower refractive index as compared to ND ZrO_2 film. The refractive index lowering is the result of increased porosity due prominent atomic shadowing at glancing angles. High porosity in GLAD ZrO_2 films is corroborated by FESEM cross-sectional and AFM images. GLAD films show lower rate of deposition compared to ND film due to the reduction in sticking coefficient of ad-atoms at glancing angle. Further, deposition rate for GLAD films increases with substrate rotation. The trend of increasing deposition rate implies an increase in column length and decrease in column diameter with substrate rotation. Further, effective refractive index of

GLAD ZrO_2 films manifests decreasing trend with increasing substrate rotation. This trend has been attributed to the variation in columnar microstructure with substrate rotation. Both, variation of rate of deposition and effective refractive index are corroborated by film morphologies measured by AFM. Residual stress in the films switches from compressive to tensile as the angle of deposition changes from 0º to 82º. ND film possesses high compressive stress of 5259 MPa whereas stress for GLAD films lies between -60 to 184 MPa. High compressive stress of ND film is the attribute of atomic peening which leads to densification of the film. Variation of stress for GLAD films with substrate rotation has been explained from the dependency of stress on inter-atomic distance in attractive region of inter-atomic forces. This study could be useful in the development of interference based multilayer devices and other technologies by GLAD.

5.2. Glancing Angle Deposition of ZrO_2 thin films by EB Evaporation

5.2.1. Introduction

In this part, ZrO_2 thin films have been deposited on fused silica substrate by EB evaporation in normal as well as GLAD configuration. Since GLAD films are highly porous, the environmental/mechanical stability of optical devices utilizing such film is of great concern. For the assessment of such stabilities, estimation of elastic properties (indentation modulus) which are related to thermal stresses in thin films, are of great importance. The Indentation elastic modulus of thin films, which differs significantly from those of the bulk materials due to the interfaces, microstructure, and the underlying substrates and also affected by the process parameters and the deposition technique, has been estimated from contact resonance spectra achieved through AFAM [88] measurement. Along with that the optical and

morphological properties of both the films are characterized in order to show the substantial difference between two films.

5.2.2. Experimental Details

For the present experiment, thin films of ZrO_2 have been deposited on fused silica substrate at 200°C by reactive EB deposition technique. The films have been deposited at two deposition angles: α=0° and α=82°. The deposition angle α is defined as the angle subtended between the substrate normal and the incident vapour flux. Different value of α is achieved by tilting the substrate, whereas the incoming vapour direction is held fixed. The total working pressure during both the deposition was kept at $1x10^{-4}$ mbar. The rate of deposition is monitored and controlled by quartz crystal monitors and in both cases deposition rate has been kept 5Å/sec. The optical constants of the film were determined by analysis of transmission spectra measured using UV-VIS-NIR spectrophotometer [72]. Since, scattering is an important factor regarding these films application in optical devices; therefore one must have an idea about the roughness of the films. Surface morphology as well as roughness of the films was estimated using AFM in Semi-Contact mode. The quantitative elastic properties in terms of indentation modulus films have been determined using AFAM.

5.2.3. Results and Discussion

5.2.3.1. Determination of Optical Constants

Using the Tauc-Lorentz dispersion model along with Urbach tail [213] modification transmission of the thin film has been generated theoretically and is fitted with the measured transmission spectra as shown in Fig. 5.10 for ZrO_2 thin films. From fitting analysis, the parameters of the dispersion model and the thickness of the film have been determined. Finally fitting parameters have been used to determine the refractive index (*n*) of the films. The thickness and refractive index of the films obtained as above have been listed in Table

5.3. The spectroscopic values of refractive index for both the films are plotted in the inset plot of Fig. 5.10. The refractive index@550 nm for GLAD ZrO_2 film is 1.40 while for normal deposited film is 2.01. Such a low refractive index value obtained for GLAD film confirms the high porosity in film due to ballistic shadowing of columns during film growth. Using the experimentally determined refractive index value and standard refractive index value for bulk ZrO_2 [214] porosity in the samples has been calculated using Bruggeman effective medium approximation (EMA) [215].

Table 5.3*: Quantitatively estimated optical and morphological parameters of normal and oblique angle deposited ZrO_2 thin films.*

ZrO_2 deposition configuration	Refractive index	Film porosity	Film thickness (nm)	RMS surface roughness (nm)	Grain size (nm)
GLAD (82°)	1.40 ± 0.01	0.64 ± 0.01	524.7 ± 1	8.9	168 ± 18
Normal (0°)	2.01 ± 0.01	0.11 ± 0.01	371 ± 0.8	1.2	75 ± 10

Obviously, from Table 5.3, the porosity in GLAD film is 6 fold higher than that of normal deposited film. Transmission spectra for GLAD film shows an antireflection effect (T=94% or more) for wavelength greater than 600 nm. This is the consequence of lower refractive of such films compared to fused silica. But there is a significant decrease in transmission (for GLAD film) below wavelength 500 nm. This may be the result of increased scattering and absorption losses. In GLAD films, column size is significantly high and becomes of order of wavelength of light. Increase in absorption may be due to multi-reflection of light between columns inside film. Fig. 5.11 (a) and (b) present 3-D surface morphology of ND and GLAD ZrO_2 thin films respectively. The ND film depicts dense surface (high grain density) morphology and small grains whereas surface of GLAD ZrO_2 film is porous (lower grain density). Obviously a height variation on the surface of GLAD film is approximately 5 fold higher than the ND ZrO_2 film. RMS roughness values for ND

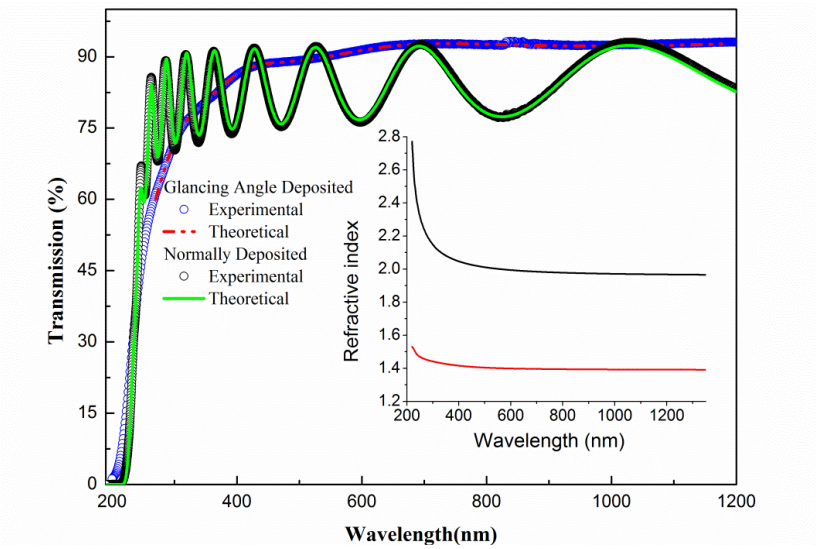

***Fig. 5.10**: Experimental and theoretical transmission curves & dispersive refractive indices of normal and GLAD ZrO_2 thin films*

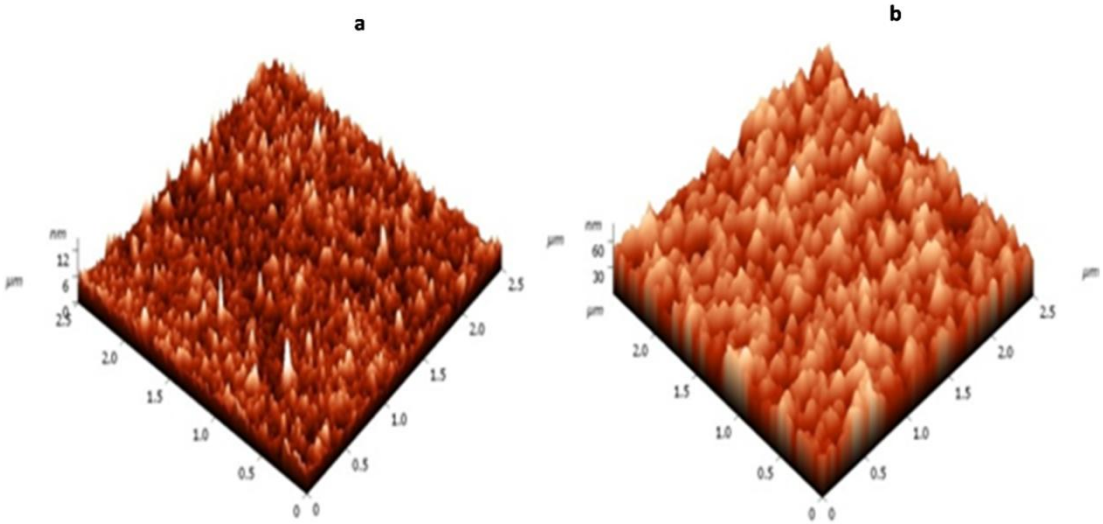

***Fig. 5.11**: 3-D surface topography of (a). Normal and (b). GLAD ZrO_2 thin films.*

and GLAD films are 1.2 and 8.9 nm respectively. Such a great difference in surface morphology is the consequence of introduction of high porosity in oblique angle deposited film due to modified (tilted columnar growth) growth mechanism. Average grain size and RMS roughness as obtained from AFM measurements are listed in Table 5.3.

5.2.3.2. Determination of Indentation Modulus from AFAM Measurements

In AFAM, flexural resonant frequencies of AFM cantilever are measured. Detailed theory of the measurement is discussed in refs. [59, 60, 92, 93, 95, 97, 216]. DLC coated Si tips

(NSG_DLC10) with 1st free resonance frequency 213.5 kHz, has been chosen for its better hardness and stability in tip geometry having indentation modulus of 590 ± 20 GPa. The spring constants of the cantilever was found to be 9.2 N/m using Sader analysis [107]. The contact resonance spectra for Si (100) (reference sample) and ZrO_2 thin films have been measured for the 1st (f_1) and 2nd (f_2) flexural modes. For each sample, the contact-resonance frequencies were measured for four different static normal loads.

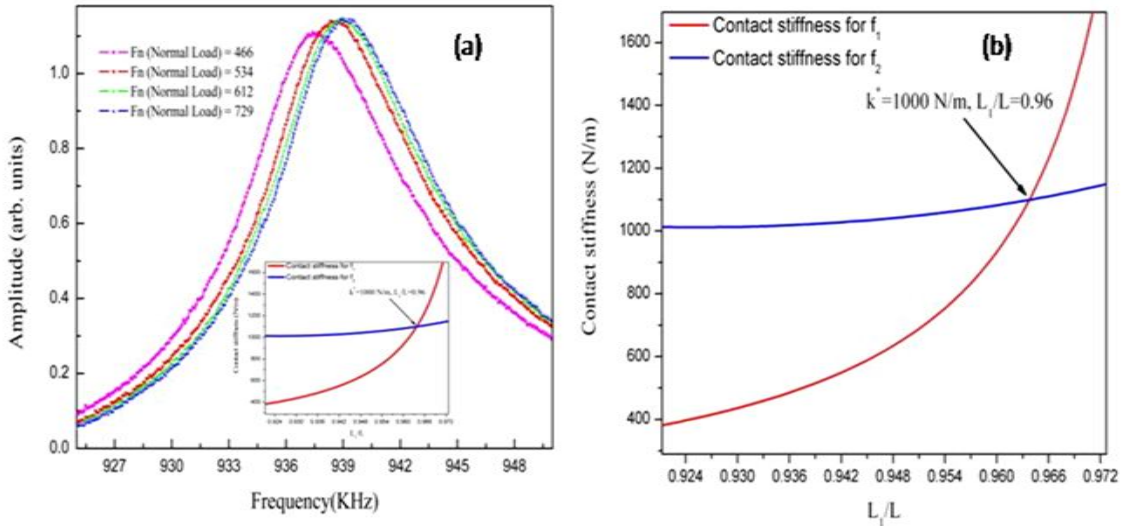

Fig. *5.12* *(a): Plot of first contact resonance frequency with varying static load and (b) Contact stiffness vs. L_1/L for oblique angle deposited ZrO_2 film.*

Fig. 5.12 (a) shows measured 1st contact resonance spectra for GLAD film. This spectra shows that the resonance frequency as well as the amplitude increase with increasing static normal load, as expected from the theory of flexural vibrations and also ensures that measurements are taken within elastic limit. Since, exact position of tip on cantilever is not known, assuming a small range of this position, contact stiffness for both 1st and 2nd flexural modes for Si (100) reference sample and both ZrO_2 films are plotted, and their intersection corresponds to exact value of cantilever tip position (L_1/L). The contact stiffness values for Si (100) reference and ZrO_2 thin films are listed in Table 5.4.

Plot of contact stiffness for GLAD film is shown in Fig. 5.12 (b). For all the samples, L1/L was found to be 0.96. The indentation modus for GLAD ZrO2 film is 74 GPa which is much lower than that of ND film (160GPa). This is due to high porosity in GLAD films.

Table 5.4*: The parameters obtained from AFAM analysis.*

Sample Name	f_1 (kHz)	f_2 (kHz)	Contact Stiffness (N/m)	Indentation Modulus (GPa)
GLAD ZrO_2	939	2359	640	74 ± 8
Normal deposited ZrO_2	965	2610	983	160 ± 17
Si (100)	966	2675	1000	165 ± 17

The relative error in the measurement of indentation modulus is about 10%, which is due to the uncertainties in tip geometry and dimensions.

5.2.4. Conclusion

ZrO_2 thin films have been deposited on fused silica substrate at angles 82° and 0°. Both the films have been characterized by spectrophotometer, AFM and AFAM techniques. The GLAD film shows high porosity with refractive index 1.40. Porous structure of GLAD film again has been confirmed by AFM image which depicts a highly porous surface morphology with bigger grains and high surface RMS roughness compared to normal angle deposited film. Elastic modulii of indentation measured from AFAM were found to be 74 and 160 GPa for GLAD and ND film respectively. Such a high decrease in indentation modulus for oblique angle deposited films is the consequence of increased porosity due to tilted columnar micro-structure. Such GLAD films have great potential in designing challenging optical filters utilizing inhomogeneous layers or rugate structures.

CHAPTER 6: OBLIQUE ANGLE DEPOSITION OF SiO_2 THIN FILMS

6.1. Introduction

As discussed in preceding chapters, oblique angle deposition of thin films is being popular and used to fabricate interference based optical devices, micro sensors, photonic crystals, and rugate structures [1, 4, 82]. Recently, porous Silicon dioxide (SiO_2) thin films fabricated using oblique angle depositions have drawn attention for practical applications, such as antireflection coatings humidity sensors, and microelectronic and photonics devices [37, 82]. SiO_2 thin films have excellent optical properties in UV, visible and near-infrared regions, good adhesion, environmental stability and high laser damage threshold [217-219]. Such properties depend on the deposition methods and process parameters.

In present work, SiO_2 single-layer thin films have been deposited at two oblique angles by EB evaporation. Their optical constants have been derived from transmission measurements through Tauc-Lorentz dispersion model. Surface morphology of such SiO_2 thin films has been characterized to determine surface roughness and geometrical grain structure. The properties of obliquely deposited SiO_2 films have also been compared with normally deposited films. Finally, a broad band antireflection coating using oblique angle deposited SiO_2 films have designed and fabricated on glass substrate.

6.2. Experimental Detail

Deposition of SiO_2 thin films were carried out in oblique angle configuration at 70° and 75° at 200°C by EB evaporation. Base pressure prior to deposition was achieved to be $1x10^{-6}$ mbar to remove contaminations from vacuum chamber. The rate of deposition was kept 4 Å/s.

Film thickness was in-situ measured and controlled by quartz crystal monitor (Inficon make). Oxygen partial pressure inside the chamber was controlled by mass flow controller and kept $1x10^{-4}$ mbar during deposition. Transmission spectra of thin films and coatings were measured by spectrophotometer in the wavelength range of 300–1200 nm. Deposited thin films were also characterized by AFM to investigate morphological properties.

6.3. Determination of refractive index through Tauc-Lorentz (TL) dispersion model

Jellison and Modine [164] presented an explicit dispersion relation with meaningful parameters for inter-band transition in amorphous materials, which is consistent with the Kramers-Kronig relation. They considered Tauc joint density of states and Lorentz oscillator model together to derive Tauc-Lorentz dispersion model and obtained following parametric expression for the imaginary part of the dielectric constant of the material (ε_2) as follows:

$$\varepsilon_{2TL} = \frac{AE_o\Gamma(E-E_g)^2}{\left\{(E^2-E_o{}^2)^2+\Gamma^2E^2\right\}E}, E > E_g$$

$$=0, \qquad E \le E_g \qquad (6.1)$$

The expression for real part of dielectric constant has been obtained using Kramers-Kronig relation [164]. Thus, in TL model proposed by Jellison and Modine, dispersion of optical constants can be described by five parameters A, E_o, E_g, Γ and $\varepsilon_{1TL}(\infty)$.

In present work, transmission spectra of single layers of obliquely deposited SiO_2 thin films at deposition angle 70° and 75° were fitted using TL dispersion model and χ^2 (chi) square minimization [71, 72] was carried out to determine the best fit values of the fitting parameters. From fitting parameters, spectroscopic refractive indices and thickness of obliquely deposited SiO_2 thin films were derived. Optical constants (refractive index and extinction coefficient) of glass substrate (BK7) were obtained by fitting transmission spectra

of bare substrate using Cauchy's dispersion relation [72] for accurate determination of refractive index of SiO_2 thin films.

6.4. Results and Discussion

6.4.1. Dispersive refractive of single layer SiO_2 thin films

Dispersive refractive index and thickness of SiO_2 thin films deposited at 75°, 70° and 0° have been derived from measured transmission curves of respective thin film. **Fig. 6.1** (a) presents the measured and fitted transmission curves of single layer SiO_2 thin film deposited at 70°.

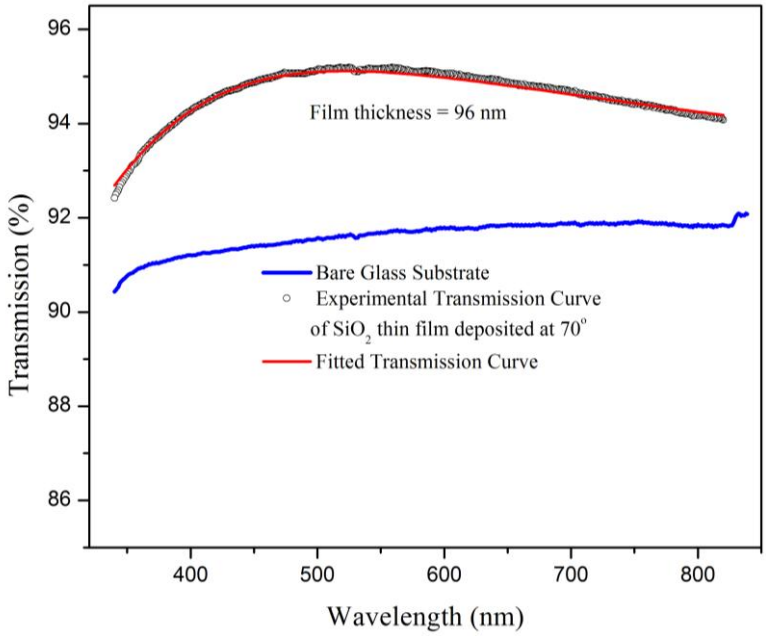

***Fig. 6.1**: Measured and fitted transmission curves of SiO_2 film deposited at 70°.*

Dispersive refractive index of the films deposited at different angles is shown in Fig. 6.2. SiO_2 films deposited at angle 75°, 70° and 0° depict refractive index values of 1.15, 1.25 and 1.46 respectively at 600 nm. Lowering in refractive index of SiO_2 films deposited at oblique angles is the result of porous columnar microstructure and the porosity increases as the angle of deposition increases. Increase in porosity is the result of increase in atomic shadowing with the increase in deposition angle. Consequently, refractive index decreases with the increase in angle of deposition.

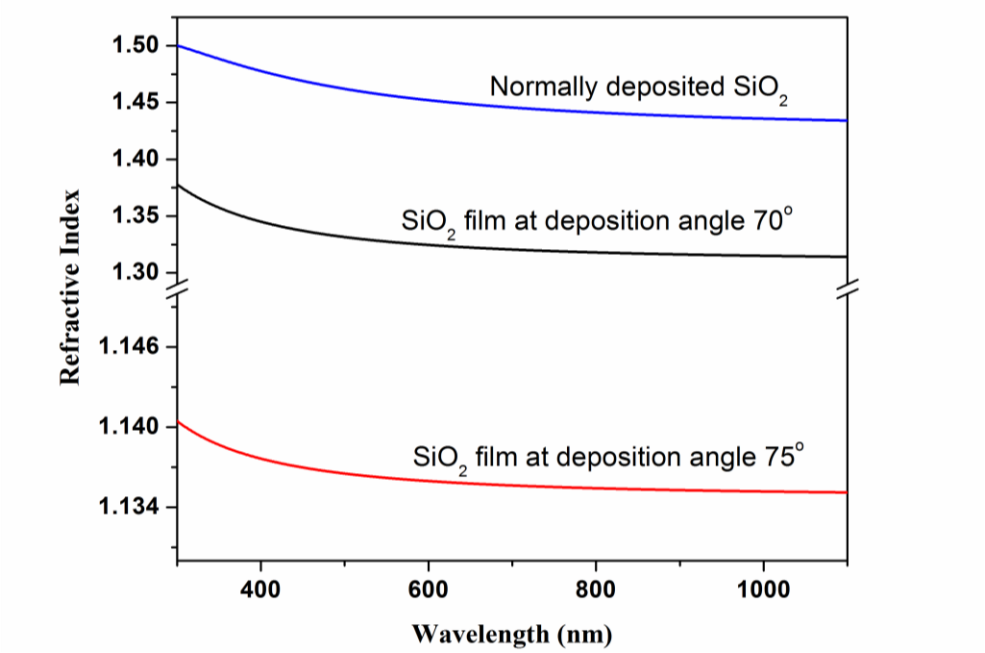

***Fig. 6.2**: Dispersive refractive index of SiO_2 films deposited at different angles.*

***Table. 6.1**: Estimated refractive index and surface statistical parameters of SiO_2 thin film.*

Sample Name	Refractive index@600nm	AFM RMS roughness (nm)	Film thickness (nm)	Average grain size (nm)
SiO_2 (75°)	1.15 ± 0.02	4.0	393 ± 1	220 ± 40
SiO_2 (70°)	1.25 ± 0.03	1.2	96 ± 4	120 ± 10
SiO_2 (0°)	1.46 ± 0.03	1.2	400 ± 4	100 ± 10

Finally in-situ quartz crystal monitor thickness readings were calibrated with post deposition thickness derived from transmission spectra.

6.4.2. Surface morphology

In Fig. 6.3 (a) and (b), morphology of SiO_2 films deposited at 75° and 0° angle are shown. It can be noted that roughness value (1.2 nm) and grain size (100-120 nm) for films deposited at 70° and 0° are similar. It indicates that there is no significant roughening of films up to the deposition angle of 70° (less shadowing effects). However, Film deposited at 75° deposition angle exhibits a 3-fold increase in RMS roughness and 2-fold increase in surface grain size.

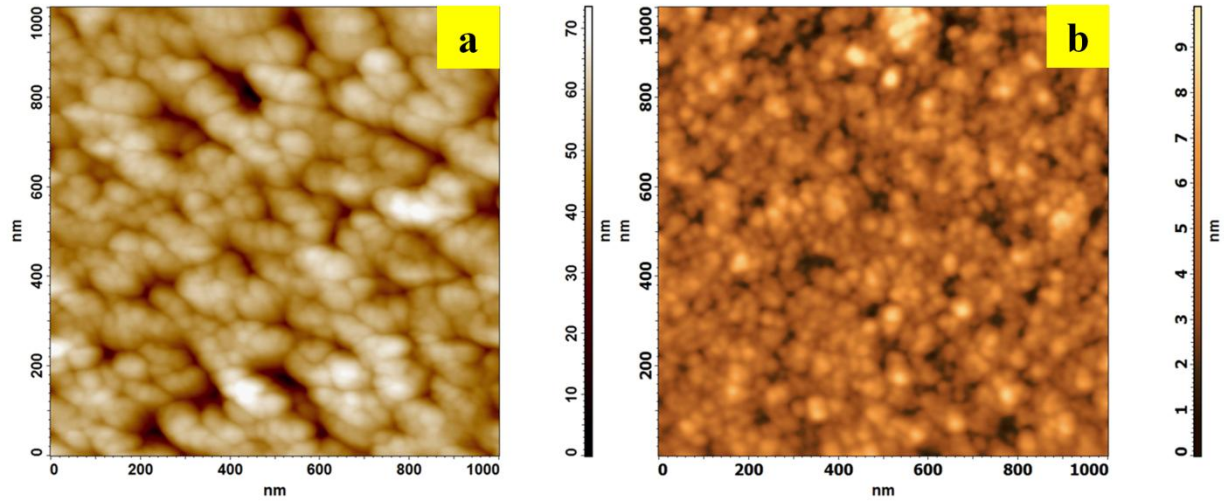

Fig. 6.3 *(a). Surface morphology of SiO_2 film deposited at 75° and (b). 0°.*

Higher roughness and bigger grains are due to dominant atomic shadowing at higher deposition angles. Results of optical and morphological analysis of SiO_2 films are presented in Table 6.1. Since films deposited at higher deposition angles show significantly high roughness, they may not be useful in UV and VUV wavelength region due to high scattering loses.

6.4.3. Design and fabrication of broadband antireflection coating

Antireflection coatings are routinely used in spectroscopic and laser experiments. Conventionally, to obtain broadband antireflection coating, a non-quarter wave multilayer design (several layers) of two or more optical thin films is required. Designs and theory of such conventional anti-reflection coating is described in ref. [51] in detail. In Fig. 6.5 (b), a 24-layer design (12-layers on each side of the glass substrate) of broadband antireflection is shown. Here band is limited and transmission is less than 98 % in the band. However with more sophisticated designs, better results are possible.

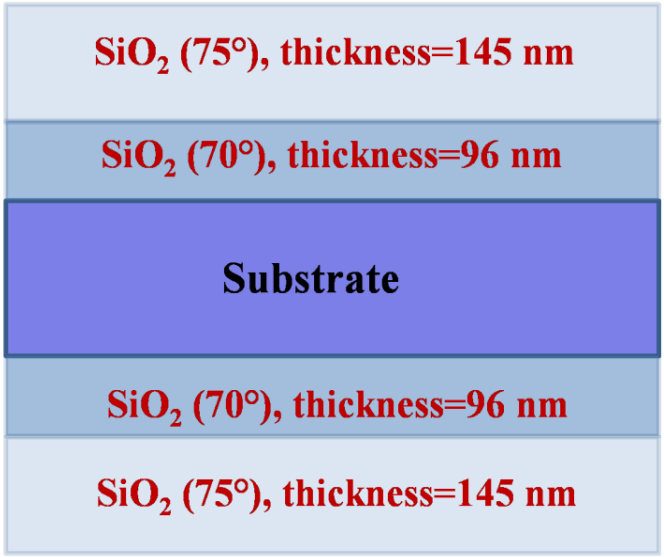

Fig. 6.4*: Design of broad-band antireflection coating using oblique angle deposition of SiO_2 layers.*

It is well understood that reflection loses in optical components used for laser, optical instruments and spectroscopic applications arise from interfaces. Higher refractive index contrast of two materials at interface leads to higher reflection loses. In many applications, such reflection loses are required to be the least. In present work, refractive index contrast of materials at interfaces has been reduced by utilizing the oblique angles deposition of 2-layers of SiO_2 thin films on both sides of glass.

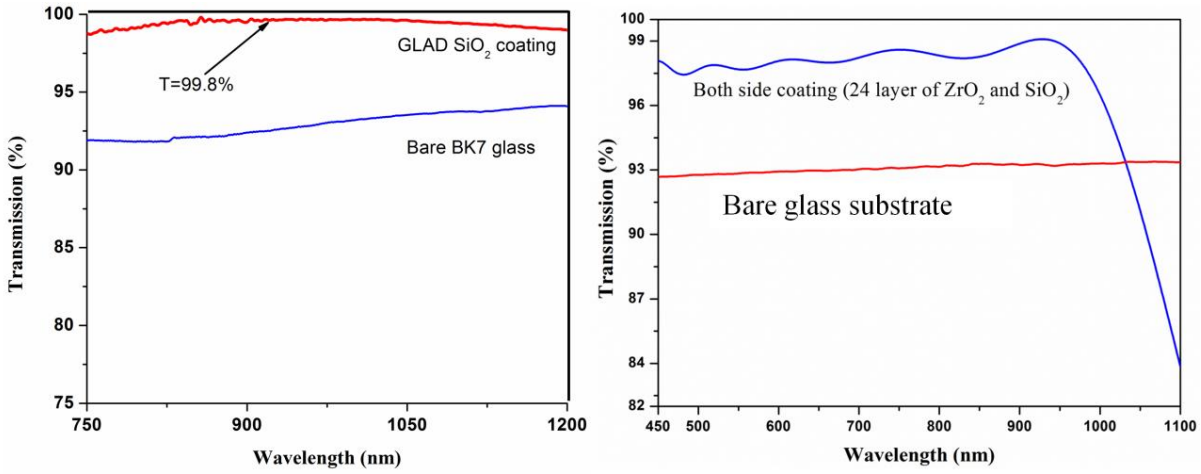

Fig. 6.5 *(a). Measured transmission characteristics of broad-band anti-reflection coating fabricated using oblique angle deposition of SiO_2 layers. (b). Theoretical transmission of a conventional 24-layer (12-layers ZrO_2/SiO_2 each side) broad-band antireflection coating.*

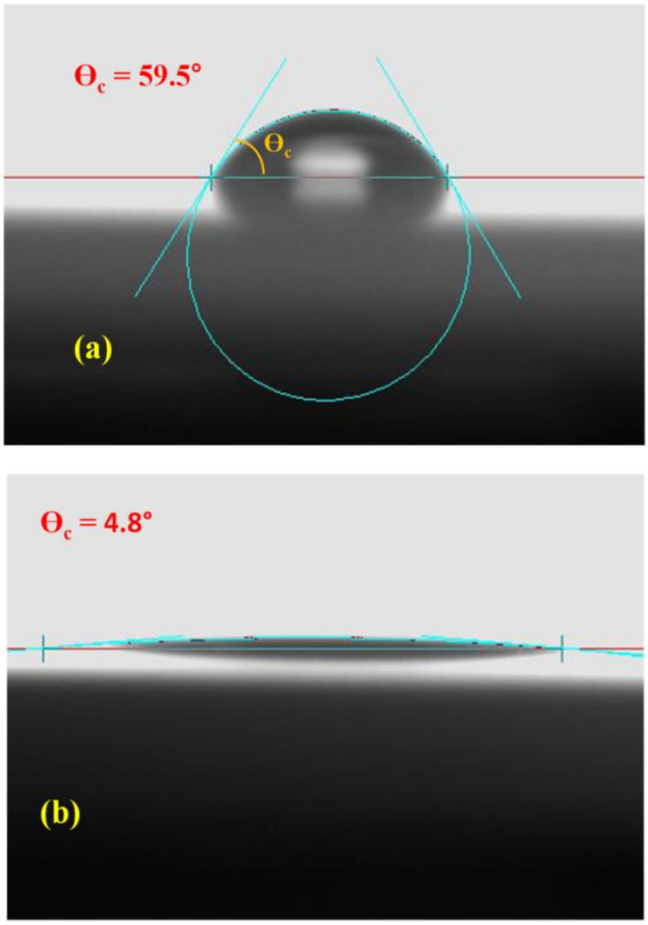

Fig. 6.6 *(a). Measured contact angle (water) for bare BK7 glass substrate and (b). Coated BK7 substrate with SiO_2 film deposited at angle 75°.*

We have designed an antireflection coating at 850 nm with non-quarter wave thicknesses of porous SiO_2 thin films as shown in Fig. 6.4. In Fig. 6.5 (a), spectral characteristic of final device is shown. The device depicts an average transmission of 99.2% in the wavelength range, 750 nm to 1200 nm. The peak transmission achieved is 99.8% around 900 nm. The transmission spectra of final device have been simulated using multilayer software and it was found that thicknesses of individual layers differ slightly from designed thicknesses. Such deviation from design thicknesses is the result of uncertainties in deposition angle and process parameters. As discussed above, conventional 12-layer antireflection designs results small band with poor transmission. Antireflection region of present device can be tuned by

changing the thickness of individual layers and antireflection effect could further be enhanced by optimizing deposition angles and thicknesses for individual layers.

Contact angle measurements have also been performed on antireflection coating to assess its wetting characteristic. Measured results are shown in Fig. 6.6 (a) and (b). Bare glass substrate shows a contact angle of 59.5° ± 0.5° while antireflection coating shows high wetting character with contact angle 4.8° ± 0.5°. Reduction in contact angle for coated substrate can be attributed to random and high fluctuations of height with respect to a mean plane over the surface (high roughness). Such hydrophilic coatings could be applied on glass encapsulation of solar panels to increase input light by providing self-cleaning, reducing reflection loses and reducing scattering loses due water droplets on glass.

6.5. Summary

Optical constants of SiO_2 thin films deposited at different deposition angles have been determined using suitable computation and modeling. Optical constants and thickness calibration of such films have been used to design and develop a broad-band antireflection coating with two obliquely deposited layers at 70° and 75° on both sides of substrate. Antireflection coating depicts more than 99.2 % transmission with a band of 450 nm. Such coatings could also be applied to solar panel encapsulation to enhance their efficiency by reducing reflection and scattering loses and self-cleaning of surface.

CHAPTER 7: SUMMARY AND FUTURE PROSPECTS

7.1. Summary

In this thesis, importance of oblique/glancing angle deposition to fabricate thin films with tunable microstructure has been demonstrated. As discussed in chapter 1, tunable microstructure is generally achieved by employing the variation in angle of deposition and substrate rotation. Nucleation and film growth mechanism, theory, role of substrate motion and angle of deposition and other factors affecting columnar microstructure in oblique angle deposition are discussed. Background research work carried out, especially pertaining to optics and photonics has been presented. Deposition techniques such as EB evaporation and magnetron sputtering to fabricate oxide thin films in the present dissertation have been described. Various characterization technique used are described.

In the present thesis, obliquely deposited HfO_2, ZrO_2 and SiO_2 thin films have been studied. Morphological, structural, optical, micro-structural, elastic and local structure properties of such films have been investigated in detail. The major outcomes of the thesis are summarized as below:

EB evaporated HfO_2 thin films deposited at different oblique angle exhibit porous tilted columnar microstructure. The porosity is highest for film deposited at glancing angle (80°) and it decreases as the angle of deposition decreases. The indentation modulus of HfO_2 film is least with a value of 42 GPa for GLAD film and highest for normally deposited film with value 221 GPa. Film density and indentation modulus depicts a similar variation (decreasing) trend with angle of deposition. The decreasing indentation modulus of HfO_2 thin films is an attribute of increase in porosity with angle of deposition. The GLAD film exhibits highest

grain size and intrinsic RMS surface roughness. The intrinsic roughness and fractal spectral strength follow the similar trend with deposition angle. Behaviour of surface morphological parameters and refractive index with deposition angles have been explained by the combined effect of atomic shadowing, re-emission of ad-atoms and diffusion of ad-atoms.

RF sputtered HfO_2 thin films have been deposited at two different glancing angle of deposition of 82° and 86° and at four different targets to substrate distances visualizing 70 mm, 90 mm, 110 mm and 125 mm. The morphological, optical and structural properties of the films have been investigated. The films show prominent nanostructures for an optimum target-substrate distance (D_{TS}) 110 mm with 82^o angle of deposition. The grains are elliptical in shape for lower D_{TS} (70-90 mm) and become circular for higher D_{TS}. The switching in the shape of grain with D_{TS} has been explained in terms of the variation in ad atom kinetic energy. The refractive index follows almost similar trend as that of deposition rate with D_{TS} except at 110 mm target-substrate distance for which the film deposited at 82° exhibits lower refractive index compared to that at 86°. At 86° angle and 110 mm target-substrate distance, the formation of amorphous crystallographic structure is responsible for relatively higher index compared to that at 82°. The films show polycrystalline monoclinic crystal structure. At lower D_{TS} values, the crystallinity has improved with the increase in deposition angle due to the reduction in deposition rate which helps in organizing the atoms in more crystalline form. However at higher distance (> 90 mm), the crystallinity has degraded with deposition angle due to the lesser diffusion due to the enhanced shadowing effect at higher deposition angle.

Effect of substrate rotation on ZrO_2 thin films deposited at glancing angle of 82º by RF magnetron sputtering has been investigated and their properties have been compared with that of film deposited at angle of 0º. The GLAD ZrO_2 films depict preferential structural growth in monoclinic phase with (110) direction whereas ND film depicts a strong preferential growth in m (-111) direction. Preferential growth in different directions is attributed to

different angle of deposition. Presence of t (11-1) phase of ZrO_2 in small fraction is also confirmed which is due to fine nanocrystalline structure (crystallite size < 30 nm). The geometrical grain size decreases with the increase in substrate rotation for GLAD films. Shape of the surface grains changes from non-circular to circular with substrate rotation. 3-D AFM images indicate that nano-columns get more cylindrical and finer with substrate rotation. GLAD films exhibit lower refractive index and rate of deposition as compared to ND ZrO_2 film. Prominent atomic shadowing and low sticking coefficient are responsible for lowering in index and rate respectively. Further, deposition rate for GLAD films increases with the increase in substrate rotation which implies an increase in column length and decrease in diameter. Refractive index of GLAD ZrO_2 films shows a decreasing trend with the increase in substrate rotation and the trend is the attribute of variation in columnar microstructure with substrate rotation. Normally deposited film possesses high compressive stress of 5259 MPa whereas stress for GLAD films lies between -60 to 184 MPa. High compressive stress of ND film is the attribute of atomic peening which leads to densification of the film. Residual stress in GLAD films switches from compressive to tensile with substrate rotation and the variation of stress with substrate rotation is explained in terms of variation of inter-atomic forces with inter-columnar distance.

EB evaporated ZrO_2 thin films at similar deposition angles 80° and 0° have also been studied to investigate their elastic, morphological and optical properties. The film deposited at 80° shows high porosity with refractive index 1.40. Porous structure of GLAD film has been confirmed by surface morphology. Surface morphology of GLAD (80°) film contains bigger grains and high surface RMS roughness compared to normal angle deposited film. Measured elastic modulus of indentation was found to be 74 and 160 GPa for GLAD and normally deposited film respectively. Such a high decrease in indentation modulus for oblique angle deposited films is the consequence of increased porosity.

Finally, obliquely deposited SiO_2 thin films have been used to design and fabricate a broad-band antireflection coating. The Coating has been designed with two obliquely deposited layers of SiO_2 films at 70° and 75° on both sides of BK7 glass substrate. Due to decrease in refractive index contrast at interface in this multilayer device, transmission improves from 90 % to 99.2 % in a wavelength band of ~ 450 nm. Moreover, this device displays an average transmission of more than 98% in the wavelength region, 300nm to 1200 nm. Such coating can be deposited on solar panel encapsulations to increase light input inside the panel. Such coating having porous layers of SiO_2 film on top exhibits a contact angle of 4°-5° while for bare glass, contact angle was measured to be around 60°. High wetting character of such films can again enhance the efficiency of solar panel by rendering self-cleaning of surface and reducing scattering loses due to water droplets on the surface.

7.2. Future Prospects

In future, effect of substrate temperature and deposition pressure could be explored for oblique angle deposition of various optical thin films for further tuning of various properties. Co-deposition/co-sputtering of two different materials in OAD configuration could also be investigated for their gained advantages. More material such as Ta_2O_5, MgF_2, Gd_2O_3, TiO_2 etc., would be examined in oblique angle configuration to assess their properties. Finally oblique angle deposition of various optical coating materials will be used to achieve continuous variation of refractive in a defined manner (rugate structure) across the thickness of the coating. Such rugate structures of different materials and profile could be utilized to fabricate challenging interference optical devices such as Raman notch filter, edge filter and beam multiplexer for nuclear detectors and radiation dosimetry applications and laser isotope separation experiments. OAD coatings would also be used to fabricate optical waveguides. Laser induced damage resistance measurement of such obliquely deposited optical coating would be carried out to assess the qualification for high power laser applications.

REFERENCES

[1] M.M. Hawkeye, M.T. Taschuk, M.J. Brett, Introduction: Glancing Angle Deposition Technology, Glancing Angle Deposition of Thin Films, John Wiley & Sons, Ltd2014, pp. 1-30.

[2] K. Robbie, M.J. Brett, Sculptured thin films and glancing angle deposition: Growth mechanics and applications, Journal of Vacuum Science and Technology A, 15 (1997) 1460-1465.

[3] M.T. Taschuk, M.M. Hawkeye, M.J. Brett, Chapter 13 - Glancing Angle Deposition, in: P.M. Martin (Ed.) Handbook of Deposition Technologies for Films and Coatings (Third Edition), William Andrew Publishing, Boston, 2010, pp. 621-678.

[4] A. Barranco, A. Borras, A.R. Gonzalez-Elipe, A. Palmero, Perspectives on oblique angle deposition of thin films: From fundamentals to devices, Progress in Materials Science, 76 (2016) 59-153.

[5] R. Messier, T. Gehrke, C. Frankel, V.C. Venugopal, W. Otaño, A. Lakhtakia, Engineered sculptured nematic thin films, Journal of Vacuum Science and Technology A, 15 (1997) 2148-2152.

[6] B. Dick, M.J. Brett, T. Smy, Controlled growth of periodic pillars by glancing angle deposition, Journal of Vacuum Science and Technology B, 21 (2003) 23-28.

[7] J. Lintymer, N. Martin, J.M. Chappé, P. Delobelle, J. Takadoum, Influence of zigzag microstructure on mechanical and electrical properties of chromium multilayered thin films, Surface and Coatings Technology, 180–181 (2004) 26-32.

[8] S. Fahr, C. Ulbrich, T. Kirchartz, U. Rau, C. Rockstuhl, F. Lederer, Rugate filter for light-trapping in solarcells, Optics Express, 16 (2008) 9332-9343.

[9] Y. Zhu, H. Jiao, Rugate filter with multi-channel grown by glancing angle deposition, Optik-International Journal for Light and Electron Optics, 123 (2012) 1501-1503.

[10] K. Kaminska, T. Brown, G. Beydaghyan, K. Robbie, Rugate filters grown by glancing angle deposition, IC02, International Society for Optics and Photonics, 2003, pp. 633-639.

[11] A. Roth, Vacuum Technology, Elsevier Science2012.

[12] J.E. Mahan, Physical Vapor Deposition of Thin Films, Wiley2000.

[13] B. Dick, M.J. Brett, T. Smy, M. Belov, M.R. Freeman, Periodic submicrometer structures by sputtering, Journal of Vacuum Science & Technology B: Microelectronics and Nanometer Structures Processing, Measurement, and Phenomena, 19 (2001) 1813-1819.

[14] Y.W. Sun, J. Gospodyn, P. Kursa, J. Sit, R.G. DeCorby, Y.Y. Tsui, Dense and porous ZnO thin films produced by pulsed laser deposition, Applied Surface Science, 248 (2005) 392-396.

[15] K.L. Chopra, Thin Film Phenomena, Malabar : Robert E. Krieger Publishing Company1979.

[16] O.S. Heavens, Thin film physics, Methuen1970.

[17] M. Ohring, Materials Science of Thin Films, Elsevier Science2001.

[18] P.N. Laboratorium, Philips Technical Review, Philips Research Laboratory.1966.

[19] I. Hodgkinson, Q.h. Wu, J. Hazel, Empirical equations for the principal refractive indices and column angle of obliquely deposited films of tantalum oxide, titanium oxide, and zirconium oxide, Applied Optics, 37 (1998) 2653-2659.

[20] R.N. Tait, T. Smy, M.J. Brett, Modelling and characterization of columnar growth in evaporated films, Thin Solid Films, 226 (1993) 196-201.

[21] C. Khare, C. Patzig, J.W. Gerlach, B. Rauschenbach, B. Fuhrmann, Influence of substrate temperature on glancing angle deposited Ag nanorods, Journal of Vacuum Science & Technology A: Vacuum, Surfaces, and Films, 28 (2010) 1002-1009.

[22] C. Patzig, B. Rauschenbach, Temperature effect on the glancing angle deposition of Si sculptured thin films, Journal of Vacuum Science & Technology A: Vacuum, Surfaces, and Films, 26 (2008) 881-886.

[23] J. Lintymer, J. Gavoille, N. Martin, J. Takadoum, Glancing angle deposition to modify microstructure and properties of sputter deposited chromium thin films, Surface and Coatings Technology, 174–175 (2003) 316-323.

[24] O. Kunito, I. Kikuo, Incidence Angle Dependences of Columnar Grain Structure and Texture in Obliquely Deposited Iron Films, Japanese Journal of Applied Physics, 44 (2005) 1382.

[25] A. Hagemeyer, H.J. Richter, H. Hibst, V. Maier, L. Marosi, Crystallographic texture and morphology of obliquely deposited Co-Cr magnetic thin films on flexible polymeric substrates, Thin Solid Films, 230 (1993) 199-202.

[26] C. Buzea, K. Kaminska, G. Beydaghyan, T. Brown, C. Elliott, C. Dean, K. Robbie, Thickness and density evaluation for nanostructured thin films by glancing angle deposition, Journal of Vacuum Science & Technology B: Microelectronics and Nanometer Structures Processing, Measurement, and Phenomena, 23 (2005) 2545-2552.

[27] R.B. Tokas, S. Jena, P. Sarkar, S.R. Polaki, S. Thakur, S. Basu, N.K. Sahoo, Oblique angle deposition of HfO 2 thin films: quantitative assessment of indentation modulus and micro structural properties, Materials Research Express, 2 (2015) 035010.

[28] R. Messier, V.C. Venugopal, P.D. Sunal, Origin and evolution of sculptured thin films, Journal of Vacuum Science & Technology A: Vacuum, Surfaces, and Films, 18 (2000) 1538-1545.

[29] K. Robbie, M.J. Brett, A. Lakhtakia, First thin film realization of a helicoidal bianisotropic medium, Journal of Vacuum Science and Technology A, 13 (1995) 2991-2993.

[30] A.C. van Popta, M.M. Hawkeye, J.C. Sit, M.J. Brett, Gradient-index narrow-bandpass filter fabricated with glancing-angle deposition, Optics Letters, 29 (2004) 2545-2547.

[31] J.B. Oliver, C. Smith, J. Spaulding, A.L. Rigatti, B. Charles, S. Papernov, B. Taylor, J. Foster, C.W. Carr, R. Luthi, B. Hollingsworth, D. Cross, Glancing-angle–deposited magnesium oxide films for high-fluence applications, Optical Materials Express, 6 (2016) 2291-2303.

[32] K.D. Harris, A.C. van Popta, J.C. Sit, D.J. Broer, M.J. Brett, A Birefringent and Transparent Electrical Conductor, Advanced Functional Materials, 18 (2008) 2147-2153.

[33] A.C.v. Popta, J. Cheng, J.C. Sit, M.J. Brett, Birefringence enhancement in annealed TiO2 thin films, Journal of Applied Physics, 102 (2007) 013517.

[34] A. Lakhtakia, M.W. McCall, J.A. Sherwin, Q.H. Wu, I.J. Hodgkinson, Sculptured-thin-film spectral holes for optical sensing of fluids, Optics Communications, 194 (2001) 33-46.

[35] K. Robbie, A.J.P. Hnatiw, M.J. Brett, R.I. MacDonald, J.N. McMullin, Inhomogeneous thin film optical filters fabricated using glancing angle deposition, Electronics Letters, 33 (1997) 1213-1214.

[36] Y. Zhu, H. Jiao, Rugate filter with multi-channel grown by glancing angle deposition, Optik - International Journal for Light and Electron Optics, 123 (2012) 1501-1503.

[37] S.R. Kennedy, M.J. Brett, Porous broadband antireflection coating by glancing angle deposition, Applied Optics, 42 (2003) 4573-4579.

[38] M.O. Jensen, M.J. Brett, Functional Pattern Engineering in Glancing Angle Deposition Thin Films, Journal of Nanoscience and Nanotechnology, 5 (2005) 723-728.

[39] D.X. Ye, Z.P. Yang, A.S.P. Chang, J. Bur, S.Y. Lin, T.M. Lu, R.Z. Wang, S. John, Experimental realization of a well-controlled 3D silicon spiral photonic crystal, Journal of Physics D: Applied Physics, 40 (2007) 2624.

[40] S.R. Kennedy, M.O. Jensen, M.J. Brett, Three-dimensional square spiral photonic crystal nanostructures by glancing angle deposition, Proceedings International Conference on MEMS, NANO and Smart Systems, 2003, pp. 165-171.

[41] S.R. Kennedy, M.J. Brett, O. Toader, S. John, Fabrication of Tetragonal Square Spiral Photonic Crystals, Nano Letters, 2 (2002) 59-62.

[42] O. Toader, S. John, Proposed Square Spiral Microfabrication Architecture for Large Three-Dimensional Photonic Band Gap Crystals, Science, 292 (2001) 1133-1135.

[43] M.A. Summers, K. Tabunshchyk, A. Kovalenko, M.J. Brett, Fabrication of 2D–3D photonic crystal heterostructures by glancing angle deposition, Photonics and Nanostructures - Fundamentals and Applications, 7 (2009) 76-84.

[44] P.C.P. Hrudey, K.L. Westra, M.J. Brett, Highly Ordered Organic Alq3 Chiral Luminescent Thin Films Fabricated by Glancing-Angle Deposition, Advanced Materials, 18 (2006) 224-228.

[45] J. Gospodyn, M.T. Taschuk, P.C.P. Hrudey, Y.Y. Tsui, R. Fedosejevs, M.J. Brett, J.C. Sit, Photoluminescence emission profiles of Y2O3:Eu films composed of high-low density stacks produced by glancing angle deposition, Applied Optics, 47 (2008) 2798-2805.

[46] S.R. Kennedy, J.C. Sit, D.J. Broer, M.J. Brett, Optical activity of chiral thin film and liquid crystal hybrids, Liquid Crystals, 28 (2001) 1799-1803.

[47] K. Robbie, D.J. Broer, M.J. Brett, Chiral nematic order in liquid crystals imposed by an engineered inorganic nanostructure, Nature, 399 (1999) 764-766.

[48] S. Wang, X. Zhao, Z. Fan, J. Shao, Controllable nanostructure and optical properties of ZrO2 thin films by glancing angle deposition, Applied Physics A, 107 (2012) 227-232.

[49] S. Wang, G. Xia, X. Fu, H. He, J. Shao, Z. Fan, Preparation and characterization of nanostructured ZrO2 thin films by glancing angle deposition, Thin Solid Films, 515 (2007) 3352-3355.

[50] N. Jie, Z. Yu, Z. Qin, Z. Zhengjun, Morphology in-Design Deposition of HfO2 Thin Films, Journal of the American Ceramic Society, 91 (2008) 3458-3460.

[51] H.A. MacLeod, Thin-Film Optical Filters, Third Edition, CRC Press2001.

[52] P.J. Kelly, R.D. Arnell, Magnetron sputtering: a review of recent developments and applications, Vacuum, 56 (2000) 159-172.

[53] R. Behrisch, Introduction and overview, in: R. Behrisch (Ed.) Sputtering by Particle Bombardment I: Physical Sputtering of Single-Element Solids, Springer Berlin Heidelberg, Berlin, Heidelberg, 1981, pp. 1-8.

[54] P.D. Townsend, J.C. Kelly, N.E.W. Hartley, Ion implantation, sputtering and their applications, Academic Press1976.

[55] G. Binnig, H. Rohrer, C. Gerber, E. Weibel, Surface Studies by Scanning Tunneling Microscopy, Physical Review Letters, 49 (1982) 57-61.

[56] G. Binnig, C.F. Quate, C. Gerber, Atomic Force Microscope, Physical Review Letters, 56 (1986) 930-933.

[57] B. Voigtlaender, Scanning Probe Microscopy: Atomic Force Microscopy and Scanning Tunneling Microscopy, Springer Berlin Heidelberg2015.

[58] P. Eaton, P. West, Atomic Force Microscopy, OUP Oxford2010.

[59] S. Amelio, A.V. Goldade, U. Rabe, V. Scherer, B. Bhushan, W. Arnold, Measurements of elastic properties of ultra-thin diamond-like carbon coatings using atomic force acoustic microscopy, Thin Solid Films, 392 (2001) 75-84.

[60] U. Rabe, K. Janser, W. Arnold, Vibrations of free and surface-coupled atomic force microscope cantilevers: Theory and experiment, Rev. Sci. Instrum., 67 (1996) 3281-3293.

[61] P. Maivald, H.J. Butt, S.A.C. Gould, C.B. Prater, B. Drake, J.A. Gurley, V.B. Elings, P.K. Hansma, Using force modulation to image surface elasticities with the atomic force microscope, Nanotechnology, 2 (1991) 103.

[62] H.-U. Krotil, T. Stifter, H. Waschipky, K. Weishaupt, S. Hild, O. Marti, Pulsed force mode: a new method for the investigation of surface properties, Surface and Interface Analysis, 27 (1999) 336-340.

[63] D. Passeri, A. Bettucci, M. Germano, M. Rossi, A. Alippi, S. Orlanducci, M.L. Terranova, M. Ciavarella, Effect of tip geometry on local indentation modulus measurement via atomic force acoustic microscopy technique, Review of Scientific Instruments, 76 (2005) 093904.

[64] K.L. Johnson, Normal contact of elastic solids – Hertz theory, Contact Mechanics:, Cambridge University Press, Cambridge, 1985, pp. 84-106.

[65] G. Stan, W. Price, Quantitative measurements of indentation moduli by atomic force acoustic microscopy using a dual reference method, Review of Scientific Instruments, 77 (2006) 103707.

[66] L. Reimer, Scanning Electron Microscopy: Physics of Image Formation and Microanalysis, Springer1998.

[67] D. Koningsberger, R. Prins, X-ray absorption: principles, applications, techniques of EXAFS, SEXAFS, and XANES, DOI (1988).

[68] A.L. Ulery, L.R. Drees, Methods of soil analysis: mineralogical methods, ASA-CSSA-SSSA2008.

[69] G. Bunker, Introduction to XAFS: a practical guide to X-ray absorption fine structure spectroscopy, Cambridge University Press2010.

[70] S. Basu, C. Nayak, A.K. Yadav, A. Agrawal, A.K. Poswal, D. Bhattacharyya, S.N. Jha, N.K. Sahoo, A comprehensive facility for EXAFS measurements at the INDUS-2

synchrotron source at RRCAT, Indore, India, Journal of Physics: Conference Series, 493 (2014) 012032.

[71] H.A. Macleod, Basic Theory, Thin-Film Optical Filters, Fourth Edition, CRC Press, 2010, pp. 13-71.

[72] N.M. Kamble, R.B. Tokas, A. Biswas, S. Thakur, D. Bhattacharyya, N.K. Sahoo, Determination of the optical constants of HfO2–SiO2 composite thin films through reverse fitting of transmission spectra, Vacuum, 86 (2011) 422-428.

[73] R.M.A. Azzam, N.M. Bashara, Ellipsometry and polarized light, North-Holland Pub. Co.1977.

[74] L.G. Parratt, Surface Studies of Solids by Total Reflection of X-Rays, Physical Review, 95 (1954) 359-369.

[75] S. Kobayashi, T. Nishikawa, T. Takenobu, S. Mori, T. Shimoda, T. Mitani, H. Shimotani, N. Yoshimoto, S. Ogawa, Y. Iwasa, Control of carrier density by self-assembled monolayers in organic field-effect transistors, Nat Mater, 3 (2004) 317-322.

[76] A. Kurokawa, K. Odaka, T. Fujimoto, Y. Azuma, XRR Analysis of the Transition Layer in SiO₂ Thin Film Formed on Si Surface, Shinku, 50 (2007) 199-201.

[77] C. Charles, N. Martin, M. Devel, J. Ollitrault, A. Billard, Correlation between structural and optical properties of WO3 thin films sputter deposited by glancing angle deposition, Thin Solid Films, 534 (2013) 275-281.

[78] Y.-J. Park, K.M.A. Sobahan, J.-J. Kim, C.-K. HwangBo, Optical and Structural Properties of Bilayer Circular Filter Prepared by Glancing Angle Deposition, Journal of the Optical Society of Korea, 13 (2009) 218-222.

[79] M.D. Gasda, G.A. Eisman, D. Gall, Nanorod PEM Fuel Cell Cathodes with Controlled Porosity, Journal of The Electrochemical Society, 157 (2010) B437-B440.

[80] K. Chiba, K. Sato, Y. Ebine, T. Sasaki, Metal evaporated tape for high band 8 mm video system, Consumer Electronics, IEEE Transactions on, 35 (1989) 421-428.

[81] N.G. Wakefield, A.L. Elias, M.J. Brett, J.C. Sit, Optical behaviour of hybrid LC/inorganic nanostructures, Integrated Optoelectronic Devices 2006, International Society for Optics and Photonics, 2006, pp. 61350G-61350G-61312.

[82] M.T. Taschuk, J.B. Sorge, J.J. Steele, M.J. Brett, Ion-beam assisted glancing angle deposition for relative humidity sensors, Sensors Journal, IEEE, 8 (2008) 1521-1522.

[83] J.E. Klemberg-Sapieha, J. Oberste-Berghaus, L. Martinu, R. Blacker, I. Stevenson, G. Sadkhin, D. Morton, S. McEldowney, R. Klinger, P.J. Martin, N. Court, S. Dligatch, M. Gross, R.P. Netterfield, Mechanical characteristics of optical coatings prepared by various techniques: a comparative study, Applied Optics, 43 (2004) 2670-2679.

[84] J.A. Turner, S. Hirsekorn, U. Rabe, W. Arnold, High-frequency response of atomic-force microscope cantilevers, Journal of Applied Physics, 82 (1997) 966-979.

[85] G.M. Pharr, D.L. Callahan, S.D. McAdams, T.Y. Tsui, S. Anders, A. Anders, J.W.A. III, I.G. Brown, C.S. Bhatia, S.R.P. Silva, J. Robertson, Hardness, elastic modulus, and structure of very hard carbon films produced by cathodic-arc deposition with substrate pulse biasing, Applied Physics Letters, 68 (1996) 779-781.

[86] D. Schneider, T. Schwarz, B. Schultrich, Determination of elastic modulus and thickness of surface layers by ultrasonic surface waves, Thin Solid Films, 219 (1992) 92-102.

[87] A.C. Ferrari, J. Robertson, M.G. Beghi, C.E. Bottani, R. Ferulano, R. Pastorelli, Elastic constants of tetrahedral amorphous carbon films by surface Brillouin scattering, Applied Physics Letters, 75 (1999) 1893-1895.

[88] U. Rabe, W. Arnold, Acoustic microscopy by atomic force microscopy, Applied Physics Letters, 64 (1994) 1493-1495.

[89] F. Marinello, P. Schiavuta, S. Vezzù, A. Patelli, S. Carmignato, E. Savio, Atomic force acoustic microscopy for quantitative nanomechanical characterization, Wear, 271 (2011) 534-538.

[90] M. Bai, X. Fu, D. Dorantes, B. Jin, X. Hu, Young's modulus determination of low-k porous films by wide-band DCC/LD SAW, J. Semicond, 32 (2011) 103003.

[91] X. Shan, X. Xiao, Y. Liu, Young's modulus characterization of low- k films of nanoporous Black Diamond™ by surface acoustic waves, Journal of Semiconductors, 31 (2010) 082002.

[92] D. Passeri, M. Rossi, A. Alippi, A. Bettucci, D. Manno, A. Serra, E. Filippo, M. Lucci, I. Davoli, Atomic force acoustic microscopy characterization of nanostructured selenium–tin thin films, Superlattices and Microstructures, 44 (2008) 641-649.

[93] U. Rabe, M. Kopycinska, S. Hirsekorn, W. Arnold, Evaluation of the contact resonance frequencies in atomic force microscopy as a method for surface characterisation (invited), Ultrasonics, 40 (2002) 49-54.

[94] U. Rabe, S. Amelio, M. Kopycinska, S. Hirsekorn, M. Kempf, M. Göken, W. Arnold, Imaging and measurement of local mechanical material properties by atomic force acoustic microscopy, Surface and Interface Analysis, 33 (2002) 65-70.

[95] U. Rabe, S. Amelio, E. Kester, V. Scherer, S. Hirsekorn, W. Arnold, Quantitative determination of contact stiffness using atomic force acoustic microscopy, Ultrasonics, 38 (2000) 430-437.

[96] U. Rabe, M. Kopycinska, S. Hirsekorn, J.M. Saldaña, G.A. Schneider, W. Arnold, High-resolution characterization of piezoelectric ceramics by ultrasonic scanning force microscopy techniques, Journal of Physics D: Applied Physics, 35 (2002) 2621.

[97] U. Rabe, Atomic Force Acoustic Microscopy, in: B. Bhushan, H. Fuchs (Eds.) Applied Scanning Probe Methods II: Scanning Probe Microscopy Techniques, Springer Berlin Heidelberg, Berlin, Heidelberg, 2006, pp. 37-90.

[98] R.B. Tokas, N.K. Sahoo, S. Thakur, N.M. Kamble, A comparative morphological study of electron beam co-deposited binary optical thin films of HfO2:SiO2 and ZrO2:SiO2, Current Applied Physics, 8 (2008) 589-602.

[99] R.B. Tokas, N.M. Kamble, S. Jena, S. Thakur, A.K. Poswal, N.K. Sahoo, Laser induced damage threshold studies of HfO2-SiO2 composite thin films, AIP Conference Proceedings, 1451 (2012) 76-78.

[100] D. Zhang, S. Fan, Y. Zhao, W. Gao, J. Shao, R. Fan, Y. Wang, Z. Fan, High laser-induced damage threshold HfO_2 films prepared by ion-assisted electron beam evaporation, Appl. Surf. Sci., 243 (2005) 232-237.

[101] L. Gallais, B. Mangote, M. Zerrad, M. Commandré, A. Melninkaitis, J. Mirauskas, M. Jeskevic, V. Sirutkaitis, Laser-induced damage of hafnia coatings as a function of pulse duration in the femtosecond to nanosecond range, Applied Optics, 50 (2011) C178-C187.

[102] M. Balog, M. Schieber, M. Michman, S. Patai, Chemical vapor deposition and characterization of HfO2 films from organo-hafnium compounds, Thin Solid Films, 41 (1977) 247-259.

[103] J.P. Lehan, Y. Mao, B.G. Bovard, H.A. Macleod, Optical and microstructural properties of hafnium dioxide thin films, Thin Solid Films, 203 (1991) 227-250.

[104] A.K. Poswal, A. Agrawal, A.K. Yadav, C. Nayak, S. Basu, S.R. Kane, C.K. Garg, D. Bhattachryya, S.N. Jha, N.K. Sahoo, Commissioning and first results of scanning type EXAFS beamline (BL-09) at INDUS-2 synchrotron source, AIP Conference Proceedings, 1591 (2014) 649-651.

[105] V. Scherer, W. Arnold, B. Bhushan, Lateral force microscopy using acoustic friction force microscopy, Surface and Interface Analysis, 27 (1999) 578-587.

[106] P.-E. Mazeran, J.-L. Loubet, Force modulation with a scanning force microscope: an analysis, Tribology Letters, 3 (1997) 125-132.

[107] J.E. Sader, J.W.M. Chon, P. Mulvaney, Calibration of rectangular atomic force microscope cantilevers, Review of Scientific Instruments, 70 (1999) 3967-3969.

[108] K. Tapily, J.E. Jakes, D.S. Stone, P. Shrestha, D. Gu, H. Baumgart, A.A. Elmustafa, Nanoindentation Investigation of HfO2 and Al2O3 Films Grown by Atomic Layer Deposition, Journal of The Electrochemical Society, 155 (2008) H545-H551.

[109] D.L. Windt, IMD Version 4.1.1, (http://cletus.phys.columbia.edu/windt/idl), DOI (2000).

[110] Paritosh, D.J. Srolovitz, Shadowing effects on the microstructure of obliquely deposited films, Journal of Applied Physics, 91 (2002) 1963-1972.

[111] M. Asmani, C. Kermel, A. Leriche, M. Ourak, Influence of porosity on Young's modulus and Poisson's ratio in alumina ceramics, Journal of the European Ceramic Society, 21 (2001) 1081-1086.

[112] A.P. Roberts, E.J. Garboczi, Elastic Properties of Model Porous Ceramics, Journal of the American Ceramic Society, 83 (2000) 3041-3048.

[113] J. Kováčik, Correlation between Young's modulus and porosity in porous materials, Journal of Materials Science Letters, 18 (1999) 1007-1010.

[114] D.-Y. Cho, H.-S. Jung, C.S. Hwang, Structural properties and electronic structure of ${\text{HfO}}_{2}{\text{-ZrO}}_{2}$ composite films, Physical Review B, 82 (2010) 094104.

[115] J. Morais, L. Miotti, K.P. Bastos, S.R. Teixeira, I.J.R. Baumvol, A.L.P. Rotondaro, J.J. Chambers, M.R. Visokay, L. Colombo, M.C.M. Alves, Environment of hafnium and silicon in Hf-based dielectric films: An atomistic study by x-ray absorption spectroscopy and x-ray diffraction, Applied Physics Letters, 86 (2005) 212906.

[116] D.C. Koningsberger, R. Prins, X-Ray Absorption: Principles, Applications, Techniques of EXAFS, SEXAFS and XANES, Wiley1988.

[117] E.A. Stern, M. Newville, B. Ravel, Y. Yacoby, D. Haskel, The UWXAFS analysis package: philosophy and details, Physica B: Condensed Matter, 208 (1995) 117-120.

[118] R.E. Hann, P.R. Suitch, J.L. Pentecost, Monoclinic Crystal Structures of ZrO2 and HfO2 Refined from X-ray Powder Diffraction Data, Journal of the American Ceramic Society, 68 (1985) C-285-C-286.

[119] J.E. Jaffe, R.A. Bachorz, M. Gutowski, Low-temperature polymorphs of Zr O 2 and Hf O 2: A density-functional theory study, Physical Review B, 72 (2005) 144107.

[120] P.S. Lysaght, J.C. Woicik, M.A. Sahiner, B.-H. Lee, R. Jammy, Characterizing crystalline polymorph transitions in HfO2 by extended x-ray absorption fine-structure spectroscopy, Applied Physics Letters, 91 (2007) 122910.

[121] R. Gavrila, A. Dinescu, D. Mardare, AFM Applications to the Study of Thin Films Morphology: A Power Spectral Density Approach, International Semiconductor Conference, 2006, IEEE, Sinaia, 2006, pp. 167-170.

[122] J.M. Elson, J.M. Bennett, Calculation of the power spectral density from surface profile data, Applied Optics, 34 (1995) 201-208.

[123] A.J. Perry, The surface topography of titanium nitride made by chemical vapor deposition, Surface and Coatings Technology, 132 (2000) 21-25.

[124] W. Kwaśny, L.A. Dobrzański, M. Pawlyta, W. Gulbiński, Fractal nature of surface topography and physical properties of the coatings obtained using magnetron sputtering, Journal of Materials Processing Technology, 157–158 (2004) 188-193.

[125] G. He, L. Zhu, Z. Sun, Q. Wan, L. Zhang, Integrations and challenges of novel high-k gate stacks in advanced CMOS technology, Prog. Mater Sci., 56 (2011) 475-572.

[126] G. He, Z. Sun, G. Li, L. Zhang, Review and Perspective of Hf-based High-k Gate Dielectrics on Silicon, Crit. Rev. Solid State Mater. Sci., 37 (2012) 131-157.

[127] G. He, X. Chen, Z. Sun, Interface engineering and chemistry of Hf-based high-k dielectrics on III–V substrates, Surf. Sci. Rep., 68 (2013) 68-107.

[128] M. Senthilkumar, N.K. Sahoo, S. Thakur, R.B. Tokas, Characterization of microroughness parameters in gadolinium oxide thin films: A study based on extended power spectral density analyses, Applied Surface Science, 252 (2005) 1608-1619.

[129] J.C. Stover, Optical scattering: measurement and analysis, SPIE optical engineering press Bellingham, Bellingham, 1995.

[130] D.J. Whitehouse, Handbook of surface metrology, CRC Press, 1994.

[131] J. Ferré-Borrull, A. Duparré, E. Quesnel, Procedure to characterize microroughness of optical thin films: application to ion-beam-sputtered vacuum-ultraviolet coatings, Applied Optics, 40 (2001) 2190-2199.

[132] C. Ruppe, A. Duparré, Roughness analysis of optical films and substrates by atomic force microscopy, Thin Solid Films, 288 (1996) 8-13.

[133] J.M. Elson, J.P. Rahn, J.M. Bennett, Light scattering from multilayer optics: comparison of theory and experiment, Applied Optics, 19 (1980) 669-679.

[134] E.L. Church, Fractal surface finish, Applied Optics, 27 (1988) 1518-1526.

[135] G. Palasantzas, Roughness spectrum and surface width of self-affine fractal surfaces via the K-correlation model, Physical Review B, 48 (1993) 14472-14478.

[136] G. Rasigni, F. Varnier, M. Rasigni, J.P. Palmari, A. Llebaria, Roughness spectrum and surface plasmons for surfaces of silver, copper, gold, and magnesium deposits, Physical Review B, 27 (1983) 819-830.

[137] T. Karabacak, Thin-film growth dynamics with shadowing and re-emission effects, Journal of Nanophotonics, 5 (2011) 052501-052501-052518.

[138] M.F. Cansizoglu, R. Engelken, H.-W. Seo, T. Karabacak, High Optical Absorption of Indium Sulfide Nanorod Arrays Formed by Glancing Angle Deposition, ACS Nano, 4 (2010) 733-740.

[139] J. Ni, Y. Zhu, S. Wang, Z. Li, Z. Zhang, B. Wei, Nanostructuring HfO2 Thin Films as Antireflection Coatings, Journal of the American Ceramic Society, 92 (2009) 3077-3080.

[140] C. Patzig, T. Karabacak, B. Fuhrmann, B. Rauschenbach, Glancing angle sputter deposited nanostructures on rotating substrates: Experiments and simulations, Journal of Applied Physics, 104 (2008) 094318.

[141] H.J. Gwon, Y. Park, C.W. Moon, S. Nahm, S.-J. Yoon, S.Y. Kim, H.W. Jang, Superhydrophobic and antireflective nanograss-coated glass for high performance solar cells, Nano Research, 7 (2014) 670-678.

[142] J.Q. Xi, M.F. Schubert, J.K. Kim, E.F. Schubert, M. Chen, S.-Y. Lin, LiuW, J.A. Smart, Optical thin-film materials with low refractive index for broadband elimination of Fresnel reflection, Nat Photon, 1 (2007) 176-179.

[143] Y.J. Park, K.M.A. Sobahan, C.K. Hwangbo, Wideband circular polarization reflector fabricated by glancing angle deposition, Optics Express, 16 (2008) 5186-5192.

[144] Y.-P. Zhao, S.-H. Li, S.B. Chaney, S. Shanmukh, J.-G. Fan, R.A. Dluhy, W. Kisaalita, Designing nanostructures for sensor applications, Journal of Electronic Materials, 35 (2006) 846-851.

[145] G.K. Kannarpady, R. Sharma, B. Liu, S. Trigwell, C. Ryerson, A.S. Biris, Silane decorated metallic nanorods for hydrophobic applications, Applied Surface Science, 256 (2010) 1679-1682.

[146] S.M. Haque, P.R. Sagdeo, S. Balaji, K. Sridhar, S. Kumar, D. Bhattacharyya, D. Bhattacharyya, N.K. Sahoo, Effect of substrate bias and oxygen partial pressure on properties of RF magnetron sputtered HfO2 thin films, Journal of Vacuum Science & Technology B, Nanotechnology and Microelectronics: Materials, Processing, Measurement, and Phenomena, 32 (2014) 03D104.

[147] F.L. Martínez, M. Toledano-Luque, J.J. Gandía, J. Cárabe, W. Bohne, J. Röhrich, E. Strub, I. Mártil, Optical properties and structure of HfO 2 thin films grown by high pressure reactive sputtering, Journal of Physics D: Applied Physics, 40 (2007) 5256.

[148] Z.W. Ma, L.X. Liu, Y.Z. Xie, Y.R. Su, H.T. Zhao, B.Y. Wang, X.Z. Cao, X.B. Qin, J. Li, Y.H. Yang, E.Q. Xie, Spectroscopic ellipsometry and positron annihilation investigation of sputtered HfO2 films, Thin Solid Films, 519 (2011) 6349-6353.

[149] R.K. Jain, Y.K. Gautam, V. Dave, A.K. Chawla, R. Chandra, A study on structural, optical and hydrophobic properties of oblique angle sputter deposited HfO2 films, Applied Surface Science, 283 (2013) 332-338.

[150] T. Nishide, S. Honda, M. Matsuura, M. Ide, Surface, structural and optical properties of sol-gel derived HfO2 films, Thin Solid Films, 371 (2000) 61-65.

[151] J.M. Khoshman, A. Khan, M.E. Kordesch, Amorphous hafnium oxide thin films for antireflection optical coatings, Surface and Coatings Technology, 202 (2008) 2500-2502.

[152] M. Fadel, O.A. Azim M., O.A. Omer, R.R. Basily, A study of some optical properties of hafnium dioxide (HfO2) thin films and their applications, Applied Physics A, 66 (1998) 335-343.

[153] G.F. Iriarte, J.G. Rodriguez, F. Calle, Effect of substrate–target distance and sputtering pressure in the synthesis of AlN thin films, Microsystem Technologies, 17 (2011) 381-386.

[154] A. Thaveedeetrakul, N. Witit-anun, V. Boonamnuayvitaya, The role of target-to-substrate distance on the DC magnetron sputtered zirconia thin films' bioactivity, Applied Surface Science, 258 (2012) 2612-2619.

[155] S.H. Jeong, J.H. Boo, Influence of target-to-substrate distance on the properties of AZO films grown by RF magnetron sputtering, Thin Solid Films, 447–448 (2004) 105-110.

[156] R. Wuhrer, W.Y. Yeung, Effect of target–substrate working distance on magnetron sputter deposition of nanostructured titanium aluminium nitride coatings, Scripta Materialia, 49 (2003) 199-205.

[157] P.R. Sagdeo, D.D. Shinde, J.S. Misal, N.M. Kamble, R.B. Tokas, A. Biswas, A.K. Poswal, S. Thakur, D. Bhattacharyya, N.K. Sahoo, S.C. Sabharwal, Deposition and characterization of titania–silica optical multilayers by asymmetric bipolar pulsed dc sputtering of oxide targets, Journal of Physics D: Applied Physics, 43 (2010) 045302.

[158] W. Bo, W. Mei, W. Ruzhi, H. Anping, Z. Hua, Z. Yunjuan, Y. Hui, W. Seiping, The growth of AlN films composed of silkworm-shape grains and the orientation mechanism, Materials Letters, 53 (2002) 367-370.

[159] Y. Ahn, Y.-H. Kim, S.-I. Kim, K.-H. Jeong, Thickness dependent surface microstructure evolution of bismuth thin film prepared by molecular beam deposition method, Current Applied Physics, 12 (2012) 1518-1522.

[160] G. Thomas, A.S. Evan, P.B. Matthew, Height-Height Correlation Function to Determine Grain Size in Iron Phthalocyanine Thin Films, Journal of Physics: Conference Series, 417 (2013) 012069.

[161] J. Lintymer, N. Martin, J.-M. Chappe, J. Takadoum, Glancing angle deposition to control microstructure and roughness of chromium thin films, Wear, 264 (2008) 444-449.

[162] S. Wang, X. Fu, G. Xia, J. Wang, J. Shao, Z. Fan, Structure and optical properties of ZnS thin films grown by glancing angle deposition, Applied Surface Science, 252 (2006) 8734-8737.

[163] K. Vedam, Optical characterization of real surfaces and films, Academic Press1994.

[164] G.E. Jellison, F.A. Modine, Parameterization of the optical functions of amorphous materials in the interband region, Applied Physics Letters, 69 (1996) 371-373.

[165] National Institute of Standard and Technology (NIST), NIST/SEMATECH e-Handbook of Statistical Methods, NIST, Gaithersburg, MD, http://www.itl.nist.gov/div898/handbook/, DOI (2007).

[166] S. Mahieu, K.V. Aeken, D. Depla, D. Smeets, A. Vantomme, Dependence of the sticking coefficient of sputtered atoms on the target–substrate distance, Journal of Physics D: Applied Physics, 41 (2008) 152005.

[167] J. Daillant, A. Gibaud, X-ray and Neutron Reflectivity: Principles and Applications, Springer Berlin Heidelberg2008.

[168] H. WENDEL, H. HOLZSCHUH, H. SUHR, G. ERKER, S. DEHNICKE, M. MENA, THIN ZIRCONIUM DIOXIDE AND YTTRIUM OXIDE-STABILIZED ZIRCONIUM DIOXIDE FILMS PREPARED BY PLASMA-CVD, Modern Physics Letters B, 04 (1990) 1215-1225.

[169] L. Weifeng, L. Xuanyong, H. Anping, K.C. Paul, Structure and properties of zirconia (ZrO 2) films fabricated by plasma-assisted cathodic arc deposition, Journal of Physics D: Applied Physics, 40 (2007) 2293.

[170] C.Y. Ma, F. Lapostolle, P. Briois, Q.Y. Zhang, Effect of O2 gas partial pressure on structures and dielectric characteristics of rf sputtered ZrO2 thin films, Applied Surface Science, 253 (2007) 8718-8724.

[171] M. Andrieux, P. Ribot, C. Gasquères, B. Servet, G. Garry, Effect of the oxygen partial pressure on the toughness of tetragonal zirconia thin films for optical applications, Applied Surface Science, 263 (2012) 284-290.

[172] C.-Y. Lin, C.-Y. Wu, C.-Y. Wu, C.-C. Lin, T.-Y. Tseng, Memory effect of RF sputtered ZrO2 thin films, Thin Solid Films, 516 (2007) 444-448.

[173] F. Rebib, N. Laidani, G. Gottardi, V. Micheli, R. Bartali, Y. Jestin, E. Tomasella, M. Ferrari, L. Thomas, Investigation of structural and optical properties of sputtered Zirconia thin films, Eur. Phys. J. Appl. Phys., 43 (2008) 363-368.

[174] D. Panda, T.-Y. Tseng, Growth, dielectric properties, and memory device applications of ZrO2 thin films, Thin Solid Films, 531 (2013) 1-20.

[175] D.Q. Xiao, G. He, J.G. Lv, P.H. Wang, M. Liu, J. Gao, P. Jin, S.S. Jiang, W.D. Li, Z.Q. Sun, Interfacial modulation and electrical properties improvement of solution-processed ZrO2 gate dielectrics upon Gd incorporation, Journal of Alloys and Compounds, 699 (2017) 415-420.

[176] H.J. Qi, L.H. Huang, Z.S. Tang, C.F. Cheng, J.D. Shao, Z.X. Fan, Roughness evolution of ZrO2 thin films grown by reactive ion beam sputtering, Thin Solid Films, 444 (2003) 146-152.

[177] S. Shao, Z. Fan, J. Shao, H. He, Evolutions of residual stress and microstructure in ZrO2 thin films deposited at different temperatures and rates, Thin Solid Films, 445 (2003) 59-62.

[178] G. Tian, J. Huang, T. Wang, H. He, J. Shao, Microstructure and laser-induced damage threshold of ZrO2 coatings dependence on annealing temperature, Applied Surface Science, 239 (2005) 201-208.

[179] D. Zhang, J. Shao, Y. Zhao, S. Fan, R. Hong, Z. Fan, Laser-induced damage threshold of ZrO2 thin films prepared at different oxygen partial pressures by electron-beam evaporation, Journal of Vacuum Science & Technology A: Vacuum, Surfaces, and Films, 23 (2005) 197-200.

[180] M. Levichkova, V. Mankov, N. Starbov, D. Karashanova, B. Mednikarov, K. Starbova, Structure and properties of nanosized electron beam deposited zirconia thin films, Surface and Coatings Technology, 141 (2001) 70-77.

[181] I.J. Hodgkinson, F. Horowitz, H.A. Macleod, M. Sikkens, J.J. Wharton, Measurement of the principal refractive indices of thin films deposited at oblique incidence, Journal of the Optical Society of America A, 2 (1985) 1693-1697.

[182] B. Bondars, G. Heidemane, J. Grabis, K. Laschke, H. Boysen, J. Schneider, F. Frey, Powder diffraction investigations of plasma sprayed zirconia, Journal of Materials Science, 30 (1995) 1621-1625.

[183] R. Srinivasan, R.J. De Angelis, G. Ice, B.H. Davis, Identification of tetragonal and cubic structures of zirconia using synchrotron x-radiation source, Journal of Materials Research, 6 (1991) 1287-1292.

[184] M. Jafarpour, E. Rezapour, M. Ghahramaninezhad, A. Rezaeifard, A novel protocol for selective synthesis of monoclinic zirconia nanoparticles as a heterogeneous catalyst for condensation of 1,2-diamines with 1,2-dicarbonyl compounds, New Journal of Chemistry, 38 (2014) 676-682.

[185] J. Chevalier, L. Gremillard, A.V. Virkar, D.R. Clarke, The Tetragonal-Monoclinic Transformation in Zirconia: Lessons Learned and Future Trends, Journal of the American Ceramic Society, 92 (2009) 1901-1920.

[186] B. Alzyab, C.H. Perry, R.P. Ingel, High-Pressure Phase Transitions in Zirconia and Yttria-Doped Zirconia, Journal of the American Ceramic Society, 70 (1987) 760-765.

[187] Z. Ji, J.M. Rigsbee, Growth of Tetragonal Zirconia Coatings by Reactive Sputter Deposition, Journal of the American Ceramic Society, 84 (2001) 2841-2844.

[188] R.C. Garvie, The Occurrence of Metastable Tetragonal Zirconia as a Crystallite Size Effect, The Journal of Physical Chemistry, 69 (1965) 1238-1243.

[189] R.B. Tokas, S. Jena, S. Thakur, N.K. Sahoo, Effect of angle of deposition on micro-roughness parameters and optical properties of HfO2 thin films deposited by reactive electron beam evaporation, Thin Solid Films, 609 (2016) 42-48.

[190] C.H. Zhang, Z.-J. Liu, K.Y. Li, Y.G. Shen, J.B. Luo, Microstructure, surface morphology, and mechanical properties of nanocrystalline TiN/amorphous Si3N4 composite films synthesized by ion beam assisted deposition, Journal of Applied Physics, 95 (2004) 1460-1467.

[191] A. Mannelquist, N. Almqvist, S. Fredriksson, Influence of tip geometry on fractal analysis of atomic force microscopy images, Applied Physics A, 66 (1998) S891-S895.

[192] H. Fujiwara, Spectroscopic Ellipsometry: Principles and Applications, Wiley2007.

[193] H. Adachi, K. Wasa, 1 - Thin Films and Nanomaterials, Handbook of Sputtering Technology (Second Edition), William Andrew Publishing, Oxford, 2012, pp. 3-39.

[194] S.M. Haque, K.D. Rao, J.S. Misal, R.B. Tokas, D.D. Shinde, J.V. Ramana, S. Rai, N.K. Sahoo, Study of hafnium oxide thin films deposited by RF magnetron sputtering under glancing angle deposition at varying target to substrate distance, Applied Surface Science, 353 (2015) 459-468.

[195] A. Garahan, L. Pilon, J. Yin, I. Saxena, Effective optical properties of absorbing nanoporous and nanocomposite thin films, Journal of Applied Physics, 101 (2007) 014320.

[196] A.S. Ferlauto, G.M. Ferreira, J.M. Pearce, C.R. Wronski, R.W. Collins, X. Deng, G. Ganguly, Analytical model for the optical functions of amorphous semiconductors from the near-infrared to ultraviolet: Applications in thin film photovoltaics, Journal of Applied Physics, 92 (2002) 2424-2436.

[197] S. Ben Amor, B. Rogier, G. Baud, M. Jacquet, M. Nardin, Characterization of zirconia films deposited by r.f. magnetron sputtering, Materials Science and Engineering: B, 57 (1998) 28-39.

[198] A. Hojabri, Structural and optical characterization of ZrO2 thin films grown on silicon and quartz substrates, Journal of Theoretical and Applied Physics, 10 (2016) 219-224.

[199] G. Balakrishnan, T.N. Sairam, P. Kuppusami, R. Thiumurugesan, E. Mohandas, V. Ganesan, D. Sastikumar, Influence of oxygen partial pressure on the properties of pulsed laser deposited nanocrystalline zirconia thin films, Applied Surface Science, 257 (2011) 8506-8510.

[200] B. Dick, M.J. Brett, T. Smy, Investigation of substrate rotation at glancing incidence on thin-film morphology, Journal of Vacuum Science & Technology B, 21 (2003) 2569-2575.

[201] L. Zhang, H. Yang, X. Pang, K. Gao, A.A. Volinsky, Microstructure, residual stress, and fracture of sputtered TiN films, Surface and Coatings Technology, 224 (2013) 120-125.

[202] D. Malacara, Optical Shop Testing, Wiley2007.

[203] R.S. Sirohi, Wave Optics And Its Applications, Orient BlackSwan1993.

[204] M.A. Hopcroft, W.D. Nix, T.W. Kenny, What is the Young's Modulus of Silicon?, Journal of Microelectromechanical Systems, 19 (2010) 229-238.

[205] A.J. Detor, A.M. Hodge, E. Chason, Y. Wang, H. Xu, M. Conyers, A. Nikroo, A. Hamza, Stress and microstructure evolution in thick sputtered films, Acta Materialia, 57 (2009) 2055-2065.

[206] N.A. Marks, D.R. McKenzie, B.A. Pailthorpe, Molecular-dynamics study of compressive stress generation, Physical Review B, 53 (1996) 4117-4124.

[207] C.A. Davis, A simple model for the formation of compressive stress in thin films by ion bombardment, Thin Solid Films, 226 (1993) 30-34.

[208] C.-W. Pao, S.M. Foiles, E.B. Webb, D.J. Srolovitz, J.A. Floro, Thin Film Compressive Stresses due to Adatom Insertion into Grain Boundaries, Physical Review Letters, 99 (2007) 036102.

[209] M.J. Buehler, A. Hartmaier, H. Gao, Atomistic and continuum studies of crack-like diffusion wedges and associated dislocation mechanisms in thin films on substrates, Journal of the Mechanics and Physics of Solids, 51 (2003) 2105-2125.

[210] E. Chason, B.W. Sheldon, L.B. Freund, J.A. Floro, S.J. Hearne, Origin of Compressive Residual Stress in Polycrystalline Thin Films, Physical Review Letters, 88 (2002) 156103.

[211] A. Misra, M. Nastasi, Evolution of tensile residual stress in thin metal films during energetic particle deposition, Journal of Materials Research, 14 (1999) 4466-4469.

[212] A. Banerjea, J.R. Smith, Origins of the universal binding-energy relation, Physical Review B, 37 (1988) 6632-6645.

[213] J. Sancho-Parramon, M. Modreanu, S. Bosch, M. Stchakovsky, Optical characterization of HfO2 by spectroscopic ellipsometry: Dispersion models and direct data inversion, Thin Solid Films, 516 (2008) 7990-7995.

[214] M. Jerman, Z. Qiao, D. Mergel, Refractive index of thin films of SiO2, ZrO2, and HfO2 as a function of the films' mass density, Applied Optics, 44 (2005) 3006-3012.

[215] W.S. Weiglhofer, A. Lakhtakia, B. Michel, Maxwell Garnett and Bruggeman formalisms for a particulate composite with bianisotropic host medium, Microwave and Optical Technology Letters, 15 (1997) 263-266.

[216] S. Jena, R.B. Tokas, N. Kamble, S. Thakur, D. Bhattacharyya, N.K. Sahoo, Investigation of elastic and optical properties of electron beam evaporated ZrO2–MgO composite thin films, Thin Solid Films, 537 (2013) 163-170.

[217] D. Franta, D. Nečas, I. Ohlídal, A. Giglia, Optical characterization of SiO2 thin films using universal dispersion model over wide spectral range, Proceedings of SPIE - The International Society for Optical Engineering.

[218] M. Zarchi, S. Ahangarani, Optical and morphological properties of silicon dioxide thin films, Journal of Materials Science: Materials in Electronics, 27 (2016) 1165-1170.

[219] U.S.N.B.o. Standards, A.S.f. Testing, Materials, N.I.o. Standards, Technology, Laser Induced Damage in Optical Materials: Proceedings of a Symposium Sponsored by the American Society for Testing and Materials and by the National Bureau of Standards, U.S. Department of Commerce, National Bureau of Standards1986.